A Be+ Ion Trap for H2+ Spectroscopy

Johannes M Heinrich

THÈSE DE DOCTORAT DE SORBONNE UNIVERSITÉ

Spécialité: Physique

École doctorale: Physique en Île-de-France

réalisée au

Laboratoire Kastler Brossel

présentée par

Johannes M. HEINRICH

pour obtenir le grade de:

DOCTEUR DE SORBONNE UNIVERSITÉ

Sujet de la thèse:

A Be^+ Ion Trap for H_2^+ Spectroscopy

soutenue le 13 avril 2018

Composition du jury:

M.	Cyril DRAG	LPP	Rapporteur
M.	Luca GUIDONI	MPQ Paris	Examinateur
M.	Johannes HECKER DENSCHLAG	University Ulm	Examinateur
M.	Laurent HILICO	LKB	Directeur de thèse
M^{me}	Martina KNOOP	PIIM Marseille	Rapporteuse
M.	Martino TRASSINELLI	INSP-UPMC	Président du jury

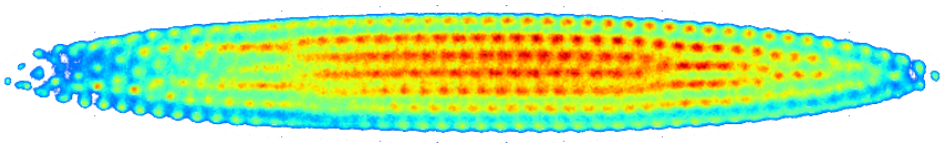

≈ 1000 Be^+ and a few H_2^+ ions
27/02/2018 at 15:20

The work presented in this manuscript was carried out from October 2014 to March 2018 in the group *trapped ions* at Laboratoire Kastler Brossel, under the supervision of Pr Laurent Hilico. It was part of the Marie Curie Initial Training Network COMIQ and funded by the European Commission under grant agreement no. 607491.

to my teachers,
and my parents,
who remain both.

Contents

List of Figures

List of Tables

Chapter 1

Introduction

... Daß ich erkenne, was die Welt
im Innersten zusammenhält.

Goethe, Faust. Der Tragödie erster Teil, 1808.
Szene: Nacht, Faust allein in seinem gotischen Zimmer

The overall goal of the experiment currently set up at LKB is to test the theory of quantum electrodynamics and to yield a direct measurement of the fundamental constant μ_{pe}, the proton to electron mass ratio.
This introduction is intended to deliver first answers to the three important questions of *what*, *why*, and *how*.

- *what*: The experimental setup developed during this PhD project provides important parts to measure the ro-vibrational Doppler-free two photon transition $\nu = 0, L = 2 \rightarrow \nu = 1, L = 2$ of the electronic ground state in the molecular hydrogen ion H_2^+.
- *why*: As further explained in section 1.1, the precise measurement of this transition frequency will allow for testing the validity of quantum electrodynamics and provides an alternative method for the determination of fundamental constants.
- *how*: Usage of laser-cooled Be^+ ions for sympathetic cooling of the H_2^+ ions will allow to strongly reduce the second-order Doppler effect, which is necessary to obtain precise measurements. Cold Be^+ Coulomb crystals are a tool which will also be used for the sympathetic cooling of antimatter ions, an important step towards the measurement of $\bar{g}$, the earth gravity acceleration on antimatter.

1.1 What and Why - Spectroscopy of H_2^+

The histories of spectroscopy, atomic and molecular physics, and quantum mechanics are deeply connected with one other, and are the foundation of our current understanding of nature. To understand the role of spectroscopy of molecular hydrogen ions it is helpful to review the beginnings.

1.1.1 The Hydrogen Atom

Using the dispersion of light, Ångstrom could observe different lines
1853 in the spectrum of atomic hydrogen in 1853 [1], and in 1862 correctly identified hydrogen as the most abundant part of the Sun [2]. Meanwhile, Maxwell provided a theoretical basis for the description
1873 of electromagnetic waves in 1873, and assigned visible light as part of
1885 the electromagnetic spectrum. In 1885, Balmer set up an empirical equation, reproducing the pattern in which the hydrogen lines occur,
1900 and predicting additional lines [3]. In 1900, Planck could explain the spectral density of the electromagnetic radiation emitted by a black body by introducing the constant h, which connects the energy E in the atomic vibrations with the frequency of the radiated electromagnetic wave via $E = nh\nu$ [4]. This energy was interpreted by Einstein
1905 in 1905 as a quantum of the electromagnetic wave (a photon). At this point it was already known that electrons are a part of the atom, and the plum pudding model of the atomic structure had been proposed
1909 by Thomson. In 1909, Rutherford et al. performed scattering of alpha particles at a thin gold foil, with the conclusion that atoms are made up of a nucleus and surrounding electrons [5]. Based on the discoveries
1913 mentioned above, Bohr postulated the famous Bohr model in 1913 [6], by introducing an ad hoc quantization rule of the atomic energy levels. In order to explain the observed fine structure in the hydrogen spectrum, Sommerfeld introduced a second quantum number (and also the
1916 fine structure constant) in 1916, which partially could explain the observations. To explain the doublet splitting Goudsmit and Uhlenbeck
1925 proposed the existence of an intrinsic spin of the electron in 1925.
1926 One year later Schrödinger came up with the equation named after him [7]. Applied to the hydrogen atom, the equation cannot only reproduce the energy levels, but for example provide information about
1928 the geometric shape of the atomic orbitals. In 1928 the theory was further improved by Dirac [8]. His equation of motion describes the relativistic motion of the electron and the spin of the electron. One of the stunning results of this equation was the prediction of antimatter.
1947 While in the Dirac equation some energy levels are degenerate, in 1947 a splitting of the $2S_{1/2}$ - $2P_{1/2}$ levels in hydrogen was observed by Lamb and Retherford [9]. This marks the starting point of quantum electrodynamics (QED) [10]. It allowed to interprete the shift of atomic

energy levels from Dirac's equation due to the interaction of the atom with vacuum fluctuations of the electromagnetic field. The final effect which has to be taken into account for a full explanation of the hydrogen spectrum is the hyperfine splitting, which is due to the nuclear magnetic moment, but will not be discussed further here.

fundamental constants

The theory of QED depends on fundamental constants. Discrepancies between theory and experimental results question the theory of QED, so that it is crucial to know the fundamental constants with high accuracy. The Committee on Data for Science and Technology (CODATA) publishes every four years recommended values and uncertainties for the fundamental constants. In the beginning of 2018 the most recent data is from 2014, giving, for example, accuracies of $5.9 \cdot 10^{-12}$ for the Rydberg constant and $7 \cdot 10^{-3}$ for the proton charge radius [11].

precision spectroscopy

The determination of these two constants is mainly based on precision spectroscopy of the hydrogen atom, namely the ultra-narrow $1S \rightarrow 2S$ transition and $2S \rightarrow n/DP$ transitions. While the $1S \rightarrow 2S$ transition is known with an accuracy of $4.2 \cdot 10^{-15}$ [12], the $2S \rightarrow 4P$ transition was measured with an accuracy of $3.7 \cdot 10^{-12}$ [13], and a recent investigation of the $1S \rightarrow 3S$ transition yielded an accuracy of $9 \cdot 10^{-13}$ [14]. These precision measurements feed the CODATA values, which in turn are needed for accurate theoretical predictions. One can write the following simplified formula for the energy levels of the hydrogen atom:

$$E_{n,l,j} = hcR_\infty \left[-\frac{1}{n^2} + A\left(n,l,j\right) + \frac{4}{3n^3} \left(\frac{r_p}{a_0}\right)^2 \delta_{l0} + \dots \right], \qquad (1.1)$$

where R_∞ is the Rydberg constant and r_p the proton charge radius, and $a_0 = \frac{\alpha}{4\pi R_\infty}$ the Bohr radius with the fine structure constant α. The first term is the nonrelativistic Schrödinger energy, the second term takes relativistic and QED corrections into account, and the last term is the leading order nuclear size correction. The dependency of the energy levels in equation (1.1) on R_∞ and r_p illustrates the need for two narrow linewidth transitions. However, the hydrogen atom has only one transition with an ultra-narrow linewidth in the UV regime, the transition between the ground state $1S$ and the metastable state $2S$. Measuring this transition with high accuracy allows to determine one of the two constants R_∞ or r_p, while the other one must be known from other measurements.

proton radius puzzle

In 2010 spectroscopy of muonic hydrogen delivered a value for the proton radius which deviates from the CODATA value by 5 standard deviations [15]. While the aforementioned precision measurement of the $2S \rightarrow 4P$ transition disagrees as well, the $1S \rightarrow 3S$ transition is again in agreement with other hydrogen measurements. This so called proton radius puzzle questions either the completeness of QED, or the

measurements used to obtain the CODATA value. Either way, this shows the need for further precision measurements which may help explain the discrepancy.

1.1.2 The Hydrogen Molecular Ion

The hydrogen molecular ion H_2^+ is the simplest molecule, consisting of two protons and one electron. Only one year after Schrödinger's
1927 equation was presented, Burrau published a first treatment of the hydrogen molecular ion [16], quickly followed by others [17, 18, 19]. It was one of the early achievements of quantum theory to explain a stable groundstate, something classical theories could not. The molecular hydrogen ion played and plays a similiar role in molecular physics as the hydrogen atom in atomic physics. Taking into account the effects first discovered in the hydrogen atom, the energy levels for H_2^+ may be written for each ro-vibrational level in the form [20]

$$E = hcR_\infty \left[E_{nr}\left(\mu_{pe}\right) + A_{QED}\left(\alpha\right) + A^{fs}\left(\frac{r_p}{a_0}\right)^2 \right], \qquad (1.2)$$

where the first term is the nonrelativistic Schrödinger energy, which depends on the mass ratio $\mu_{pe} = {}^{m_p}/_{m_e}$. The second term takes relativistic and QED corrections into account. The last term is a correction due to the finite size of the proton charge radius.
Due to the dependency on fundamental constants, spectroscopy of
1976 hydrogen molecular ions was already proposed in 1976 as a tool to accurately determine the proton to electron mass ratio μ_{pe} [21]. In
2016 2016, Karr et al. presented a selection of different narrow linewidth transitions in H_2^+, HD^+ and H, in order to determine the constants μ_{pe}, R_∞, r_p, μ_{pd} and r_d [20]. In contrast to the hydrogen atom, hydrogen molecular ions have multiple narrow linewidth transitions between long-lived ro-vibrational levels. These considerations make the hydrogen molecular ion H_2^+ a benchmark system for testing the validity of QED, and a promising candidate to obtain improved values for μ_{pe}, R_∞ and the proton charge radius r_p.

recent measurements Recently, a collaboration was able to measure the $\nu = 0 \rightarrow \nu = 8$ single-photon transition in HD^+ with partially resolved hyperfine structure (LaserLab in Amsterdam), and compare the results with theoretical predictions (LKB) [22, 23]. As a result the proton to electron mass ratio could be determined. However, the accuracy is about 27 times lower than provided by the CODATA adjustment of 2014. The main limitation is due to the Doppler effect. A new experiment to observe a Doppler-free two-photon $\nu = 0, L = 3 \rightarrow \nu = 4, L = 2 \rightarrow \nu = 9, L = 3$ transition is prepared in Amsterdam.

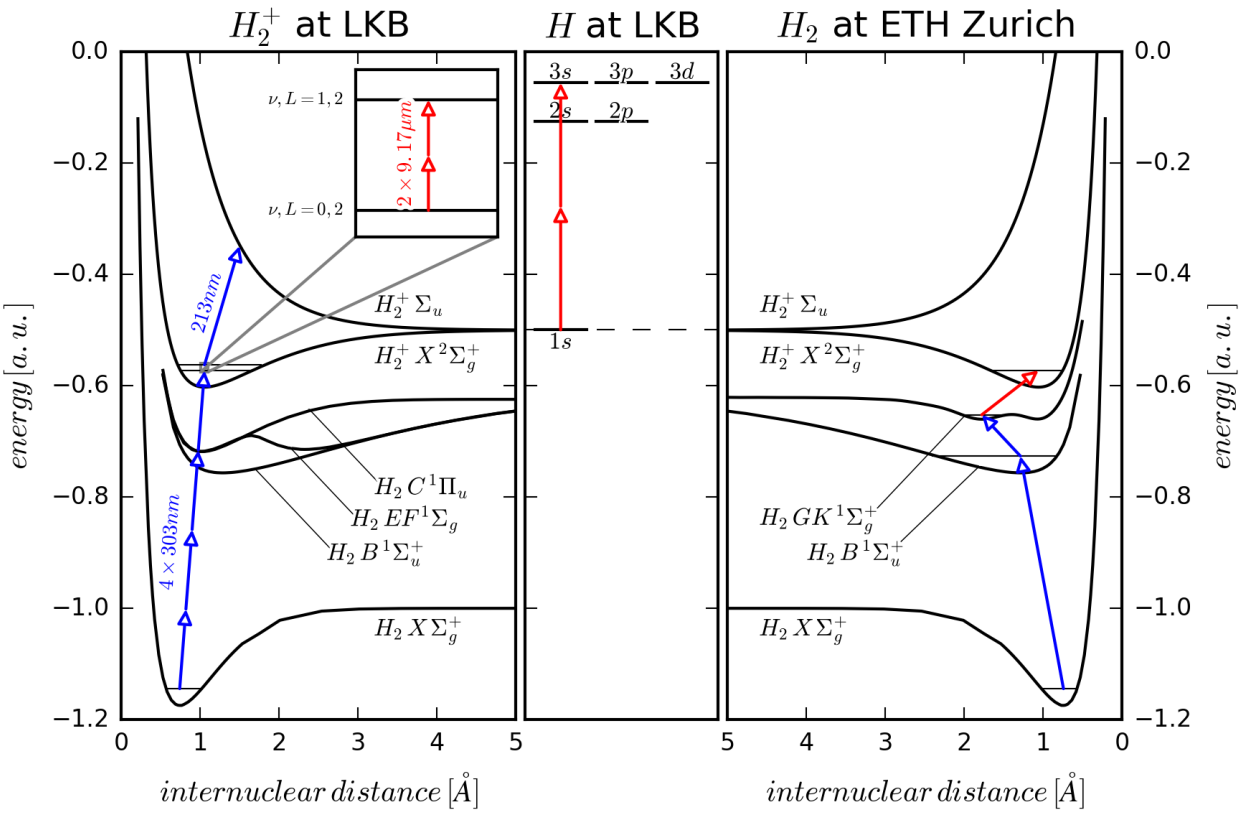

Figure 1.1: *Left: Electronic states in the Born-Oppenheimer approximation for* H_2 *and* H_2^+ *and transitions as planned at LKB. The arrows show the vibrational ground state preparation of* H_2^+ *using a* $3 + 1$ *REMPI scheme at* 303 nm*, and after that the* $2 + 1$ *REMPD spectroscopy. The inset shows the two-photon transition at* 9.17 μm *between two ro-vibrational levels. Center: The energy structure of the H atom and the transition currently probed at one of the groups at LKB. Right: Rydberg state spectroscopy of* H_2 *as performed at the ETH Zürich.*

The most stringent test of QED in molecular hydrogen is momentanly performed at the ETH Zürich by precision spectroscopy of molecular Rydberg states [24]. The excitation scheme to obtain the dissociation energy of molecular hydrogen can be seen on the right hand side of Fig. 1.1. The reported accuracy to the $n = 50$ Rydberg state is ${}^{\Delta\nu}/_{\nu} = 2 \cdot 10^{-10}$.

1.1.3 H_2^+ Spectroscopy at LKB

experimental scheme

The experiment which is set up at LKB aims to perform high precision spectroscopy of the $\nu = 0, L = 2 \rightarrow \nu = 1, L = 2$ two-photon transition in H_2^+. On the left hand side of Fig. 1.1 one can see the lowest electronic energy curves of H_2 and H_2^+ in the Born-Oppenheimer approximation. The overall experimental scheme is as follows: First

the H_2^+ molecules are prepared in the ro-vibrational $\nu = 0, L = 2$ state by resonance-enhanced multi-photon ionization (REMPI). We plan to use a $3 + 1$-photon transition at 303 nm from the electronic ground state of H_2, indicated by the four arrows in Fig. 1.1. Thereafter a resonance-enhanced multi-photon dissociation (REMPD) is performed. The REMPD consists of the two-photon spectroscopy laser at 9.17 μm (shown in the inset) and, as a final step, the excited H_2^+ molecules will be dissociated by a 213 nm laser. The last step is relevant to detect the success of the ro-vibrational transition, and the observed signal will be the loss of the H_2^+ ions.

aimed accuracy

With a narrow linewidth spectroscopy laser in the 100 Hz range at 9.17 μm we aim at an accuracy of $1 \cdot 10^{-12}$ or below for the experimental part. The theoretical calculations have reached an accuracy of $7.6 \cdot 10^{-12}$ [25], and should reach $3.0 \cdot 10^{-12}$ in the near future [26].

current CODATA standard

The CODATA value for the mass ratio μ_{pe} is determined by two separate measurements, for the mass of the proton by mass spectrometry, and for the mass of the electron by g-factor measurements [27]. In atomic units the relative uncertainties are $9.0 \cdot 10^{-11}$ and $2.9 \cdot 10^{-11}$, leading to an accuracy of $9.5 \cdot 10^{-11}$ for the proton to electron mass ratio. However, there is a recent improvement concerning the accuracy of the proton mass in atomic units, leading to an accuracy of $3.2 \cdot 10^{-11}$, but that also deviates from the CODATA value by about 3 standard deviations [28]. This shows again the need for additional measurements.

The high precision measurement of the $\nu = 0, L = 2 \rightarrow \nu = 1, L = 2$ transition will provide a direct optical determination of the mass ratio μ_{pe} by a different method, and an improvement of the accuracy by a factor of about 15 compared to the CODATA value of 2014 [11, 20].

1.2 How - Be^+ Coulomb Crystals

A limiting factor one encounters while performing precision spectroscopy is the Doppler effect and the induced broadening of the transition lines. While the first-order Doppler effect is not present in two-photon transitions with counter-propagating beams, the second-order Doppler-effect still remains and is given by

$$\frac{\Delta\nu}{\nu} = -\frac{v^2}{2c^2}, \tag{1.3}$$

where $\Delta\nu$ is the Doppler shift and v the velocity of the particles. Trapped particles in an RF trap experience RF heating. This RF heating depends on the number of trapped particles, the temperature of the ion cloud, and the amplitude of the applied RF voltage [29].

Without cooling, thermalization of the trapped ions occurs at $\approx 10\%$ of the trap depth [30], and the trap depth for H_2^+ in an RF trap can easily be more than 10 eV. One electron Volt corresponds to more than 10 000 K, and the maximum of the Maxwell-Boltzmann distribution for H_2^+ ions at this temperature is $\approx 9100\,{}^{m}/_{s}$. This leads to a second-order Doppler effect of $\left|\frac{\Delta\nu}{\nu}\right|_{2nd} > 2 \cdot 10^{-10}$, limiting the possible accuracy. In order to achieve the aimed precission of $1 \cdot 10^{-12}$ it is therefore necessary to cool the hydrogen molecular ions.
Unfortunately, molecular ions lack suitable transitions to perform laser cooling. However, sympathetic cooling by simultaneous trapping of a second, laser-cooled species allows to overcome this obstacle. Sympathetic cooling works best between particles of close masses, which is the reason why we chose beryllium as the lightest, alkaline-like ion with a suitable cooling transition. As we will see in the last chapter, cooling of trapped ions leads to the formation of so called Coulomb crystals, which are of interest per se.

the GBAR project

Sympathetic cooling relies on the Coulomb interaction and is not restricted to matter-matter ions, but also applies for antimatter ions. An example is the GBAR (gravitational behaviour of antimatter at rest) experiment [31]. This experiment aims at the determination of the effect of Earth's gravitational field on $\bar{H}$ antihydrogen atoms. The overall scheme is simple: prepare $\bar{H}$ atoms at rest and subsequently perform a free fall measurement. However, antimatter is produced in particle accelerators at high energies and needs to undergo multiple cooling steps in order to cool it down to sufficiently low temperatures in the μK range. Therefore, first an antimatter ion $\bar{H}^+$ will be formed, which can be confined in RF traps. Since $\bar{H}^+$ has only one electronic bound state, it cannot be directly laser cooled. Therefore, sympathetic cooling in mixed HD^+/Be^+ Coulomb crystals will be applied [32]. Two final cooling steps will be applied, first in a linear Paul trap using a large ion cloud, and thereafter in a precision trap, where a $\bar{H}^+$ Be^+ ion pair will be cooled to the vibrational quantum ground state. Finally photodetachment of the excess positron will be performed, and the free fall of the $\bar{H}$ will be measured.

in this thesis

One question which arises is how to detect and determine the position of the $\bar{H}^+$ ion in the Coulomb crystal of the linear Paul trap. The last chapter of this PhD project gives a possible answer to that question.

quantum simulations

Another application of Coulomb crystals might be the possibility to perform quantum simulations. For instance, quantum spin models are an important part of the description of condensed-matter systems and may be crucial to explain the physics underlying high-temperature superconductivity. However, these spin models are difficult to compute due to them being quantum many-body problems. In 1984, Feynman proposed the simulation of such many-body problems in well-controlled quantum systems [33]. For example, trapped ions are a promising candidate to observe and study quantum phase transi-

tions [34]. However, the experiments have been restricted to one-dimensional ion chains and therefore the quantum simulation of one-dimensional spin models. In surface traps it has already been shown that large, purely two-dimensional Coulomb crystals can be realized, containing up to a few hundred ions [35]. In linear Paul traps, however, two-dimensional Coulomb crystals of a similar size were not yet reported (at least to the knowledge of the author).

in this thesis In the last chapter of the work at hand the observation of large (the largest, to the knowledge of the author), purely two-dimensional Coulomb crystals in linear Paul traps is presented, having centered-square lattice and hexagonal lattice structures over a large region in the crystal center. Although the inter-ion distance is large as compared to theoretical considerations [36] this observations may help to design future ion traps capable of preparing large two-dimensional ion lattices.

1.3 Overview of this Work

chapter 2 Chapter 2 first presents a review of the trapping mechanism for ions in a linear Paul trap. Based thereon the choice for the trap design is elaborated, respecting major constraints of the overall experimental aim. Furthermore the Be^+ source, the vacuum system and the planned H_2^+ source are presented. Finally the imaging system for the ion detection and the experimental control software are explained.

chapter 3 Chapter 3 reviews the fundamentals of Doppler cooling and presents different options to provide laser light at 626 nm. A bow-tie cavity to perform frequency doubling and create the 313 nm light needed for Doppler cooling of Be^+ is also explained. Finally, the other laser sources needed for the REMPI of H_2 and REMPD of H_2^+ are shortly discussed.

chapter 4 First results are given in chapter 4. Starting with first crystallized ions, minimizing the micromotion is explained, and a precise evaluation of the magnification of the imaging system is obtained. Thereafter a large, three-dimensional Coulomb crystal is presented and methods to analyse the crystal are derived. This methods are modified in the subsequent section in order to analyse two-dimensional Coulomb crystals, and tested on selected examples. Additionally the highly ordered structure of the two dimensional crystals is investigated, and two different lattice structures can be identified. The last part of this chapter shows sympathetically cooled H_2^+ ions, so that a working setup for H_2^+ spectroscopy can be reported.

chapter 5 The last chapter summarizes the next steps which have to be taken, in order to observe a Doppler-free two-photon transition in cold, state selected H_2^+ ions.

Chapter 2

Trapping Charged Particles

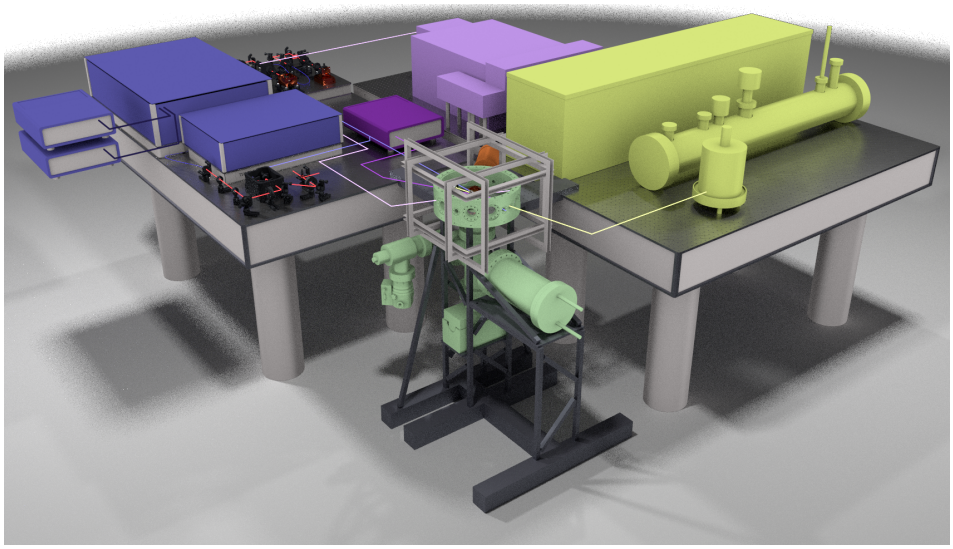

Figure 2.1: *Overview of the experimental setup. It shows the vacuum setup with the linear Paul trap in the front and sketches the placement of the four necessary laser sources and the associated beam paths.*

This chapter describes the technical realization for an experimental setup with the purpose to produce, confine and investigate Be^+ and H_2^+ ions. In the first section Paul traps are introduced as a possibility to trap charged particles. In the second and third section first the trapping mechanism is reviewed and subsequently a design for a linear Paul trap presented, which suits the requirements. Thereafter follows a description of the beryllium ion source to load the trap with ions. The fifth section presents the the vacuum system. A simple test shows that all the components are working as intended. An overview for the planned H_2^+ source is given in section six. This part is preliminary and the final design may be slightly modified. In the last two sections the imaging system and the experiment control software are presented.

2.1 Paul Traps

harmonic potential

To confine particles at a given point $\mathbf{r}_c$ in space, one needs a restoring force $\mathbf{F}$. For charged particles an electric field $\mathbf{E}$, described by a harmonic potential

$$\Phi = \frac{\Phi_0}{2r_0^2} \cdot \left(\alpha x^2 + \beta y^2 + \gamma z^2\right), \tag{2.1}$$

seems to allow a simultaneous restoring force in all three directions. But a confining electrostatic potential in such a form is not possible, since the Laplace equation $\Delta\Phi = 0$ must be respected. This leads to the condition

$$\alpha + \beta + \gamma = 0 \tag{2.2}$$

for the potential in equation (2.1), and two simple solutions for the parameters are:

$$\alpha = \gamma = 1 \text{ and } \beta = -2, \tag{2.3}$$
$$\alpha = -\beta = 1 \text{ and } \gamma = 0. \tag{2.4}$$

no static 3d confinment

Obviously an electrostatic potential is always repulsive in at least one direction. This obstacle can be overcome by using an alternating electric field between parameters of different sign, which leads to a cycling of the attractive force between the corresponding directions. In the time average a small mean force remains, confining the particles. This

RF trapping

idea was published by Paul in 1958 [37]. The first realization of such an RF ion trap is based on eq. 2.3, which leads to the geometry of the hyperbolic trap (see Fig. 2.2 a) for a sketch). The design of this apparatus and a description can be found for example in Paul's Nobel lecture [38].
For the solution in equation (2.4) an alternating electric field between the $\hat{x}$ and $\hat{y}$ direction has to be established. This leads to the design of

linear trap

the mass spectrometer and the linear Paul trap. The linear design has the advantage of a better accessibility of the center of the trap, making it easier to inject particles or manipulate trapped particles.

different designs

The main working principle, namely an RF field between at least two electrodes in different directions, remains the same for Paul traps, independent of the geometry. However, different tasks lead to a broad

few ions

variety of geometric realizations. In Fig. 2.2 different linear traps are shown. The trap in b) is a so called precision trap from Mainz

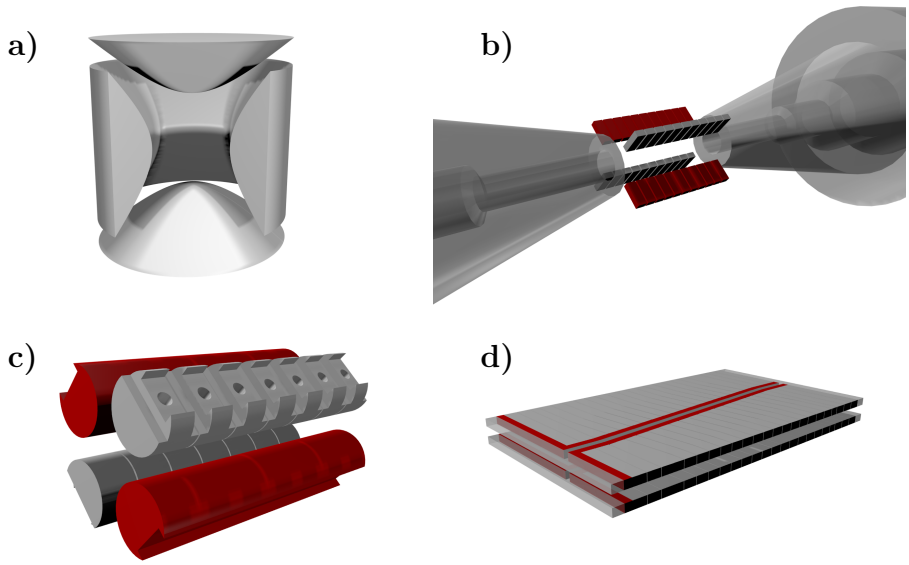

Figure 2.2: *Different Paul traps.* a) *Sketch of a hyperbolic Paul trap. The ring electrode is cut open to show the hyperbolic shape of the electrodes.* b) *A precision trap as it is realized at Mainz university. The eleven fingers are each* 0.2 mm *wide with a spacing of* 0.03 mm. c) *A possible design for the precapture trap in the GBAR project. The length of the red RF electrodes is* 34.8 mm, *and the spacing between the DC electrodes* 0.2 mm. *The total length of this trap is approximately* 15 *times the length of the precision trap.* d) *Two ITO chips, a new technical realization of a linear trap, which is under investigation in Mainz.*

university and is designed to capture single or few ions while being able to manipulate the position of the potential minimum very precisely [39, 40]. The trap shown in c) is designed to confine a laser cooled ion cloud which contains more than $> 10^4$ particles. This trap is larger than the precision trap, since it must accomodate a laser beam to address the ion cloud. New materials and manufacturing techniques lead to designs like in d), a litographically created chip of conducting segments, where the transparent part is created with an indium tin oxide (ITO) coating. This allows for a conducting, but transparent segment on the chip [41].

$> 10^4$ **ions**

The traps b) - c) are also used as design studies for the GBAR project [42]. While b) presents a possible candidate for the final trap, where the photodetachment of $\bar{H}^+$ is planned. The traps c) and d) present design studies for the pre-capture trap.
The following two sections review first the mechanism of a linear Paul trap, and present then, based on the previous considerations, a trap design which is suited for this project.

2.2 A linear Paul Trap

RF and DC potentials

In eq. 2.4 an alternating potential between electrodes in $\hat{x}$ and $\hat{y}$ direction can establish confinement in the $\hat{x}\hat{y}$ plane. To confine particles along the $\hat{z}$ direction additional electrodes are needed. Fig. 2.3 shows an example of a linear Paul trap with its RF electrodes, the center electrodes and the endcaps.

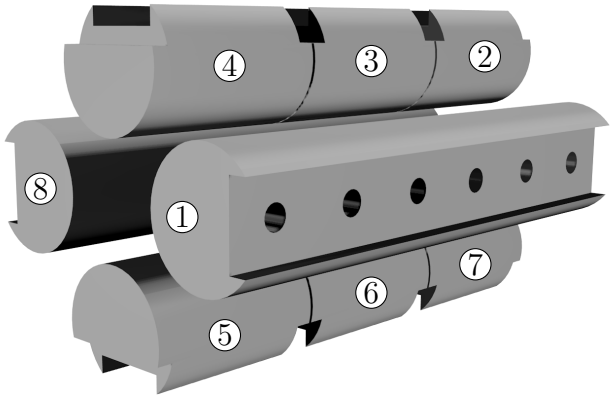

Figure 2.3: *Sketch of a linear Paul trap. Electrodes ① and ⑧ are the RF electrodes. Electrodes ③ and ⑥ are the center electrodes. The remaining ones are the endcap electrodes.*

While the center electrodes are supplied with an RF voltage $V_{RF} = U_0 + V_0 \cos[\Omega t]$, the endcap electrodes are supplied with a constant voltage U_1. The complete potential can be written as:

$$\Phi(x, y, z, t) = \Phi_{RF}(x, y, t) + \Phi_{endc.}(x, y, z) \tag{2.5}$$

In the following two subsections first the $\hat{x}\hat{y}$-confinement and the conditions for a stable RF trapping are derived, then the confinement along the $\hat{z}$-axis with a static DC potential are treated in more detail.

2.2.1 Trapping in the $\hat{x}\hat{y}$-plane

the quadrupole

As a first step in understanding the trapping dynamics in the $\hat{x}\hat{y}$-plane a two dimensional quadrupole is treated. Real linear Paul traps usually do not use hyperbolic electrodes, but rather cylindric ones. In a second step a geometric correction factor κ will be introduced, to account for this difference.

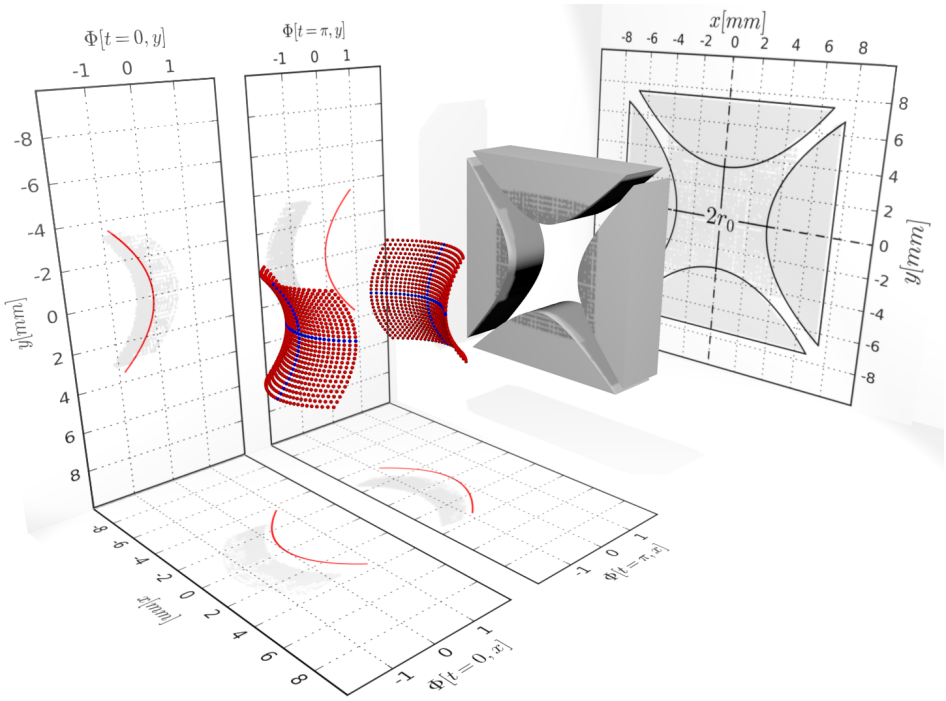

Figure 2.4: *Cross section of hyperbolic electrodes with the inner radius r_0. Also shown is the potential for two different times $t = 0$ and $t = \pi$; the attractive potential is cycling between the electrodes.*

the potential

The hyperbolic electrodes shown in Fig. 2.4 establish a two dimensional quadrupole field in the $\hat{x}\hat{y}$ plane. With $\Phi_0 = U_0 + V_0 \cos[\Omega t]$ the two dimensional potential is

$$\Phi_{RF}(x, y, t) = \frac{(U_0 + V_0 \cos[\Omega t])}{2r_0^2} \left(x^2 - y^2 + r_0^2\right). \tag{2.6}$$

eq. of motion

The electric field is given by $\mathbf{E} = -\nabla\Phi$, so the equations of motion for an ion of mass m and charge q can be written as:

$$\ddot{x} - \frac{q}{mr_0^2}(U_0 + V_0 \cos[\Omega t])\, x = 0, \tag{2.7}$$

$$\ddot{y} + \frac{q}{mr_0^2}(U_0 + V_0 \cos[\Omega t])\, y = 0. \tag{2.8}$$

By using the substitutions

$$a_x = -a_y = \frac{4qU_0}{m\Omega^2 r_0^2} \tag{2.9}$$

$$q_x = -q_y = \frac{2qV_0}{m\Omega^2 r_0^2} \tag{2.10}$$

$$\tau = \frac{\Omega t}{2}, \tag{2.11}$$

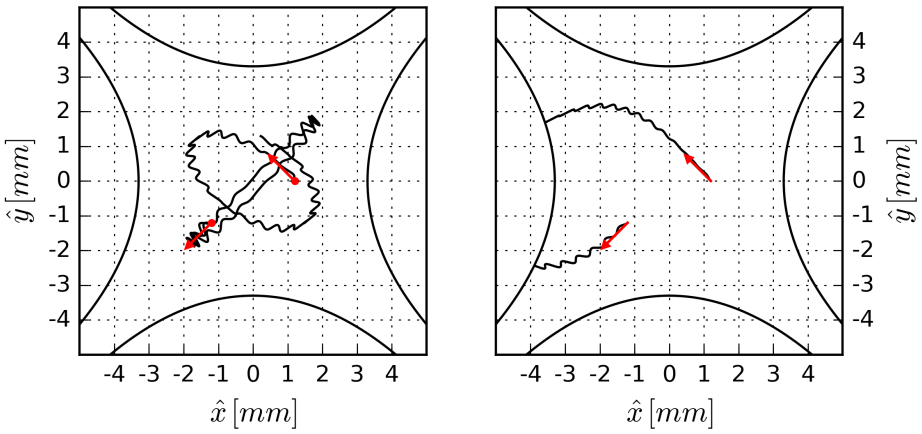

Figure 2.5: *Lissajous like trajectories of two charged particles with mass* 9 amu *and charge* 1 e. *The initial conditions* $\mathbf{x}_i, \dot{\mathbf{x}}_i$ *are the same in both cases, where the red arrow represents the direction of the initial velocity. Left: Stable trajectories with* $\Omega = 2\pi \cdot 13.37\,\mathrm{MHz}$, $V_0 = 518\,\mathrm{V}$ *and* $U_0 = 1\,\mathrm{V}$, *and therefore* $(|a_x|, |q_x|) = (4.96{\cdot}10^{-4}, 0.13)$. *Right: Unstable trajectories with* $\Omega = 2\pi \cdot 13.37\,\mathrm{MHz}$, $V_0 = 200\,\mathrm{V}$ *and* $U_0 = 4\,\mathrm{V}$, *and* $(|a_x|, |q_x|) = (1.98 \cdot 10^{-3}, 0.050)$.

Mathieu equation

the equations of motion can be transformed into a Mathieu equation for both directions $u = x, y$:

$$\frac{\mathrm{d}^2 u}{\mathrm{d}\tau^2} + (a_u + 2q_u \cos[2\tau])\, u = 0. \tag{2.12}$$

unstable and stable solutions

In Fig. 2.5 numerical solutions for different initial conditions and RF voltage parameters are shown. These solutions can be divided into two different categories: unstable and stable solutions. For unstable solutions the trajectory diverges (and the particles collide with the electrodes), while for stable solutions the trajectory is restricted to a finite area in space. The general solution to the Mathieu equation can be written as [37]:

$$u(\tau) = A\, e^{\mu\tau} \sum_{n=-\infty}^{\infty} c_{2n}\, e^{2in\tau} + B\, e^{-\mu\tau} \sum_{n=-\infty}^{\infty} c_{2n}\, e^{-2in\tau}, \tag{2.13}$$

where A and B are constants depending on the initial conditions, and the stability parameter μ and the coefficients c_{2n} depend only on the parameters a_u and q_u. As the name would suggest the stability parameter $\mu = l + im$ determines if the solution $u(\tau)$ describes a unstable or stable solution:

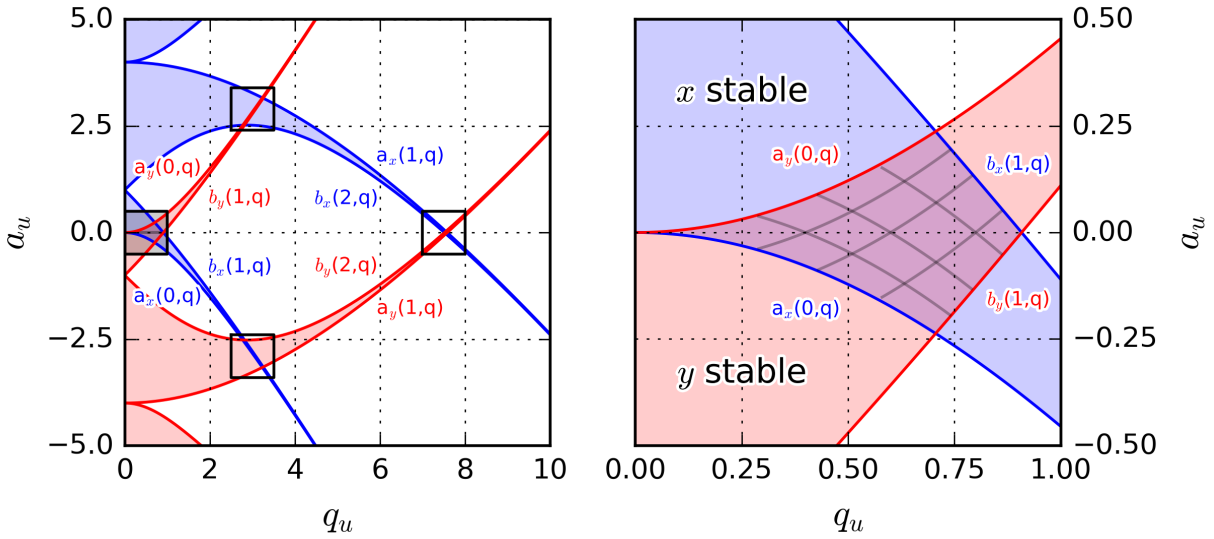

Figure 2.6: *Stability diagram for the Mathieu equation for the linear RF trap. Left: Only the overlapping regions lead to stable solutions. Right: The first stable region.*

- $l \neq 0$: In that case either $e^{\mu\tau}$ or $e^{-\mu\tau}$ diverges and therefore also the solution $u(\tau)$ diverges. This unstable solution leads to the loss of the particle.

- $l = 0$ and $m \in \mathbb{R}$: The particle has a periodic amplitude in the $\hat{x}\hat{y}$ plane and the solution is stable. The solutions with $m \in \mathbb{Z}$ describe the transition between stable and unstable solutions.

stability diagram

The python package *scipy.special* contains special functions, amongst other things also the functions for the characteristic value of the even and odd Mathieu function: `mathieu_a(m,q)` and `mathieu_b(m,q)`. In Fig. 2.6 the functions for $m = 0, 1, 2$ are plotted, which enclose the stable regions for the $\hat{x}$ and $\hat{y}$ direction. To confine a charged particle the trajectory must be stable in $\hat{x}$ and $\hat{y}$ direction, therefore only the overlapping regions in Fig. 2.6 are of interest. Experimentally the region with a smaller q_u and therefore also a smaller voltage is easier to access, for which reason linear Paul traps are usually operated in the first stable region.

Adiabatic Approximation

The trajectory of a charged particle in a time constant field and a rapidly oscillating field can be separated into two components: a smooth secular motion $\mathcal{S}(t)$ and a fast oscillating micromotion $\mathcal{M}(\mathcal{S}, t)$, following the secular motion [43, 44].
In the following an one-dimensional approach outlines this separation. The potential can be expressed by a time independent part $\phi_{\mathcal{S}}(x)$ and an oscillating part $\phi_{\mathcal{M}}(x, t)$, so that one can write for the resulting forces:

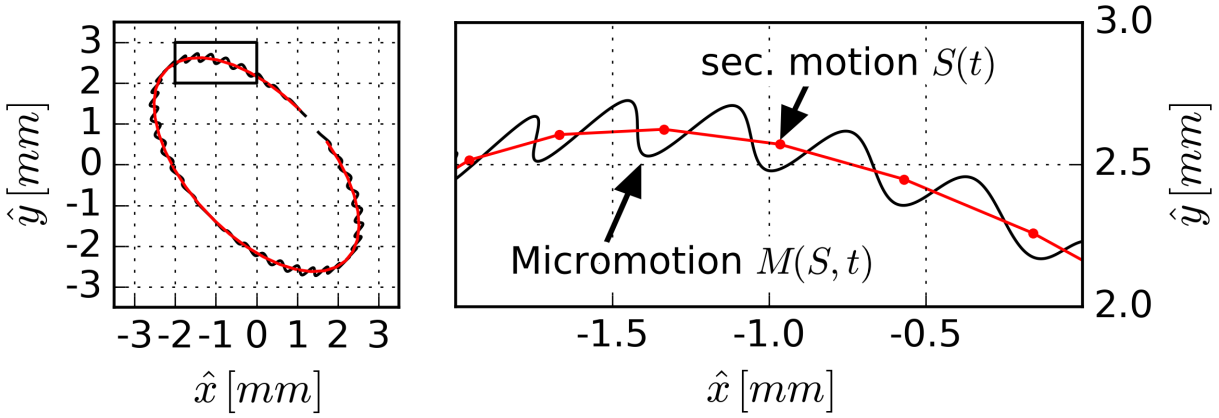

Figure 2.7: *The motion $\mathcal{X}(t)$ can be separated into a secular motion $\mathcal{S}(t)$ and a micromotion $\mathcal{M}(S(t),t)$. The inset of the left panel is shown again on the right side.*

$$F(x) = -q \cdot \frac{\mathrm{d}\phi_{\mathcal{S}}(x)}{\mathrm{d}x} \tag{2.14}$$

$$f(x,t) = -q \cdot \frac{\mathrm{d}\phi_{\mathcal{M}}(x,t)}{\mathrm{d}x} = f_0(x)\,\cos\left[\Omega(t-t_0)\right] \tag{2.15}$$

If now $\mathcal{M} \ll \mathcal{S}$ and $\dot{\mathcal{M}} \gg \dot{\mathcal{S}}$, then $\mathcal{M}$ can be treated as perturbation of $\mathcal{S}$ and one can expand the equation of motion:

$$\begin{aligned} m\,\ddot{\mathcal{S}}(t) + m\,\ddot{\mathcal{M}}(\mathcal{S},t) \;=\; & F(\mathcal{S}) + f(\mathcal{S},t) \\ & + \mathcal{M}\,\partial_x\left(F(x) + f(x,t)\right)|_{\mathcal{S}} + \mathcal{O}(\mathcal{M}^2) \end{aligned} \tag{2.16}$$

Since the smooth and the oscillating part must be separately equal one can write for the oscillating terms:

$$m\,\ddot{\mathcal{M}}(\mathcal{S},t) \;=\; f(\mathcal{S},t) \tag{2.17}$$

Using eq. (2.15) this leads to an expression for $\mathcal{M}$:

$$\mathcal{M}(\mathcal{S},t) = -\frac{f_0(\mathcal{S})}{m\Omega^2}\,\cos\left[\Omega(t-t_0)\right] \tag{2.18}$$

Averaging eq. (2.16) over one period of the micromotion one obtains the secular motion, as shown in Fig. 2.7 on the right side. The fast oscillating terms vanish, so that one can write

$$m\ddot{\mathcal{S}} = F(\mathcal{S}) + \frac{1}{T}\int_0^T \mathcal{M}\,\partial_x f(x,t)|_{\mathcal{S}}\,\mathrm{d}t. \tag{2.19}$$

Using the expression for the force from eq. (2.15) and for the secular motion from eq. (2.19) one can write:

$$m\ddot{\mathcal{S}} = F(\mathcal{S}) - \frac{1}{2m\Omega^2}\; f_0(x)\,\partial f_0(x)|_{\mathcal{S}}\,, \tag{2.20}$$

which can be rewritten

$$m\ddot{\mathcal{S}} = -\partial_x \left(q\phi_{\mathcal{S}}(x) + \frac{q^2}{4m\Omega^2}\left(\partial_x\phi_{\mathcal{M}}(x)\right)^2\right)\Big|_{\mathcal{S}}. \tag{2.21}$$

One can now identify the pseudopotential energy: **pseudo potential**

$$\phi_{pseudo}(x) = \frac{q^2}{4m\Omega^2}\left(\partial_x\phi_{\mathcal{M}}(x)\right)^2 \tag{2.22}$$

And rewrite the secular potential energy:

$$\phi_{sec}(x) = q\,\phi_{\mathcal{M}}(x) + \phi_{pseudo}(x). \tag{2.23}$$

This calculation can be generalized to three dimensions. With the time depending part in eq. (2.6) this leads to the pseudopotential energy

$$\phi_{pseudo}(x,y) = \frac{q^2V_0^2}{4m\Omega^2 r_0^4}\,(x^2+y^2). \tag{2.24}$$

This expression shows that the pseudopotential is confining in the $\hat{x}$ and $\hat{y}$ direction. Finally, the complete secular potential energy in the $\hat{x}\hat{y}$-plane is

$$\phi_{sec}(x,y) = \frac{q^2V_0^2}{4m\Omega^2 r_0^4}\,(x^2+y^2) + \frac{qU_0}{2r_0^2}\,(x^2-y^2). \tag{2.25}$$

It can be written in terms of secular oscillation frequencies as **secular frequencies**

$$\begin{aligned}\phi_{sec}(x,y) &= \frac{1}{2}\,m\,\widetilde{\omega}^2(x^2+y^2) + \frac{1}{2}\,m\,\omega_0^2(x^2-y^2) \\ &= \frac{1}{2}\,m\,\left(\widetilde{\omega}^2+\omega_0^2\right)x^2 + \frac{1}{2}\,m\,\left(\widetilde{\omega}^2-\omega_0^2\right)y^2, \end{aligned} \tag{2.26}$$

with

$$\widetilde{\omega}^2 = \frac{q^2V_0^2}{2m^2\Omega^2r_0^4} \text{ and } \omega_0^2 = \frac{qU_0}{mr_0^2}.$$

These frequencies can also be expressed in terms of the parameters a_u, q_u and Ω

$$\widetilde{\omega}^2 = \frac{q_u^2\Omega^2}{8} \text{ and } \omega_0^2 = \frac{a_u\Omega^2}{4},$$

so that one can write:

$$\omega_{x/y}^2 = \frac{\Omega^2}{4}\left(\frac{q_u^2}{2} \pm a_u\right). \tag{2.27}$$

potential depth

The potential depth can be estimated using eq. 2.26 as the effective potential at the electrode location:

$$\phi_{sec,depth} = \frac{q^2V_0^2}{4m\Omega^2r_0^2} \pm \frac{qU_0}{2}. \tag{2.28}$$

cylindrical electrodes

Mathieu's differential equation assumes hyperbolically shaped electrodes as boundary conditions. These are difficult to produce, and in 1958 Paul, Reinhard and von Zahn replaced the hyperbolic electrodes successfully by electrodes with a circular cross section with $r_e/r_0 = 1.16$ [37].

With the increasing computer power it was shown in 1971, that a ratio of $r_e/r_0 = 1.1468$ leads to an even better approximation of the quadrupole field [45]. Nowadays it is easy to verify these results. The potential distribution in a quadrupole with circular cross section can be expressed as a series [45]:

$$\Phi(x,y,t) = \left(U_0 + V_0\cos\left[\Omega t\right]\right)\sum_{n=0}^{\infty} C_n\left(\frac{r}{r_0}\right)^{2(2n+1)}\cos\left[2\left(2n+1\right)\theta\right] + \frac{1}{2}. \tag{2.29}$$

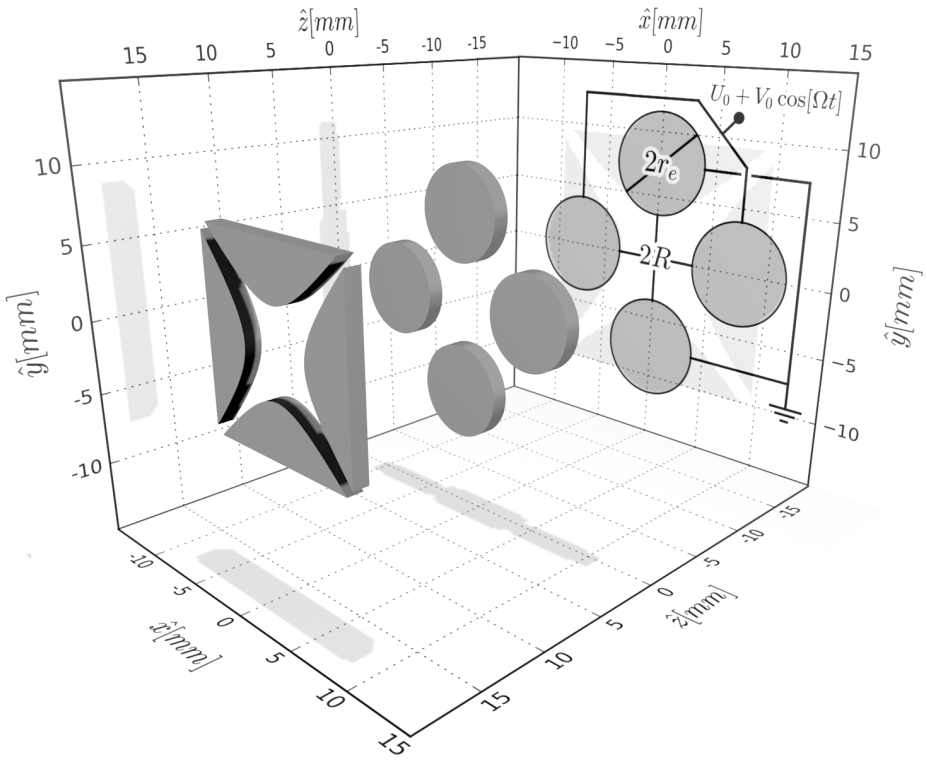

Figure 2.8: *Cross section of cylindrical electrodes for a linear Paul trap. The characteristic parameters are R, the distance between the trap center and the electrodes, and the radius for the cylindric electrodes, r_e.*

The first term is the quadrupole term, the second one a 12-pole term, etc. The best approximation to a pure quadrupole potential is an electrode radius such that the 12-pole coefficient C_1 disappears, all higher contributions are magnitudes of order smaller.
Transforming eq. (2.29) into cartesian coordinates and using some trigonometric identities one can write for the potential along the $\hat{x}$ axis for $U_0 = 0$ and $t = 0$:

$$\Phi(x, y = 0, t = 0) = V_0 \left(C_0 \frac{x^2}{r_0^2} + C_1 \frac{x^6}{r_0^6} + \dots \right) \tag{2.30}$$

Here an effective radius r_0 was introduced, which is expected to be close to R.

SIMION

An option to simulate the potential which is caused by multiple electrodes is the commercial software SIMION 8.1. This software can be used to define the geometry of the electrodes via `.gem`-files. It then solves the Laplace equation numerically on a mesh, where the resolution of the mesh is 1 point/mm. In order to obtain a better resolution all the following results are obtained with a $^{10}/_{1}$ scaled geometry. The result for each independent electrode is saved in a so called `.patxt`-file

format, and then imported into Python 3. Here the potential arrays are rescaled to a newly defined voltage for the corresponding electrode. The geometry is also rescaled. Thereafter the total potential caused by the i independent electrodes can be summed up:

$$\Phi_{\mathrm{SIM,DC}}(x, y, z) = \sum_i \Phi_i(x, y, z) \tag{2.31}$$

To determine the values of the coefficients C_0 and C_1 the geometry of four cylindric electrodes with the parameters $R = 3.5\,\mathrm{mm}$, $l = 12\,\mathrm{mm}$ and $r_e = 2.975\,\mathrm{mm}, 3.325\,\mathrm{mm}, \ldots$ was defined in multiple `.gem`-files (an example file and an overview of the resulting geometry can be found in the appendix A.1). The mesh consists in each case of $261 \cdot 261 \cdot 141$ points. The results were imported to python and rescaled such, that each two opposite set of electrodes have the same voltage, the two RF electrodes with 1 V and the other two electrodes with 0 V. Thereafter the total potential $\Phi_{\mathrm{SIM,DC}}$ along the $\hat{x}$ axis was fitted with the first two terms of eq. 2.30. In fig. 2.9 the coefficients C_0 and C_1 are plotted as a function of the ratio r_e/R. For a ratio of $r_e/R = 1.15 \pm 0.01$ the contribution of the 12-pole term vanishes, and the approximation with a pure quadrupole potential is best justified. These calculations agree with what can be found here [46], where a more detailed analysis is carried out.

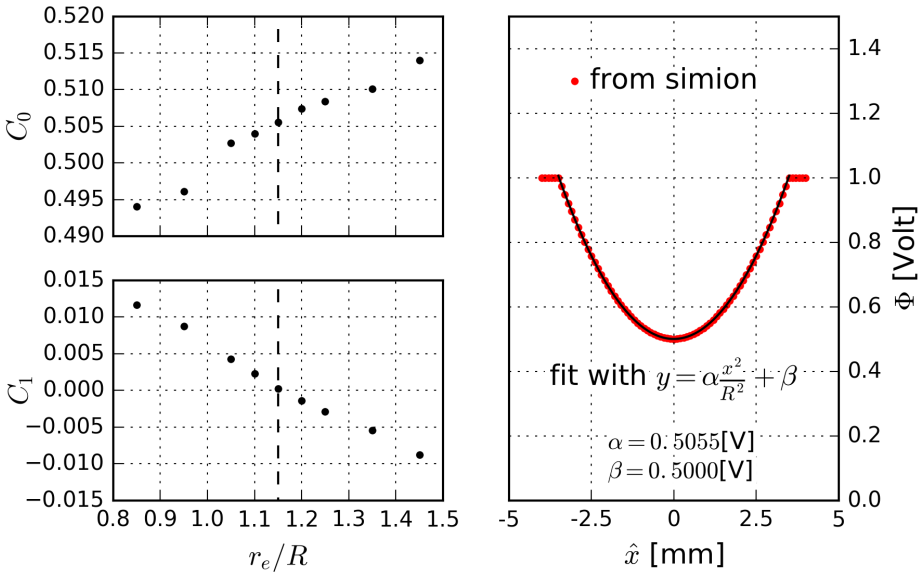

Figure 2.9: *Left: Coefficients C_0 and C_1 for different ratios r_e/R. Right: Data points from SIMION for $r_e/R = 4.0/3.5 = 1.1429$ and a pure quadrupole fit.*

correction factor κ

In the case of our trap this ratio is not the ideal value, since $r_e/R = 4.0/3.5 = 1.1429$, which is slightly smaller. Therefore the 12-pole term does not vanish completely, and one obtains $C_0 = 0.5055$ and $C_1 =$

3.823810^{-4}. In the practical case one is interested in the region in the proximity of the trap center, so that $r/r_0 \ll 1$. Therefore $C_0 \left(r/r_0\right)^2 \gg C_1 \left(r/r_0\right)^6$ and the quadrupole approximation is valid.
The fit with a pure quadrupole term of the form $\alpha \cdot x^2/r_0^2 + \beta$ leads to $\beta = 0.500$ and to $\alpha = 0.5055$. The discrepancy between the theoretic value $\alpha_{th} = 1/2$ and the value from the fit can be explained by the fact that not all higher order terms in eq. 2.29 become zero. By introducing

$$r_0 = \kappa R \tag{2.32}$$

and demanding $\alpha \cdot x^2/R^2 \stackrel{!}{=} x^2/2r_0^2$ one obtains for the geometric correction factor $\kappa = 0.9945$. This correction factor has to be taken into account when deriving the secular frequencies (see section 2.2.3).

2.2.2 Trapping in the $\hat{z}$-direction

In the section before it was shown how trapping in the $\hat{x}\hat{y}$ plane can be achieved using an RF potential. Confinement along the $\hat{z}$-direction can be accomplished by applying DC potentials at the endcap electrodes.

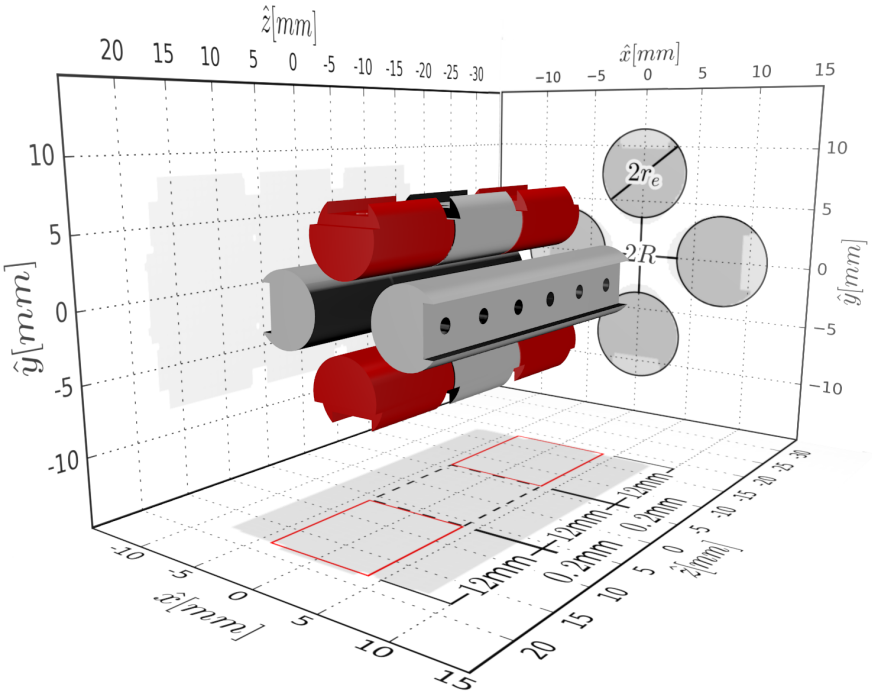

Figure 2.10: *Design for a linear Paul trap, consisting of RF and center electrodes (light grey), and four endcap electrodes (dark red) for confinement along the $\hat{z}$-direction.*

endcaps

In fig. 2.10 the endcap electrodes are highlighted. The RF electrodes are not segmented. One can see that with positive endcap voltage the potential is confining along the $\hat{z}$ direction and deconfining along the $\hat{x}$ and $\hat{y}$ directions. Close to the center of the trap, the potential has a quadrupolar behaviour that is modeled by

$$\Phi_{endc.}(x,y,z) = \frac{U_1}{2z_{eff}^2} \cdot \left[z^2 - 1/2\left(x^2+y^2\right)\right] + \gamma, \tag{2.33}$$

where U_1 is the voltage applied to the endcap electrodes. To estimate the effective parameter z_{eff} for the specific geometry shown in fig. 2.10 SIMION 8.1 was used again. The `.gem`-file with a mesh of $241 \cdot 241 \cdot 401$ points can be found in the appendix A.2.
After preparing the results in python 3 the endcap electrodes were scaled to 1 V and all other electrodes to 0 V. The total potential $\Phi_{\text{SIM,DC}}(x,y,z)$ along the $\hat{x}$, $\hat{y}$ and $\hat{z}$ axis was plotted and can be seen in fig. 2.11.

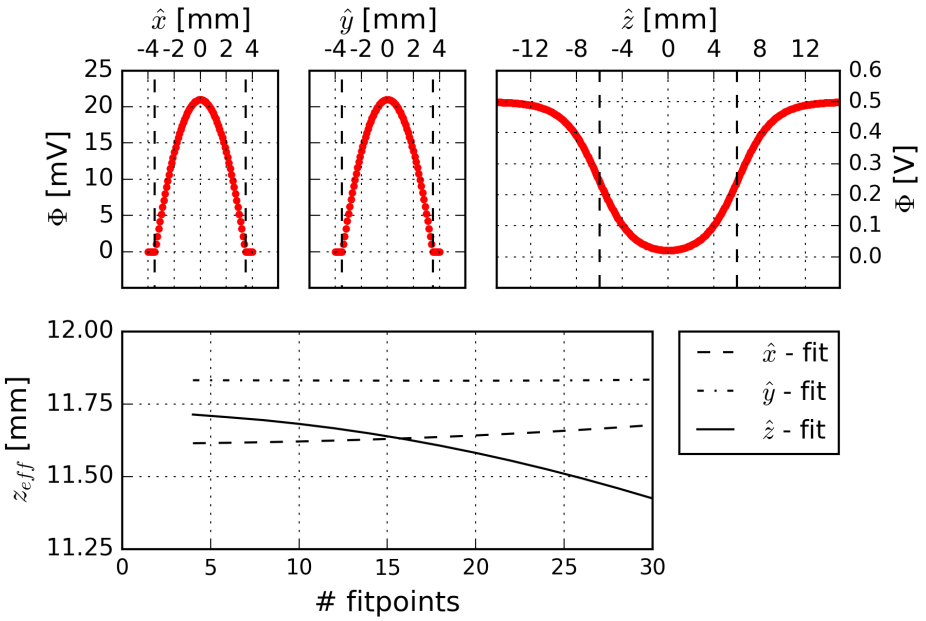

Figure 2.11: *Top: SIMION potential along the $\hat{x}$, $\hat{y}$ and $\hat{z}$ axis for the geometry shown in Fig. 2.10. At the endcaps the applied voltage is 1 V, and 0 V elsewhere. Bottom: Adjustment of the parameter z_{eff} depending on the number of points which are used to fit the potential.*

effective length

This result has been fitted with the expression in eq. 2.33. The bottom part of fig. 2.11 shows the dependency of z_{eff} for the three axes, when varying the fit intervall around $x, y, z = 0$. One can estimate the value for the effective length with $z_{eff} \approx 11.7\,\text{mm}$. This is approximately twice the size of the half electrode distance with 6.2 mm, which can be expected since the RF electrodes are not seg-

mented. The potential minimum is consistent in all three dimensions with $\gamma = \Phi_{\mathrm{SIM,DC}}(0,0,0) = 0.021\,\mathrm{V}$.

2.2.3 The Effective Potential

With the investigations of the last two sections eq. (2.5) can be rewritten in order to gain some quantitative insight to the effective trapping potential. First the RF part can be replaced with the expression for the secular potential in eq. (2.25) with $r_0 = \kappa \cdot R$, where $\kappa = 0.9945$. In a next step the endcap potential is replaced with eq. (2.33), with $z_{\mathrm{eff}} = 11.7\,\mathrm{mm}$. By sorting the equation by variable we finally obtain an expression for the effective potential energy:

$$\begin{aligned}\phi_{\mathrm{eff}}(x,y,z) = &\left(\frac{q^2V_0^2}{4m\Omega^2r_0^2} + \frac{qU_0}{2r_0^2} - \frac{1}{2}\frac{qU_1}{2z_{\mathrm{eff}}^2}\right)\cdot x^2 \\ &+\left(\frac{q^2V_0^2}{4m\Omega^2r_0^2} - \frac{qU_0}{2r_0^2} - \frac{1}{2}\frac{qU_1}{2z_{\mathrm{eff}}^2}\right)\cdot y^2 + \frac{U_1}{2z_{\mathrm{eff}}^2}\cdot z^2 \end{aligned} \quad (2.34)$$

one can identify the different contributions from the RF potential and the endcap potential. Using eq. (2.26) we can further simplify and obtain a final expression for the effective potential:

$$\phi_{\mathrm{eff}}(x,y,z) = \frac{1}{2}\,m\left(\omega_x^2x^2 + \omega_y^2y^2 + \omega_z^2z^2\right) \quad (2.35)$$

with

$$\omega_{x/y}^2 = \widetilde{\omega}^2 \pm \omega_0^2 - \frac{1}{2}\omega_z^2 \text{ and } \omega_z = \frac{q}{m}\frac{U_1}{z_{eff}}. \quad (2.36)$$

In Table 2.1 frequencies for typical operating parameters can be found.

species	V_0	a_x	q_x	ω_x[kHz]	ω_y[kHz]	ω_z[kHz]
H_2^+	200 V	$2.26\cdot10^{-4}$	0.226	1069.5	1060.0	94.5
Be^+	200 V	$5.02\cdot10^{-5}$	0.050	239.7	230.2	44.5
H_2^+	518 V	$2.26\cdot10^{-4}$	0.585	2764.2	2760.5	94.5
Be^+	518 V	$5.02\cdot10^{-5}$	0.130	615.1	611.4	44.5

Table 2.1: *Eigenfrequencies for different RF voltage amplitudes,* $\Omega = 2\pi\cdot 13.37\,\mathrm{MHz}$, $U_0 = 0.1\,\mathrm{V}$ *and* $U_1 = 1\,\mathrm{V}$.

One can use the parameters $\Omega = 2\pi\cdot13.37\,\mathrm{MHz}$, $r_0 = \kappa\cdot3.5\,\mathrm{mm}$ and m to plot the region of the first stability diagram of Fig. 2.6 as a function of the voltages U_0 and V_0, as shown in Fig. 2.12 on the top.

mass spectrometer

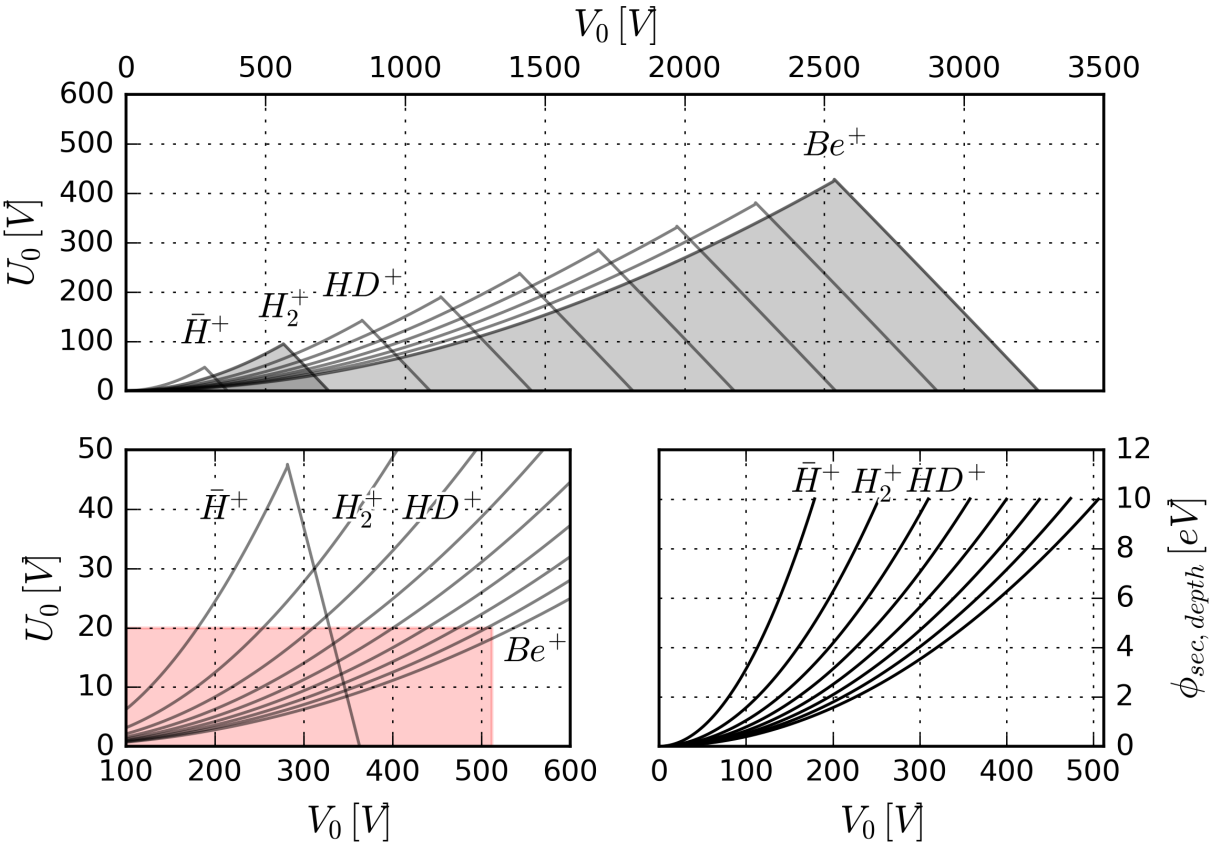

Figure 2.12: *Analysis for the trap realization of section 2.3 Top: Stability diagrams for the masses* $m = 1\,\text{amu} - 9\,\text{amu}$. *Bottom left: The colored background marks the parameter space which is accessible with the setup of section 2.3. Bottom right: The trap depth for different masses.*

Based on this plot the working mechanism of a mass spectrometer can be explained: By changing simoultaneously U_0 and V_0 with a fixed ratio, such that only the stability of one species overlaps with the setting of the trap, one can confine distinct species.
Bottom left of the Fig. 2.12 shows the parameter space which can be accessed wih the potential supplys described in section 2.3. By changing U_0 it should be possible to deplete the trap of heavy particles. The potential depth depends quadratically on V_0 as one can see in Fig 2.12 at the bottom right. For high values of the trap depth the adiabatic approximation is not valid anymore and the confinement of the particles is not stable anymore. One can also see, that having the same charge, lighter particles are trapped tighter than heavier ones.

asymmetric potentials

The expression for the effective potenial derived in the section before allows to estimate the motional frequencies ω_x, ω_y and ω_z. However, this works only for symmetric potentials, i.e. the same endcap potential U_1 at all four endcap electrodes and the same potential at the

center electrodes U_0. Therefore the effect of patch potentials or the movement of the potential minimum (and therefore the movement of the cloud in the trap) by different DC voltages cannot be investigated. As demonstrated below, an analysis with SIMION allows to investigate these effects of different DC potentials at the eight electrodes, while including the pseudo potential to take the RF trapping into account. The `.gem`-file ca be found in the appendix A.3.

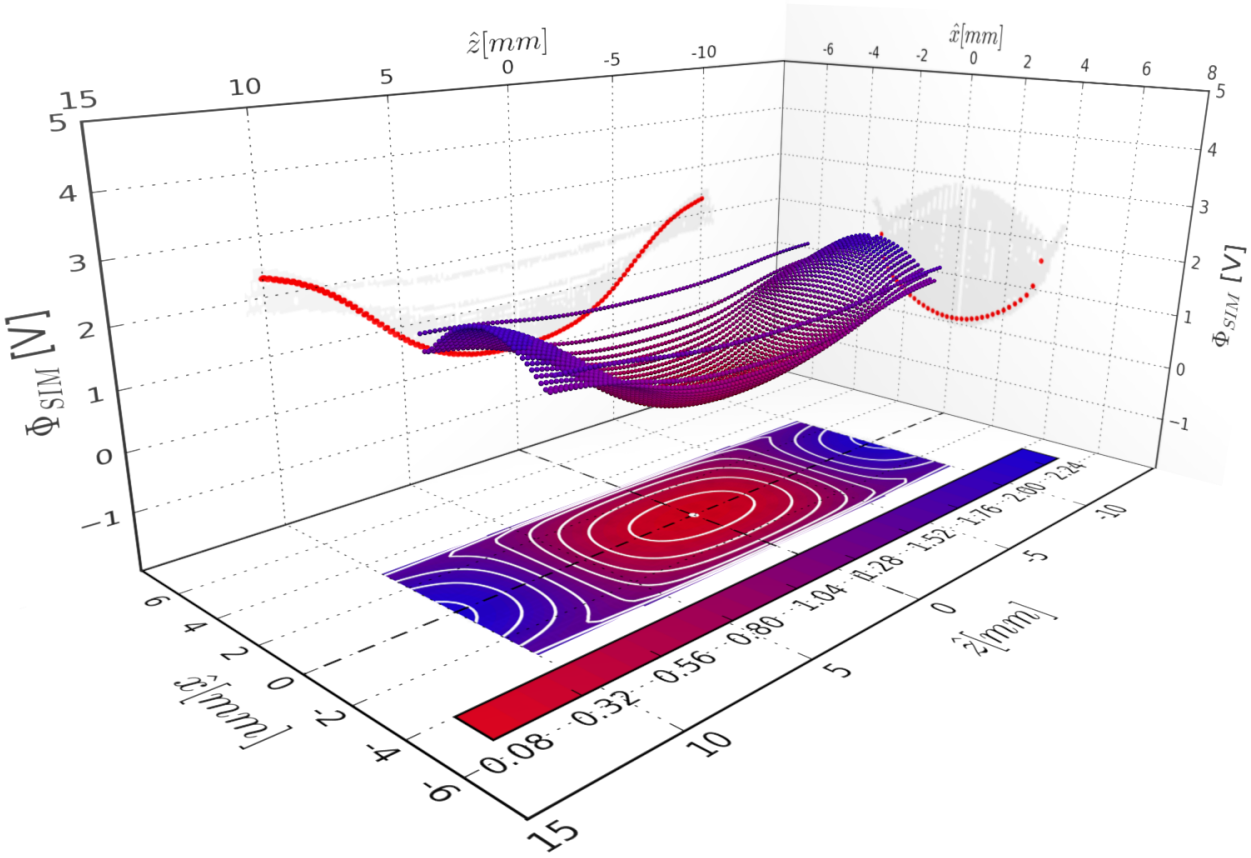

Figure 2.13: *SIMION analysis for the effective potential* $\Phi_{SIM}(x, y, z)$ *for* $\Omega = 2\pi \cdot 13.37\,\mathrm{MHz}$, $V_0 = 200\,\mathrm{V}$, $U_0 = 0.0\,\mathrm{V}$ *and* $U_1 = 5\,\mathrm{V}$

The potential can be written as a sum of the pseudopotential and the static potential applied to the eight electrodes:

$$\Phi_{\mathrm{SIM}}(x, y, z) = \Phi_{\mathrm{SIM,\ pseudo}}(x, y, z) + \Phi_{\mathrm{SIM,\ DC}}(x, y, z) \tag{2.37}$$

The part for the pseudopotential is numerically solved, using equation (2.22), and thereafter the DC arrays are added. Fig. 2.13 shows $\Phi_{\mathrm{SIM}}(x, y = 0, z)$ between the trap electrodes for a symmeric potential. In fig. 2.14 the consequence of some patch potentials on the position of the potential minimum is shown. Asymmetric potentials at the endcaps have a smaller influence on the position of the ion cloud than at the center electrodes.

a) no defect

b) defect at electrode ④

c) defect at electrode ③

d) defect at electrode ①

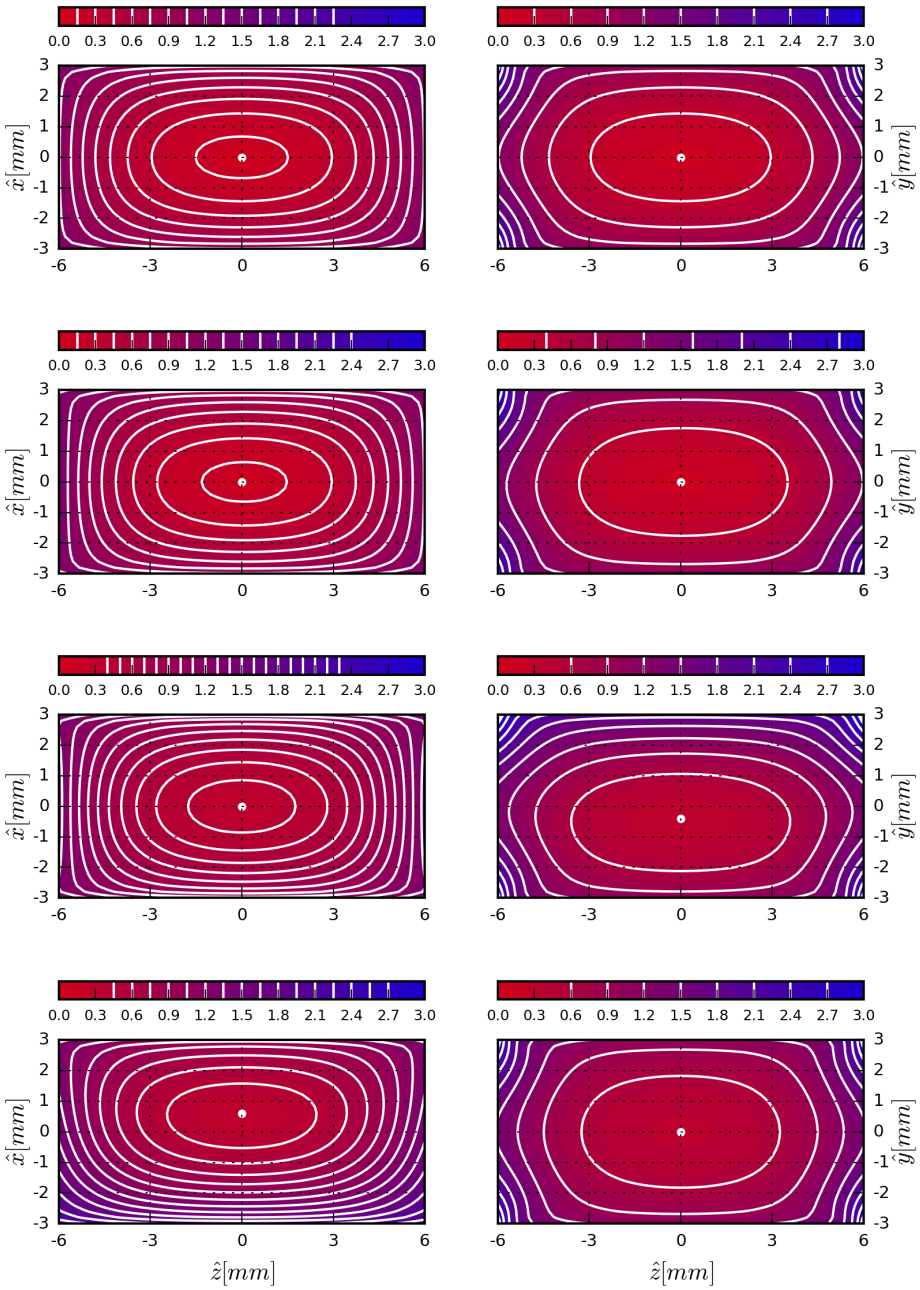

Figure 2.14: *SIMION analysis for the effective potential* $\Phi_{SIM}(x, y, z)$ *in the* $\hat{x}\hat{z}$ *plane (left) and the* $\hat{y}\hat{z}$ *plane (right). The basic parameter configuration in each case is* $\Omega = 2\pi \cdot 13.37\,\mathrm{MHz}$, $V_0 = 200\,\mathrm{V}$, $U_0 = 0.0\,\mathrm{V}$ *and* $U_1 = 5\,\mathrm{V}$.
The first case a) shows the case of perfectly symmetric applied potentials. In case b) the endcap electrode ④ is charged with $6\,\mathrm{V}$. *The potential minimum does not change the position. In the case c) the center electrode ③ is charged with* $1\,\mathrm{V}$. *The potential minimum moves in the* $\hat{y}\hat{z}$ *plane by* $0.4\,\mathrm{mm}$. *In the last case d) the RF electrode ① is charged with* $1\,\mathrm{V}$, *which moves the center of the potential minimum by* $0.6\,\mathrm{mm}$ *in the* $\hat{x}\hat{z}$ *plane.*

2.3 Design and Implementation of a linear Paul Trap

The task for this trap is to confine a few hundred molecular hydrogen ions in a laser cooled beryllium Coulomb crystal. In the previous section it was shown that the kind of particle one wishes to trap and the size of the trap imposes the trap voltages in a certain regime.

size of ion cloud

Suitable Coulomb crystals contain a few thousand ions and have a dimension of approximately 1 mm in length and up to a couple of hundred μm in width [47, 32]. In Fig. 2.15 the result of a numerical simulation for such a mixed species Coulomb crystal is shown. This kind of cloud could be accomodated in a relatively small trap.

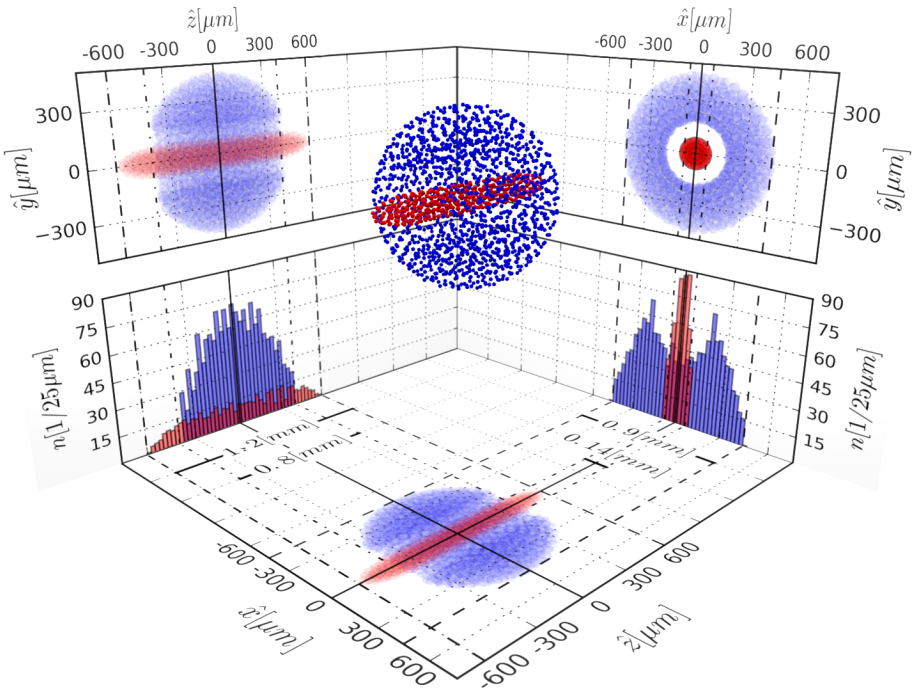

Figure 2.15: *A typical Coulomb crystal composed of* 1469 Be^+ *ions and* 450 H_2^+ *ions, where the stability parameters for* Be^+ *are* $a_x = 5.25 \cdot 10^{-7}$ *and* $q_x = 0.0223$*, and the axial frequency* $\omega_z = 2\pi \cdot 250\,\mathrm{kHz}$*. This is the result of a numerical simulation, details in [32].*

optical access

However, once the ions are trapped one needs good optical access to manipulate the particles. For some of the needed laser sources in this experiment (see 2.3.1) there are no window materials and coatings which allow good transmission at all the wavelengths. Therefore multiple windows need to be installed. In our case the size of the trap and the vacuum chamber is governed by the size and divergence of the laser beams needed. The most stringent constraint is caused by the infrared 9.17 μm H_2^+ two-photon excitation source.

loading ions

As a last constraint the trap must allow to be loaded with ions . In this experiment a beryllium oven and an electron gun are used, which are mounted below the trap (see 2.4), and a H_2 molecular beam apparatus

was constructed and tested (see 2.6 and [32]).

2.3.1 Trap Accessibility

The trap and vacuum chamber have been designed to accomodate the following laser beams:

- a continous wave 313 nm laser for Be^+ cooling
- a pulsed 303 nm (or 202 nm) REMPI laser for H_2^+ creation
- a continous wave 9.17 μm H_2^+ two-photon excitation laser
- a pulsed 213 nm H_2^+ dissociation laser
- a 235 nm laser for ionization of Be (not yet implemented).

In addition, the trap needs to allow access for

- imaging to a CCD camera
- H_2^+ molecular beam
- a neutral Be beam
- electrical feedthroughs for trap, Be^+ source and cavity

multiple windows

The UV beams can in principle share the same windows, while for others like the spectroscopy laser at 9.17 μm and the cooling beam at 313 nm there are no technological solutions for simultaneous high transmission. This obliges one to use different windows for these beams and therefore makes angles between laser beams necessary. This setup is designed to allow optical access to at least three different laser sources with non-compatible transmission properties.

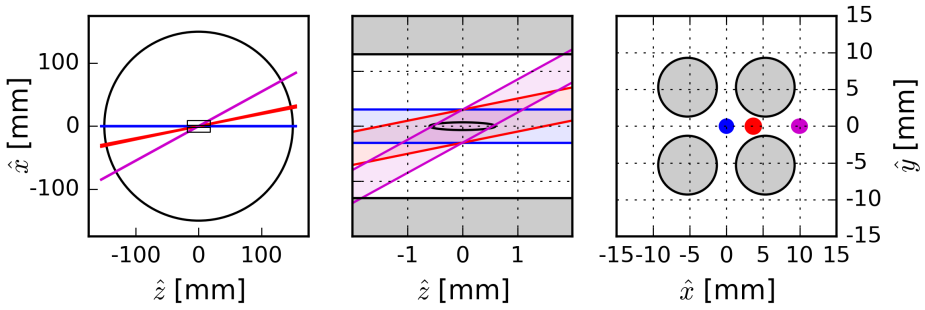

Figure 2.16: *Left: Arrangement of the trap and the laser beams for cooling (at 0.0 °, blue), spectroscopy (at 11.45 °, red) and dissociation (at 28.5 °, purple). Center: Enlargement of the trap center. A beamwaist of 300 μm at the trap center overlaps a sketched ion cloud with the dimensions of the H_2^+ cloud in Fig. 2.15. Right: Cut surface of the laser beams at the entrance of the trap.*

As noted above, the 313 nm and the 9.17 μm laser cannot share a common viewport. However, for both beams the preferred axis would be along the trap axis, in order to obtain the biggest overlap between the beams and the ion cloud (Fig. 2.16, center image). The smallest available viewports (CF16) and an inner diameter of 298.5 mm for the main chamber lead to an angle of 11.45 ° for the spectroscopy laser at 9.17 μm.

cavity

In order to be able to address all the trapped H_2^+ ions, the beam waist at the center of the ion cloud should be as large as possible. On the other hand the needed intensity for the two-photon transition makes a beam waist as small as possible desirable. A trade off is achieved with a beamwaist of $\approx 300\,\mu$m. The transition probability at resonance is given by [48]

$$\Gamma_{\nu\nu'} = \left(\frac{4\pi a_0^3}{\hbar c}\right)^2 \frac{4I^2}{\Gamma_f}\,(1+\epsilon)^4 \left|Q_{\nu\nu'}\left(\frac{E_\nu + E_{\nu'}}{2}\right)\right|^2, \tag{2.38}$$

with the intensity I, the linewidth of the transition Γ_f, and the two-photon transition operator $Q_{\nu\nu'}$. For $\nu = 0$, $\nu' = 1$ and $L = 2$ the two-photon transition operator evaluates to $Q_{01}(L=2) = 0.199$ [49]. Assuming an optical power of 10 W and a beam waist of 300 μm, one ends up with an intensity of $I = 70.7\,{}^{W}/_{\mathrm{mm}^2}$. Together with an estimation for the linewidth $\Gamma_f = 2\pi\,10^4\,\mathrm{s}^{-1}$ the transition probability is $\Gamma_{01} \approx 44\,\mathrm{s}^{-1}$, which is sufficient for trapped H_2^+ ions. However, to reach the required intensity for the two-photon transition an intra-vacuum cavity for the spectroscopy laser is needed. To accomodate the cavity in the vacuum chamber, the latter can not be too small (see Fig. 2.16 on the left side).

beam divergence

The high intensity for the spectroscopy laser leads to the major designing constraint, namely that clipping of the beam by the electrodes must be avoided. At 9.17 μm the divergence of the beam must be taken into account. The radius of a Gaussian beam with waist w_0 located at $z = 0$ depends on its wavelength and can be written [50]

$$w(z) = w_0 \cdot \sqrt{1 + \left(\frac{\lambda z}{\pi w_0^2}\right)^2} \tag{2.39}$$

and its beam divergence angle is

$$\theta = \frac{\lambda}{\pi w_0}, \tag{2.40}$$

which is for a wavelength of 9.17 μm approximately 30 times larger than in the UV. In order to estimate the minimum distance between

the trap electrodes, one can calculate the fraction of power of a Gaussian beam with waist w_0 which is within a circle of radius R. This is given by

$$p = 1 - \exp\left[-\frac{2R^2}{w_0^2}\right]. \tag{2.41}$$

Table 2.2 gives an overview of the loss of power outside a circle with multiples of the beamwaist as radius.

radius	$1\,w_0$	$2\,w_0$	$3\,w_0$
loss	0.135	$3.4 \cdot 10^{-4}$	$1.5 \cdot 10^{-8}$

Table 2.2: *Losses for different radii.*

For the cavity we aim at a Finesse of > 1000. With the definition of the Finesse $\mathcal{F}$ as

$$\mathcal{F} = \frac{\pi}{\text{losses of the cavity}}$$

one can see that with a radius of $\geq 3 \cdot w_0$ the losses are negligible. To make sure no power is lost at the electrodes, the distance between the trap electrodes is choosen such that it is at least 3 times the beam diameter after propagating 18.2 mm (Fig. 2.16, right image).

trap dimensions

A trap with an electrode radius of $r_e = 4\,\text{mm}$ and $R = 3.5\,\text{mm}$ fulfills this requirement. The design shown in Fig. 2.17 respects the above mentioned points and allows for multiple electric feedthroughs. In Table 2.3 the angles for the optical axes and the feedthroughs are displayed. The beryllium source is mounted below the trap, and the chamber is closed with a custom flange which includes a reentrant window to monitor the ions from above.

position	B/K	C/L	D/M	E	F/O	G	H/Q	I	J	N	P	R	A
angle °	0	11.5	28.5	52	70.4	90	115	135	150	232	270	315	330

Table 2.3: *Angles of feedthroughs with respect to the $\hat{z}$ axis of the trap.*

The electrodes were mounted on four Al_2O_3 bars to ensure electric insulation between the electrodes (Fig. 2.17). To prevent deforming the electrode shape each of the electrodes is contacted by the screws which position the electrodes on the bars. The Al_2O_3 bars are fixed on two stainless steel holders, which are shaped to allow optical access along the relevant axes in Fig. 2.17. The holders are connected to two copper corpi, one on top and one from below, while the lower block accomodates the beryllium oven and the e-gun.

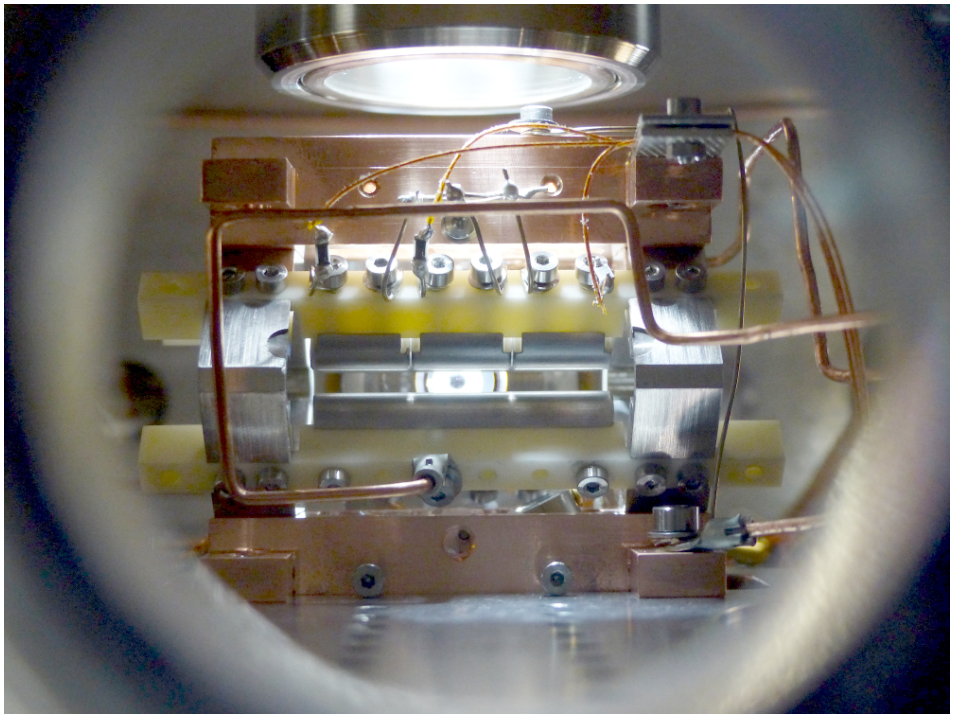

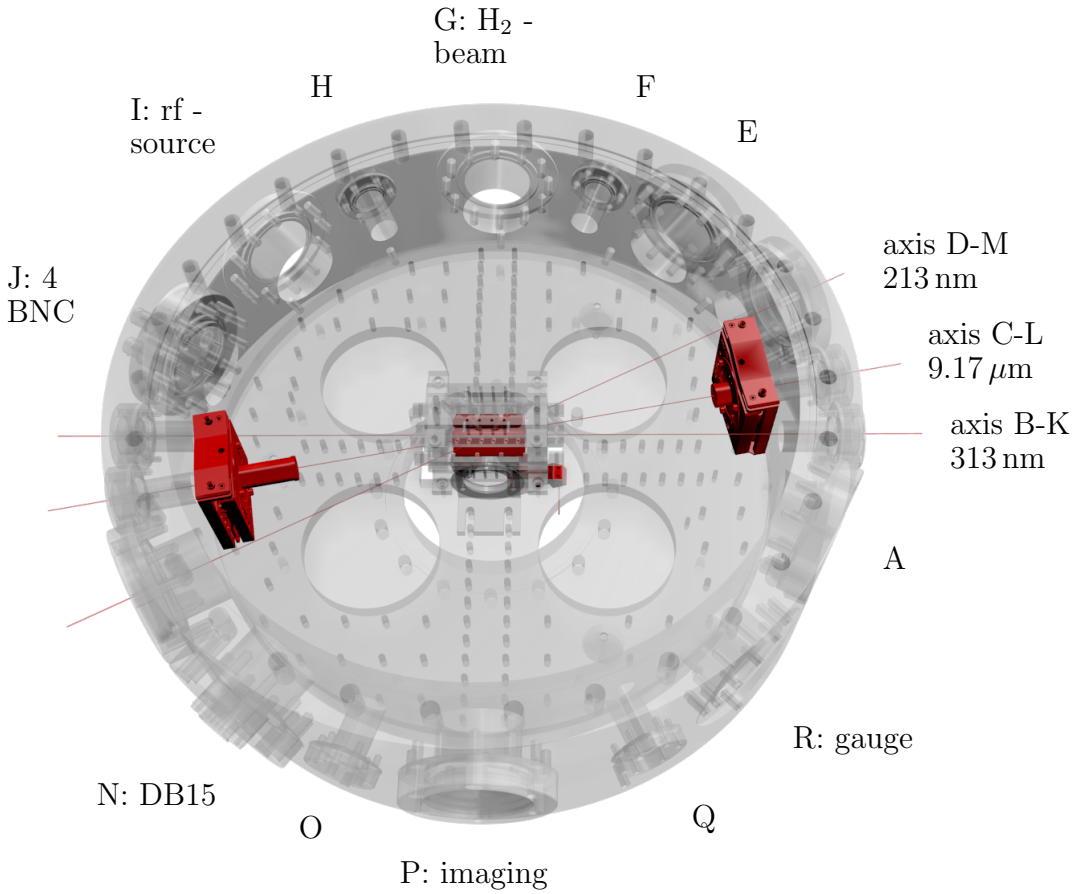

Figure 2.17: *Top: The mounted trap, as seen from position G. Bottom: Design of the vacuum chamber with trap and cavity.*

2.3.2 DC Voltage Supply

The linear trap in this experiment needs

- eight, individually controllable and stable DC voltage channels
- two RF voltage channels up to 600 V.

Each of the DC channels is applied at one of the electrodes 1 to 8, while the RF channels are connected to the RF electrodes 1 and 8 (See Fig. 2.18). A DB-15 wire provides the connection to the DCelectrodes, while the connection to the RF electrodes is done with a copper wire with a diameter of 1 mm.

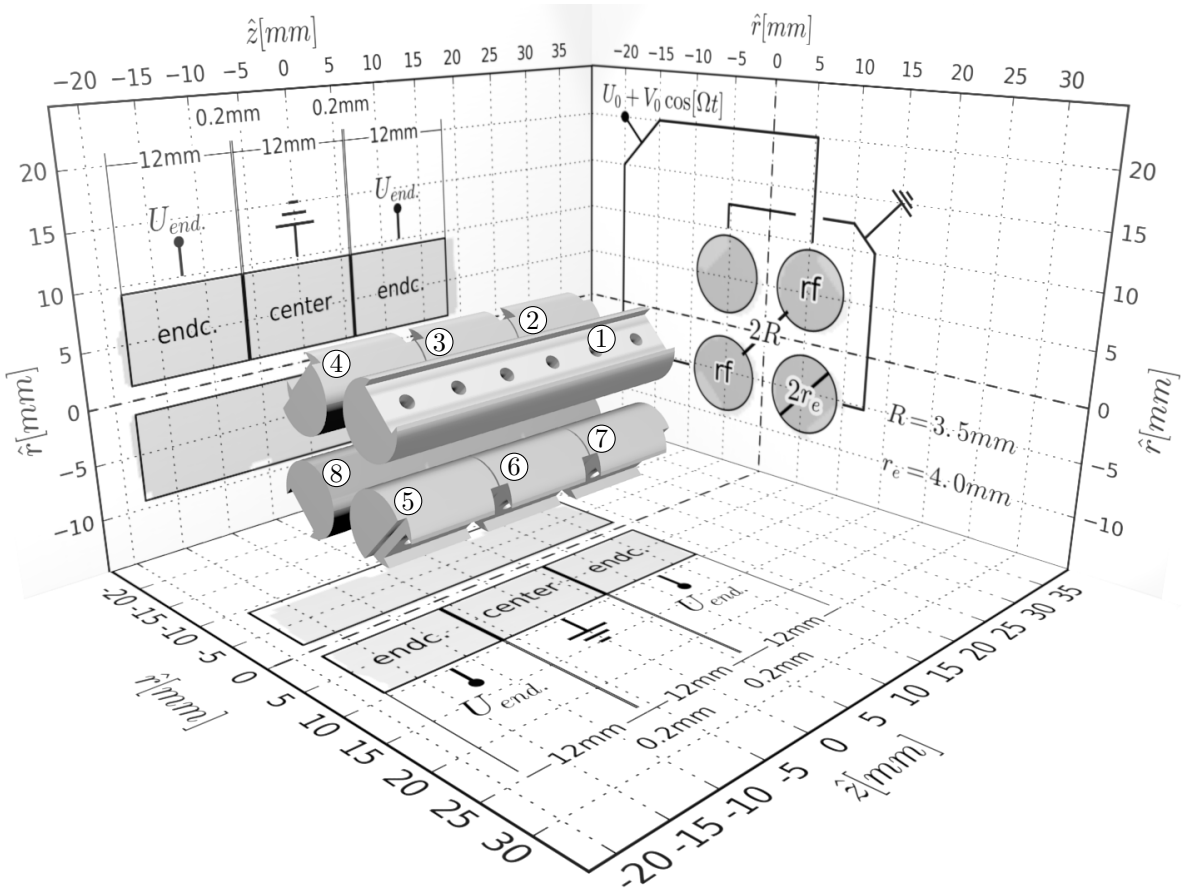

Figure 2.18: *Linear Paul trap with its eight electrodes and the corresponding electric connections.*

rf grounding

The six smaller electrodes with a length of 12 mm are each separately RF - grounded (using a 1 nF CMS capacitor) right at the trap housing, in order to minimize any picked up signals due to the RF supply. With a resistance of $R = 100\,\mathrm{k}\Omega$ the parameters of this part of the circuit in Fig. 2.19 (dashed box) are such that it acts as a low pass filter, allowing only frequencies below a cut off frequency of $\approx 1.6\,\mathrm{kHz}$ to pass. This is well below the RF frequency of the trap at 13.35 MHz, and also well below the secular frequencies, which are $> 44\,\mathrm{kHz}$ (see

also table 2.1).

current compensation

While creating Be^+ ions by electron impact (see section 2.4) the emission current of the e-gun is dissipated mostly by the trap electrodes. This leads to currents of $\approx 10\,\mu$A and together with the resistance of $100\,\text{k}\Omega$ for the RF - grounding this may change the voltages at the trap electrodes in an order of magnitude of 1 V and prevent trapping. As seen in the section before in Fig. 2.14, such additional voltages change the position of the potential minimum and therefore possibly increase the effect of rf-heating. In order to counteract for this effect the electrodes are connected to an electrical circuit which actively stabilizes the voltages at the trap electrodes. This circuit is shown in Fig. 2.19 and is described in [47].

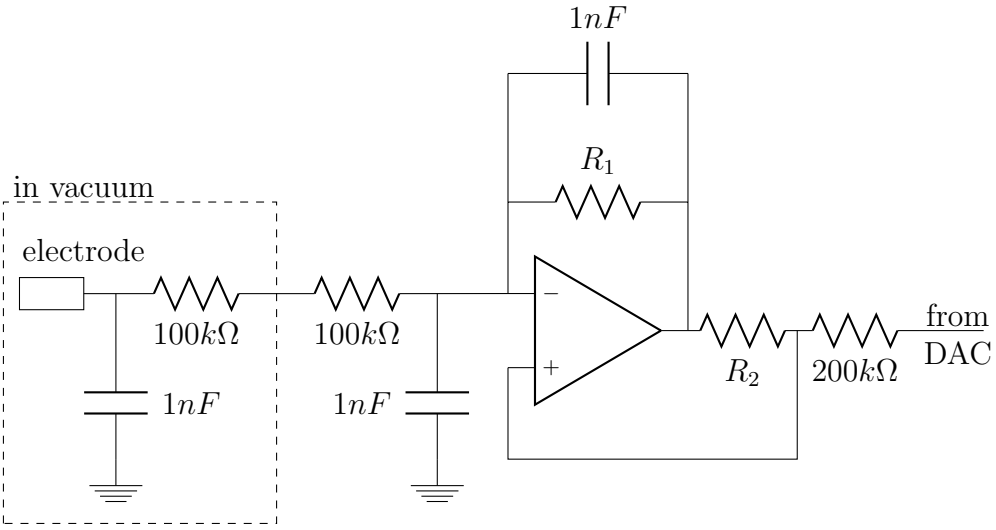

Figure 2.19: *DC electrode connection and voltage stabilization. In the case of the DC electrodes the values for the resistances R_1 and R_2 are $12\,\text{k}\Omega$, for the RF electrodes $R_1 = R_2 = 100\,\text{k}\Omega$.*

A DAC from National Instruments provides the voltages for the DC electrodes. The output voltages are between -10 V and $+10$ V. The DAC is interfaced with Python 3 and the DC voltages on the trap electrodes can be controlled individually from the experiment control software.

2.3.3 RF Voltage Supply

Red Pitaya

The sinusoidal RF voltage is provided by a Red Pitaya used as a signal generator, which is interfaced by the Python experiment control. The red pitaya output is sent to a RF001100-25 RF amplifier from RFPA, which delivers up to 25 W between 0.01 and 100 MHz. This results in an RF amplitude of ≈ 15 V on a $50\,\Omega$ impedance.

helical resonator

In order to provide the trap with a stable and high voltage potential a helical resonator [51] was designed, Fig. 2.20 shows a sketch of the

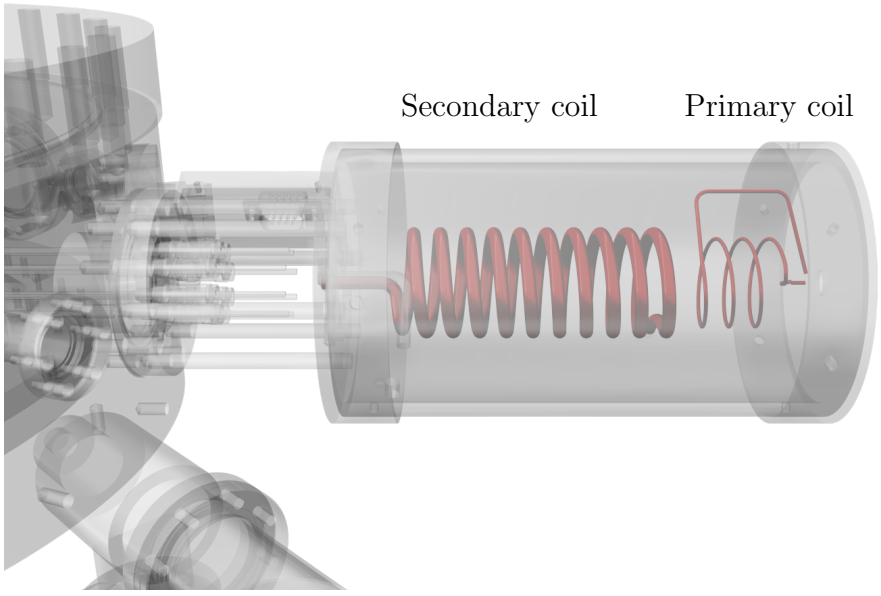

Figure 2.20: *A sketch of the helical resonator. The secondary coil is inductively coupled to the primary coil.*

design. The amplifier output is connected to the primary coil of the helical resonator, and the secondary coil is capacitively connected to the trap electrodes. The coil of the helical resonator consists of a 5 mm copper wire with 19 windings. The pitch of the coil is 10 mm and the diameter is 45 mm. The primary coil, or RF antenna, has 7 windings and is made of a copper wire with 1 mm diameter. The RF antenna is partially inserted into the secondary coil.

shifting the f_{res}

Since the original design of the experiment included RF guides for the injection of externally produced H_2^+ ions, the parameters of the helical resonator were optimized for a higher capacitative ballast than we ended up with (instead of the guides and the trap only the trap accounts for the capacitative ballast). Therefore the resonance frequency of the lumped system was lowered from 19.47 MHz to 13.37 MHz by adding an additional capacitance C_{add} (see Fig. 2.21) into the circuit.

trap capacitance

Measuring the resonance frequency f_{res} as a function of the added capacitance C_{add} gives access to the inductivity L_{coil} of the coil and the capacitance C_{trap} of the trap. For this measurement the circuit in Fig. 2.21 was used, but without the connections to the DC supply (shown in the dotted rectangles). Adding the two capacitors for the divider bridge in a combined capacitor C_{bridge} one can write for the total capacitance of the circuit (neglecting the low impedance of the big capacitors C)

$$C_{tot} = C_{\mathrm{bridge}} + C_{\mathrm{add}} + C_{\mathrm{trap}} + C_{\mathrm{coil}}. \tag{2.42}$$

Asuming the inductance of the trap is small one can write $L_{coil}\, C_{tot}\, \omega^2 = 1$ and therefore

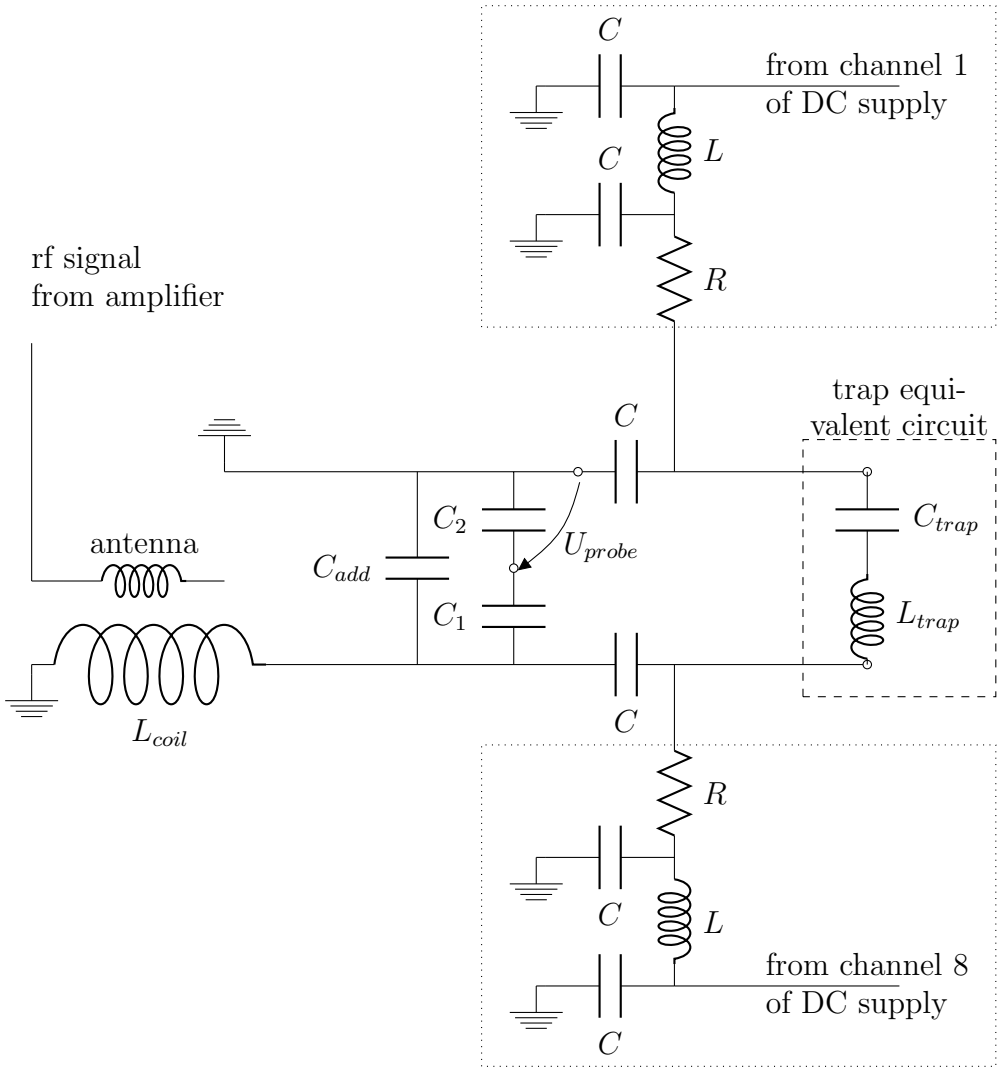

Figure 2.21: *The lumped system, consisting of the helical resonator and the trap. For the capacitors:* $C_1 = 1.8\,\mathrm{pF}$, $C_2 = 18\,\mathrm{pF}$ *and* $C = 10\,\mathrm{nF}$. *Remaining parameters:* $R = 220\,\mathrm{k\Omega}$ *and* $L = 0.1\,\mathrm{mH}$.

$$C_{\mathrm{bridge}} + C_{\mathrm{add}} = \frac{1}{L_{\mathrm{coil}}} \frac{1}{(2\pi f_{\mathrm{res}})^2} - (C_{\mathrm{trap}} + C_{\mathrm{coil}})\,. \tag{2.43}$$

Fig. 2.22 shows the measured values for the expression above and a linear fit. With this fit the inductance of the coil can be determined to $L_{coil} = 1.63\,\mu\mathrm{H}$ and the capacitance $C_{\mathrm{trap}} + C_{\mathrm{coil}} = 35.3\,\mathrm{pF}$. By removing the trap equivalent circuit (within the dashed rectangle in Fig. 2.21) and measuring a resonance frequency of 32.6 MHz one can also determine the capacitance of the coil. With $L_{\mathrm{coil}} \cdot C_{\mathrm{coil}} \cdot (2\pi \cdot 32.6\,\mathrm{MHz})^2 = 1$ the value for the capacitance C_{coil} results in 14.7 pF, and one finally obtains a value of $C_{\mathrm{trap}} = 20.6\,\mathrm{pF}$ for the capacitance of the trap.

By adding a capacitative ballast of 54 pF the resonance frequency

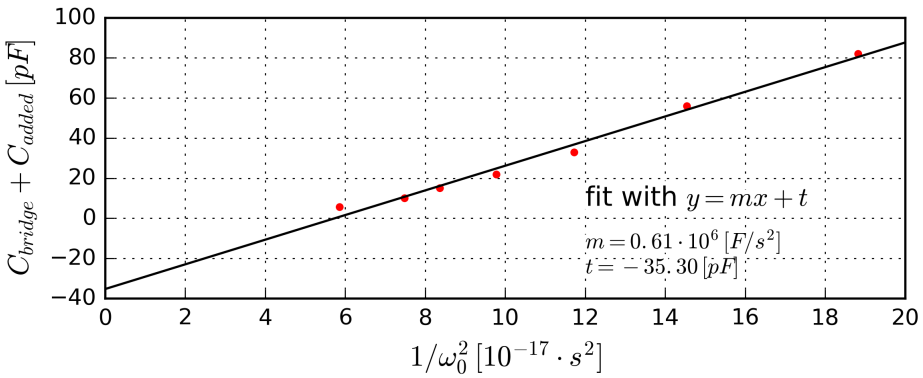

Figure 2.22: *The resonance frequency of the RF circuit versus the added capacitance.*

is finally shifted to a lower value. While the maximum amplitude of the RF voltage was 671 V at 19.47 MHz, this reduces to 518 V at 13.37 MHz (see also Fig. 2.23). The quality factor reduced as well, from 46.4 to 27.3 . However, since the a_i and q_i factor are $\propto 1/\Omega^2$ (see section 2.2.1) the values for the two factors increase and lead to more suitable values for light particles (see also Table 2.1).

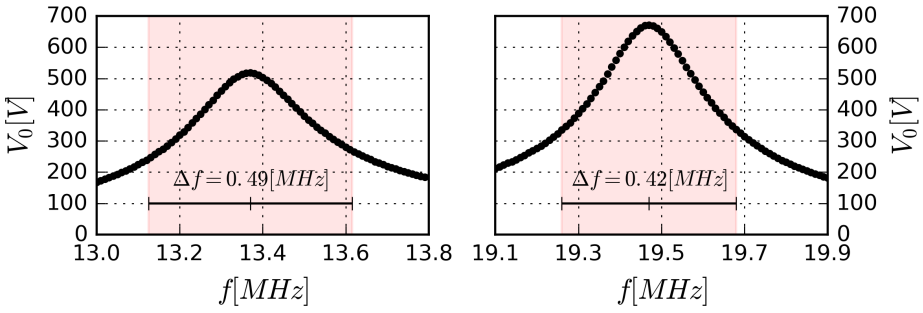

Figure 2.23: *Amplification of the helical resonator, with and without additional capacitance.*

2.4 Loading Ions

The RF potential makes it difficult to load ions from the outside. Therefore neutral atoms are targeted towards the trapping region and are there ionized, either by photo-ionization or by electron impact ionization, using an electron gun.

molecular beam

To load H_2^+ ions a gas inlet for a molecular beam was constructed and is together with the REMPI laser currently being tested within another experimental setup (see section 2.6 and [32]).

atoms and e-gun

The creation of the Be^+ ions can be solved by another approach. An oven is used to produce beryllium vapor close to the trap center. Then an electron gun ionizes the beryllium atoms. The design for the beryl-

lium oven (see further below) was developed by P. O. Schmidt and T. Rosenband at the National Institute of Standards and Technology, and is an improvement of the design described in [52]. In Fig. 2.24 a) the overall arrangement of trap, beryllium oven and electron gun is shown.

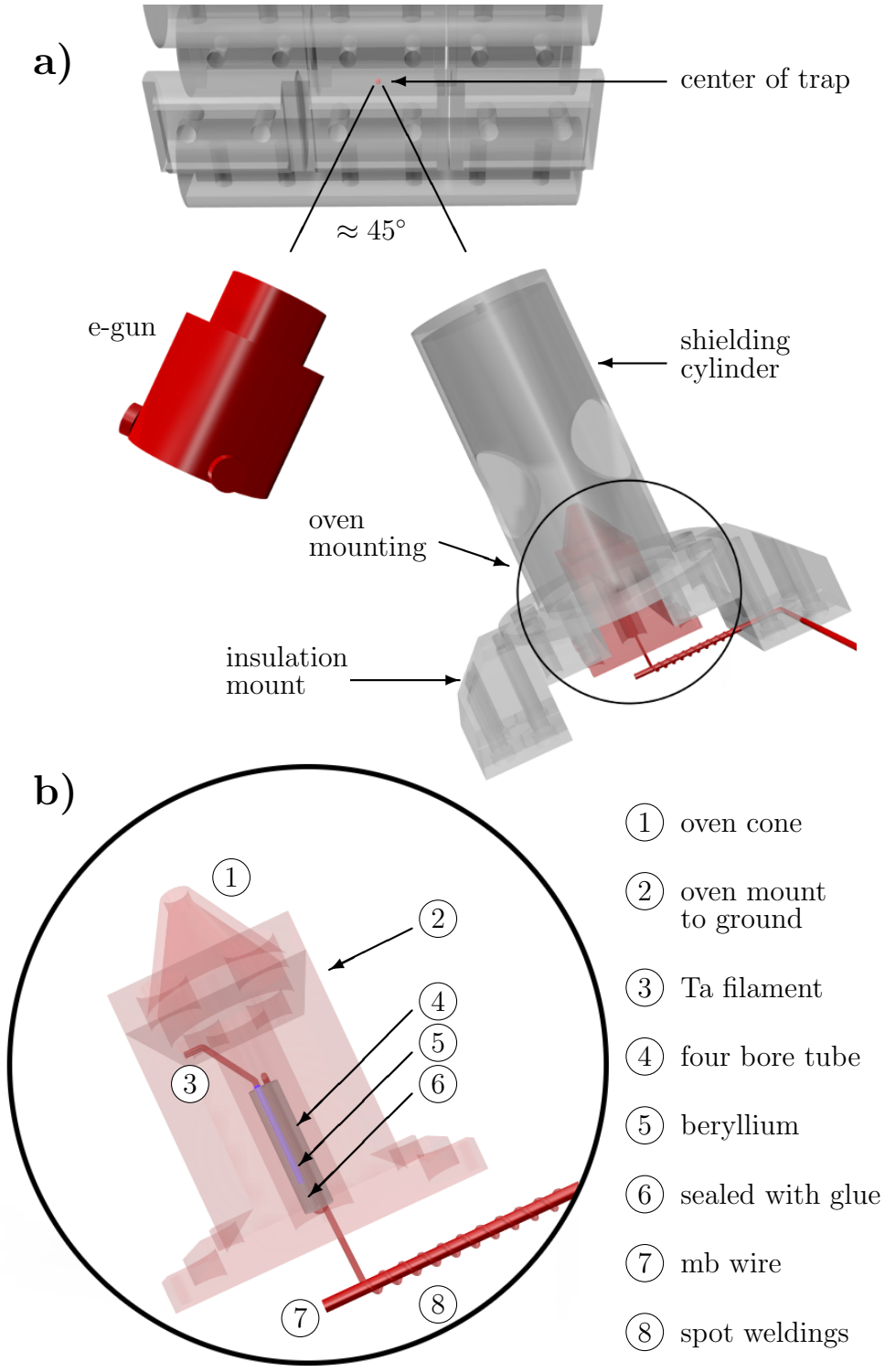

Figure 2.24: *Beryllium oven and electron gun.*

2.4.1 Beryllium Oven

The main component of the beryllium oven is an aluminium oxide (Al_2O_3) tube with a length of ≈ 5 mm and a diameter of ≈ 1.2 mm. Beryllium has a melting point of 1560 K and is brittle in its solid state. The melting point of Al_2O_3 is with 2345 K significantly higher than the one of beryllium.

design

The Al_2O_3 tube comprises four holes , each with a diameter of 0.254 mm (see Fig. 2.24 b)). A tantalum wire to heat, with a diameter of 0.125 mm is looped through three of the four holes. In the fourth hole a beryllium wire with a diameter of 0.25 mm and a length of ≈ 3 mm is placed. To fix the beryllium wire in its position and also to seal one of the openings, one end of the Al_2O_3 tube is filled with a ceramic paste (Ceramabond 569), which is, once it is hardened, temperature resistant up to 1923 K.

The tantalum wire is then spot welded to a molybdenum wire with a diameter of 0.5 mm, which is connected to the copper current supply by a wire to wire screw connector that is vacuum compatible.

The tantalum wire is wrapped around the molybdenum wire (see Fig. 2.24 b)), and thereafter the two wires are connected through multiple spot weldings. The spot welding is done with an old Sciaky spot welding machine. This machine has two parameters: The intensity of the current and the duration of the welding time, where both of the parameters are without units. A setting of 10 for the intensity and 5 for the duration leads to a robust connection. Different parameter settings lead either to a weak connection or to a damage of the tantalum wire.

heat reflector

To heat the oven and evaporate beryllium a current is sent through the tantalum wire. Since a significant amount of the heat is lost by radiation, the oven is placed within a stainless steel enclosure. This reduces the current needed, and helps to prevent the tantalum wire to break because of too high current.

In order to prevent sputtering the electrodes with beryllium the oven is covered with a stainless steel cone (bottom of Fig. 2.24) and an additional cylinder with a hole at the top is attached (see Fig. 2.24). These two apertures cause a collimated beryllium beam and help to aim the beam into the center of the trapping region, without sputtering to much Be^+ on the electrodes.

oven testing

To test the oven and determine the current which is needed to evaporate a sufficient amount of beryllium atoms, the oven was mounted in a vacuum cross. In front of the oven a residual gas analyser was mounted. The results can be seen in Fig. 2.25. Heating the tantalum wire with a current of > 2.95 A is sufficient to produce enough beryllium vapor for a loading of the trap using the electron gun. The oven current is provided by a three channel Keithley power supply, which is also used to drive the electron gun.

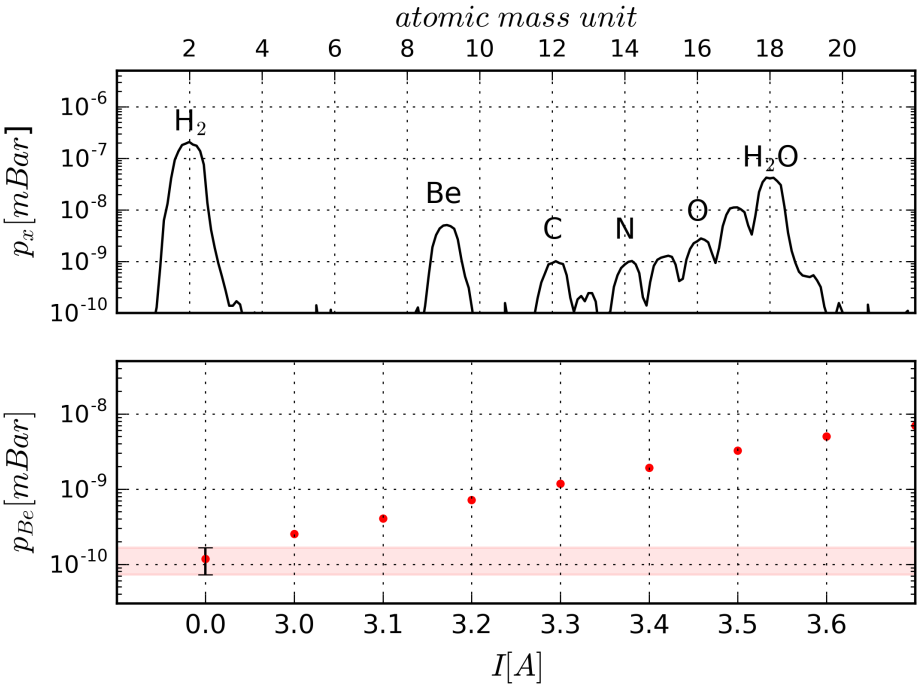

Figure 2.25: *Top: Partial pressure as a function of the atomic mass unit for an oven current of* 3.5 A. *Bottom: The partial pressure of beryllium as a function of the oven current. The bottom bar shows the noise at an oven current of* 0.0 A.

2.4.2 E-Gun

In this experiment the beryllium ionization is done by electron impact ionization (for photo ionization see for example [53]). Thus an electron gun (model FRA-2X1-2 from Kimball) is mounted close to the trap center (see Fig. 2.24). The angle between the neutral beryllium atoms and the electrons is approximately 45°. The beam energy can be adjusted in between 5 and 1000 eV. The beam current is adjustable in between 5 nA and 400 μA. The spot size of the beam varies with the beam parameters, but the design is optimized for a 20 mm diameter for 50 eV and a working distance of 25 mm.
During the loading of beryllium ions the electron gun is operated for the complete loading time. The emission current is approximately 20 μA, and the beam energy 120 eV. The supply of the e-gun is done with the same Keithley power supply the oven current is provided.

2.5 The Vacuum System

Since the objective of the experiment is the investigation of light molecules, the experiment needs to be placed in an ultra high vaccum

(UHV) environment. The UHV regime is characterized by pressures below 10^{-9} mbar. In Fig. 2.26 a schematic view of the vacuum system can be seen. The main components are the experiment chamber (electropolished, custom made titanium chamber, with an inner diameter of 298.5 mm), a turbo pump and a turbo pumping station (including a turbo pump and a baking pump), an ion pump and a titanium sublimation pump. The setup is designed to reach pressures well below the start of the UHV regime, 10^{-10} - 10^{-11} mbar.

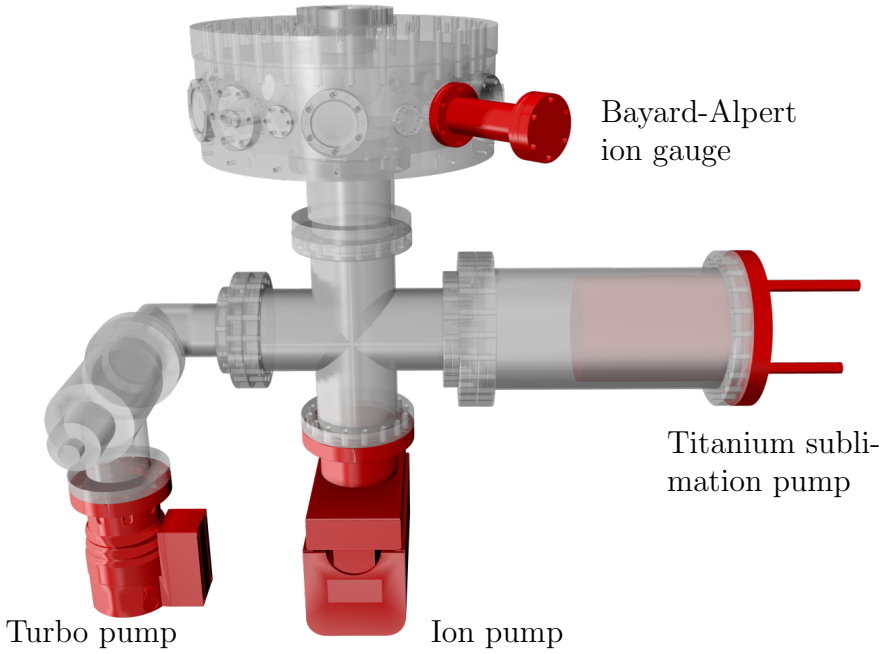

Figure 2.26: *Sketch of the vacuum housing. The turbo pumping station is placed after the first turbo and not shown in the sketch.*

baking To reach low pressures the complete setup was heated around 100 °C, using heating wires. The limiting factor for the temperature are the ZnSe windows for the IR laser. Baking removes water and other gases which were adsorbed at the chamber walls during cleaning and during the contact with air. In Fig. 2.27 a typical baking cycle is shown. After closing the setup the turbo pumps are started and the temperature is increased, such that the temperature gradient does not exceed the tolerances of the windows ($\approx$ 10 °C/min). After baking the setup the ion pump is started and the heating turned off. Without using the titanium sublimation pump a pressure of $\approx 2.5 \cdot 10^{-10}$ mbar was reached within a week.

testing To test the vacuum setup and detect possible leaks one can determine the outgassing rate. For that reason all pumps were stopped and the pressure was measured using the Bayard-Alpert gauge each 15 s for 240[s]. A linear fit shows an increase of $1.27 \cdot 10^{-9}$ mb l/s.

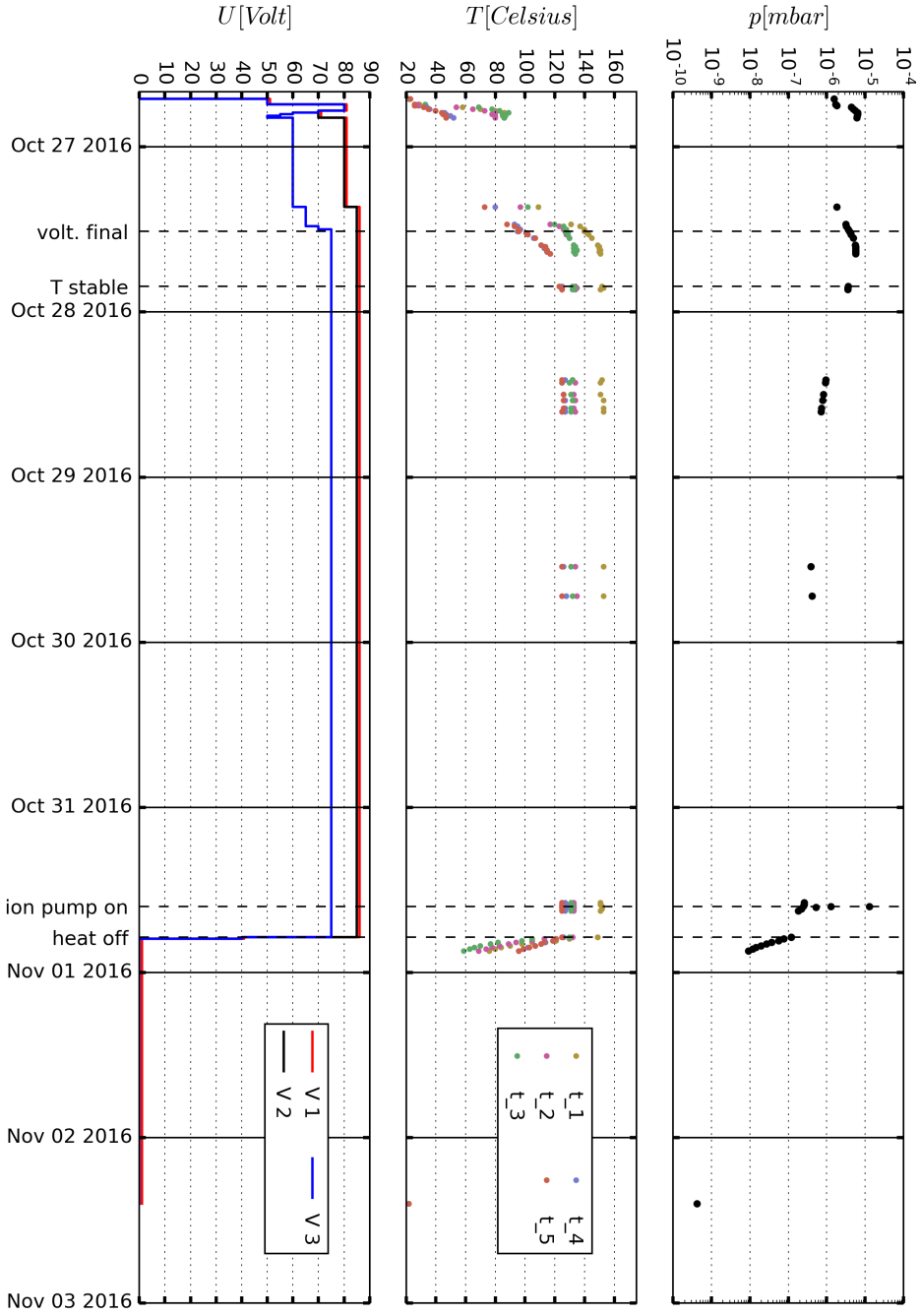

Figure 2.27: *After baking the setup for five days and pumping, the pressure decreases to* $\approx 2.5 \cdot 10^{-10}$ mbar. *During this process the voltage applied at the heating wires, the temperature and the pressure was monitored.*

By estimating the enclosed volume and the surface of the setup to 18.6 l and 8100 cm^2 one can find a value for the outgassing rate. After applying a correction factor for molecular hydrogen of 0.46 [54] for the pressure indicated by the Bayard-Alpert gauge finally an outgassing rate of $3.40 \cdot 10^{-13}$ mb l/s/cm^2 is found. An overview of outgassing rates for different materials and treatments can be found here [55].

The lowest value for stainless steel is $2.13 \cdot 10^{-14}$ mb l/s/cm^2, after a baking at 1000 ° for 3 hours and subsequently baking at 360 ° for 25 hours. This indicates that the setup presented here is working well. Only recently (January 2018) the titanium sublimation pump came into operation. The pressure indicated by the Bayard-Alpert gauge dropped to approximately $6.7 \cdot 10^{-11}$ mbar, which is close to the limit of the pressure range these gauges can accurately detect.

2.6 The H_2^+ Source

The design for the in situ creation of the H_2^+ ions in form of a molecular beam with a differential pressure setup and a 303 nm laser source is described in detail in [32]. Fig. 2.28 shows a preliminary plan for the molecular beam source. At the moment the apparatus is mounted at a different setup and tested there.

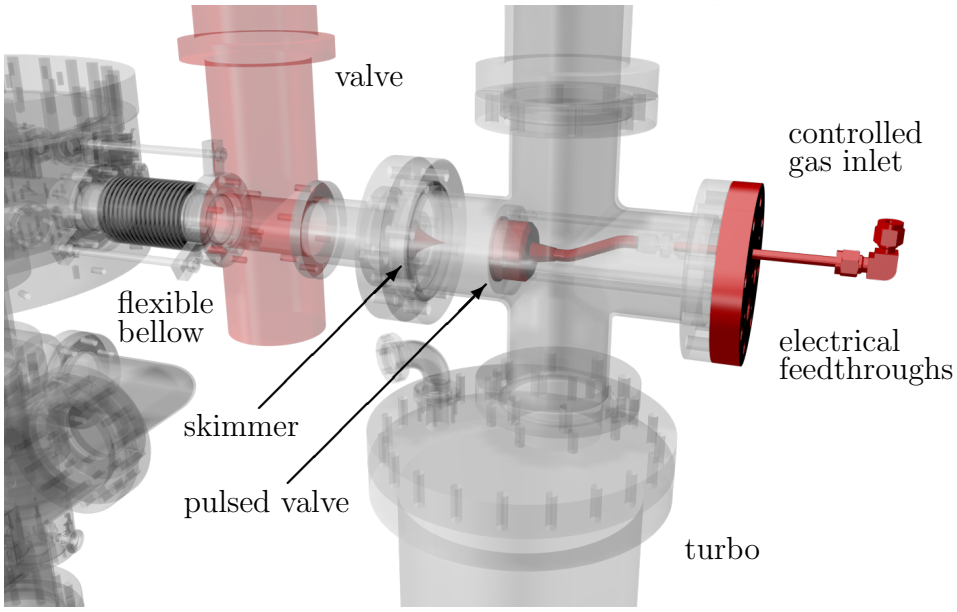

Figure 2.28: *A sketch of a first design for the molecular beam of* H_2.

pulsed valve Its main components are a piezo-electric pulsed valve and a skimmer, which, together with a controlled gas inlet, divide the volume in three parts with different pressure. In the first part, before the pulsed valve, the H_2 gas is stored at a couple of 100 mbar. This pulsed valve can be opened and closed with high frequencies, while the delay in between the openings can be controlled.

skimmer In this region after the valve and before the skimmer a turbo pump ensures a good intermediate pressure, before the skimmer marks the transition into the last regime, the main chamber, where a pressure of $\approx 10^{-10}$ mbar should be maintained. The skimmer works also a kind of collimation for the molecular beam, since due to its shape only molecules with a certain velocity vector can pass. A flexible bellow

allows for the alignment of the complete ion source with the center of the trap, where the photodissociation will take place.
At the moment the design will be changed to include two skimmers, to obtain a better differential pressure setup. While the $3+1$ REMPI scheme has been shown to work [32], a $2+1$ REMPI scheme is under investigation.

status

2.7 Imaging

The detection of the fluorescence of the Doppler cooled beryllium ions with CCD cameras allows for an analysis of the trapped ions, like for example the number of ions. If the ions form a Coulomb Crystal (see section 4.1) also the shape of the crystal can be detected. This allows for the identification of different species of commonly trapped ions. A photomultiplier allows for the minimization of micromotion (see section 4.3). An overview of the implemented imaging system can be seen in Fig. 2.29 below.

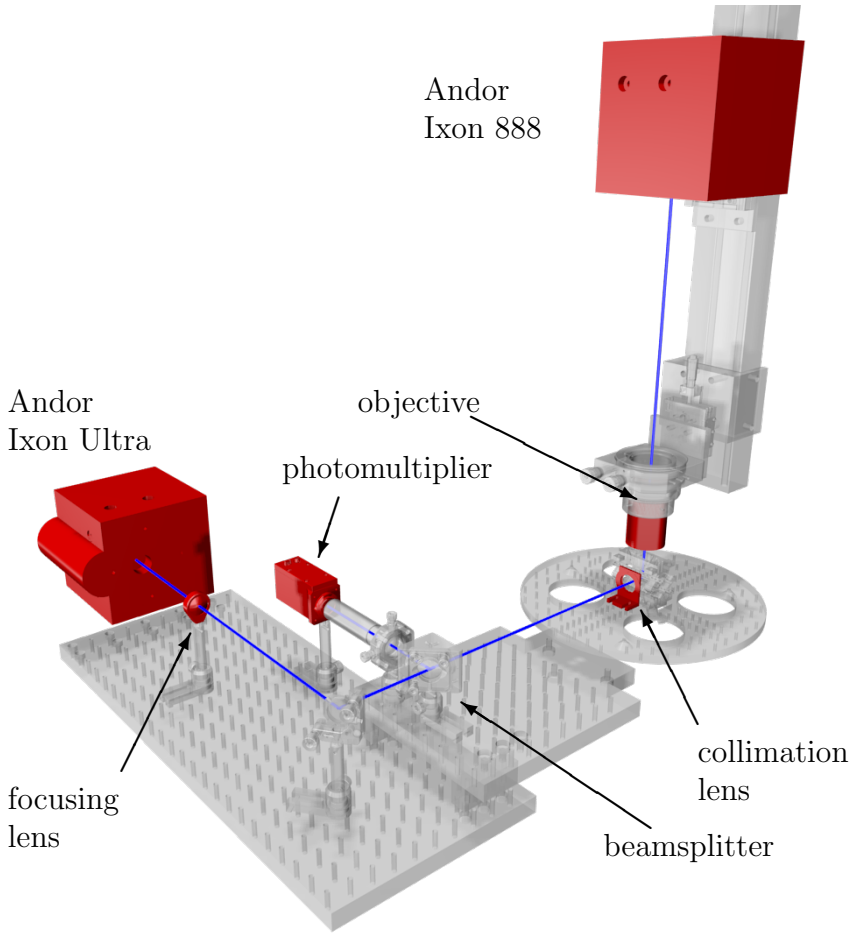

Figure 2.29: *Sketch of the imaging system and the photomultiplier.*

Two EMCCD (electron multiplying charge-coupled device) cameras were mounted to monitor the experiment. The camera on top is an

EMCCD cameras

Andor Ixon 888 with 1024×1024 pixel, with an edge length of $13\,\mu$m. The camera responsible for the imaging in the horizontal plane is an Andor Ixon Ultra, which comes with 512×512 pixel, each having an edge length of $16\,\mu$m. Both cameras have a built-in peltier element to cool the chip, which decreases the dark current and improves the signal. Without additional help (except the also built-in fans) to transport the excess heat the minimum operating temperature is approximately $-80\,°$. The quantum efficiency for CCDs is at 313 nm very low, for which reason in both cameras the CCD chip is coated with a material which absorbs the UV-photons and emits at a different wavelength. This increases the quantum efficiency to $\approx 30\%$.

collected photons IXON Ultra

In order to estimate the collected photons one needs to analyze the optical accessibility of the trap center. Fig. 2.30 sketches the geometric situation for the camera in the horizontal plane.

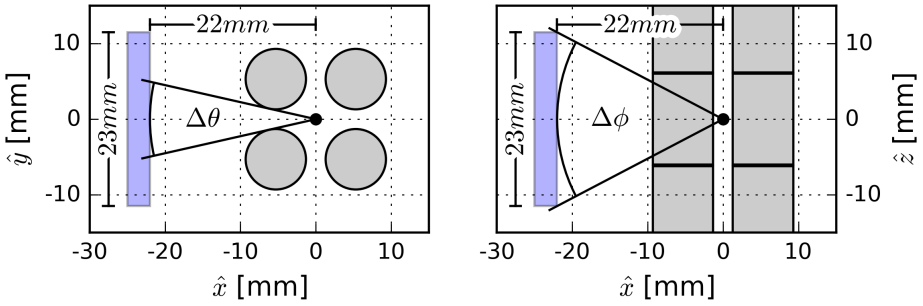

Figure 2.30: *Sketch of the position of the lens (indicated on the left side) relatively to the trap. The electrode diameter limits the angle θ.*

The fluorescence of the trapped and cooled ions is collected with a 1 inch collimation lens (see also Fig. 2.29), which is mounted in a home-build holder, resulting in an effective diameter of 23 mm. The front surface of the lens is 22 mm away from the trap center. Although the large lens would allow to collect about 5.7% of the fluorescence light the clipping by the electrodes reduces this value. An estimation of the solid angle can be done in spherical coordinates, by integrating over $\Delta\theta = 25.5\,°$ and $\Delta\phi = 55.2\,°$, which results in 3.4% for the percentage of the collected light. Since this does not take the circular cross section of the lens into account the actual value is even smaller.

collected photons IXON 888

The objective for the top camera is placed outside the vacuum, which results in a larger distance between objective and the trap center. The percentage of collected light is therefore smaller than the overestimated value for the camera in the horizontal plane. Additionally, one needs to take the bandpass filters (model FGUV11 from Thorlabs, 80 % transmission at 313 nm) into account. These filters are mounted on the cameras to reduce the detection of stray light. In summary one ends up with less than 1% of detected light at each of the cameras. For the camera in the horizontal plane this value decreases further, since only a part of the resulting fluorescence signal is used for the camera.

photomultiplier

The other part of the signal is guided to a commercial photomultiplier from Hamamatsu (model H12386-210). The signal is then fed to a Time-to-Digital-Converter (TDC), which is able to measure the arrival time of the photomultiplier signal with precision in the ns range. By triggering the TDC with the RF frequency of the trap one can therefore measure the time of arrival of individual photons within a time interval defined by the RF frequency. This can be used to minimize the micromotion of the trapped ions (see section 4.3).

2.8 Experiment Control via Python 3

The coordinated interaction of the various experimental devices is a crucial part of any precision experiment. Therefore it is indispensable to control the complete setup with all its components from one control instance. In order to do that a highly scalable and modular control software has been developed.

choice of software

The right choice for the programming language for software development can make things easier. Python 3 is a modern programming language which is easy to handle and serves a wide range of applications, for instance:

- data analysis: the analysis of the SIMION potential arrays in the present manuscript is done with Python 3, using the *numpy* package
- plotting: all the figures in this manuscript are done in Python 3 and Blender, a Python based render engine
- hardware: the various measurement and control devices used in the experiment presented here are represented in a basic hardware abstraction layer implemented in Python 3, partly using the *ctypes* package to interface with c and c++ libraries
- graphical user interfaces (GUI): the front end implemented to control the experiment presented here is written in Python 3

Since the software had to be written from scratch there was freedom of choice for the programming language, and Python 3 is an appropriate trade-off between simplicity and capability. When designing the overall structure of such a software one should always try to keep the software architecture as clear as possible, while maintaining modularity in order to provide scalability and extensibility regarding hardware devices and measurement work-flow.

object oriented

The software developed for this experiment is based on the object-oriented character of Python 3. The general scheme can be seen in Fig. 2.31. Each included device is represented by a separate class. This has the advantage that the functionality of each device can be tested individually. The methods for communication between the computer

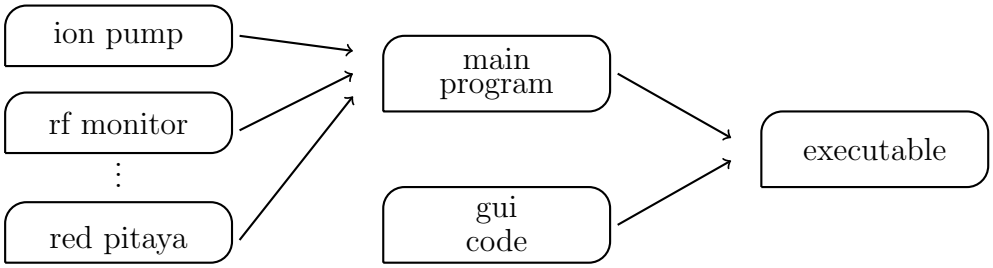

Figure 2.31: *The hierarchy of the code for the experiment control.*

and the device in question are all collected in that class.

communication protocols

Note, that different devices may use different communication protocols. The devices interfaced during this PhD project are mainly controlled via the *VISA* package of python, which bundles severall communication protocols. Exceptions are the digital to analog converter, the Red Pitaya, the cameras and the wavemeter. The last two are controlled by dynamic link libraries (DLL) which are written in C++, and can be accessed using the *ctypes* package of Python 3. In Tab. 2.4 the devices interfaced during this PhD project are listed, together with the used communication protocol.

device	purpose	communication via
AgilentTech DSO1024A	RF frequency monitoring	VISA
Andor Cameras	imaging	ATMCD32D.DLL
HighFinesse WS07	frequency monitoring and locking	wlmData.dll
Keithley 2231A 30 3	Be oven and e-gun current	VISA
NI PCI6703 DAC	DC voltages output	PyDAQmx
NI PCI6010 ADC	DC voltages input	PyDAQmx
Red Pitaya	RF frequency	SCPI access
SPC ion pump	pressure	VISA
Thorlabs piezo controller	wavelength of the fiber laser	VISA

Table 2.4: *The various interfaced devices , their purpose and the communication protocol used. The cameras and the wavemeter are interfaced via dynamic link libraries (DLL).*

software architecture

Once the interaction with the device is tested, an instance (also called object) of the class is created in the main program. The main program bundles instances for each device. Within the main program new methods can be implemented, which for example access different devices simultaneously. Many needed methods expand over a certain time interval, for example ramping of voltages or the detuning of a laser. Since it is crucial to perform tasks simultaneously, it is important to use concurrency. The developed software uses the Python 3 package *threading* for that. Another vital part is to make the configuration of a certain experiment persistent by using configuration-files. This way the configuration of a measurement can be saved and reloaded to repeat. In the present version of the software this is done

by simple *.txt* files, which are automatically provided with a timestamp within the name of the configuration-file. In that way the recorded data can be linked to the corresponding configuration-file, in order to have the experimental parameters available when interpreting the data.

GUI

In principle the experiment can now be controlled by calling an instance of the main program, but it is not very pleasant to operate an experiment within a terminal. Therefore a GUI must be implemented. Here severall options are available, like for example the *TkInter* package for Python. The usage of *TkInter* is a tedious work, since the layout, positions of buttons, and other details must be implemented by writing the code by hand. In addition one often ends up with a code where the main program and the instructions for the GUI are not clearly separated. A better solution is to use *Qt-Designer*. This is a so called what-you-see-is-what-you-get tool, which allows to compose a GUI quickly and easily. The drawback is that *Qt-Designer* is intended for C++, but the code for the GUI can be automatically translated to the corresponding Python bindings of Qt by using the Python module *pyuic5*.

final step

As a final step an executable has to be implemented, which connects the methods of the main program with the GUI. Following this approach one ends up with a software which clearly separates the interfacing of the various devices from the tasks one wishes to execute and the GUI. This makes the code easy to modify or extend, while maintaining it readable, which is important if more than one person is supposed to perform changes.

GitHub

The complete code for the experiment control can be found on GitHub via XCon_02, and the next release, XCon_03, will be available in the near future.

Chapter 3

Cooling Trapped Ions

$\approx 5\,500\,000\,000\,000$ K	Large Hadron Collider at CERN
$\approx 100\,000\,000\,000$ K	Supernovae
5 000 - 15 000 000 K	The Sun
95 - 397 K	The Moon
≈ 2.7 K	Outer Space
≈ 0.01 K	Coulomb Crystals
0.0000001 K	Bose-Einstein Condensates

Temperatures of different objects.

As motivated in the introduction in section 1.2, cooling of the trapped H_2^+ ions is indispensable. Since the H_2^+ ions cannot directly be laser-cooled sympathetic cooling via Be^+ ions is applied. The Be^+ cooling transition used in this experiment requires a laser at 313 nm with a linewidth of 2 MHz or less and a few mW of optical power.
Over the last decades ion trapping and cooling became a very active field of research, so that nowadays multiple technological solutions exist to provide suitable light at 313 nm. Many of them include the production of light at 626 nm and the subsequent frequency doubling in a bow-tie cavity.

This chapter is structured as follows: In the first section Doppler-cooling is reviewed. This allows to evaluate what requirements the laser source should meet.
During this PhD project different approaches were followed to provide light at 626 nm, and the results are presented in the second section. The frequency doubling to 313 nm is achieved in a bow-tie cavity, which is also presented in section two.
The last section gives an overview over the remaining three laser sources which are needed to probe the $\nu = 0, L = 2 \rightarrow \nu = 1, L = 2$ two-photon transition in H_2^+.

3.1 Doppler Cooling

In order to perform precision spectroscopy on free particles the Doppler broadening of the transitions needs to be reduced. This broadening depends on the random thermal velocities of the particles. The particle speed probability distribution is the Maxwell-Boltzmann distribution, and depends on the mass of the particles and the temperature of the gas. At the top left of Fig. 3.1 the Maxwell-Boltzmann distribution is shown for Be at different temperatures. With a mass of $m_{Be} = 9\,\text{amu}$ beryllium is a light particle, and even at room temperature highly mobile.

initial Be^+ temperature

The trap depth of a linear Paul trap is in the range of a few eV. Together with the fact that the beryllium atoms are provided by an atomic oven one can therefore expect to find trapped Be^+ ions at temperatures of up to a few thousand Kelvin.

radiative forces

Laser cooling allows the reduction of the random thermal velocities by using radiative forces. First experiments to quantitatively investigate radiative forces of light on macroscopic objects go back to the beginning of the last century [56]. The idea to use optical pumping between atomic levels to cool was first proposed by A. Kastler in 1950 [57]. With the rise of narrow linewidth lasers D. Wineland et al. demonstrated in 1978 the first laser cooling of trapped ions [58].

Doppler effect

Tunable laser sources allow to cool trapped particles over a wide temperature range. Doppler cooling takes advantage of the Doppler effect, which states that the frequency seen by a moving particle is shifted depending on its velocity,

$$f = f_0 \left(1 - \frac{\mathbf{k}}{k}\frac{\mathbf{v}}{c}\right), \tag{3.1}$$

where $\mathbf{k}$ is the wavevector of the incident light and $\mathbf{v}$ the velocity of the particle.

Doppler broadening

Together with the Maxwell-Boltzmann distribution for the velocities of the trapped particles this leads to an expression for the Doppler-broadening of the spectral lines of atomic transitions,

$$p(f) = \frac{1}{\sqrt{2\pi}\,\sigma_f}\,\exp\left[-\frac{(f_0 - f)^2}{2\sigma_f}\right] \text{ with } \sigma_f = \sqrt{\frac{k_B T}{mc^2}}\,f_0. \tag{3.2}$$

At the top right of Fig. 3.1 the relative Doppler-broadening is plotted as a function of the temperature for transitions in beryllium and the hydrogen molecule. At room temperature the relative broadening $\Delta f/f$ for transitions in beryllium is $4.7 \cdot 10^{-6}$.

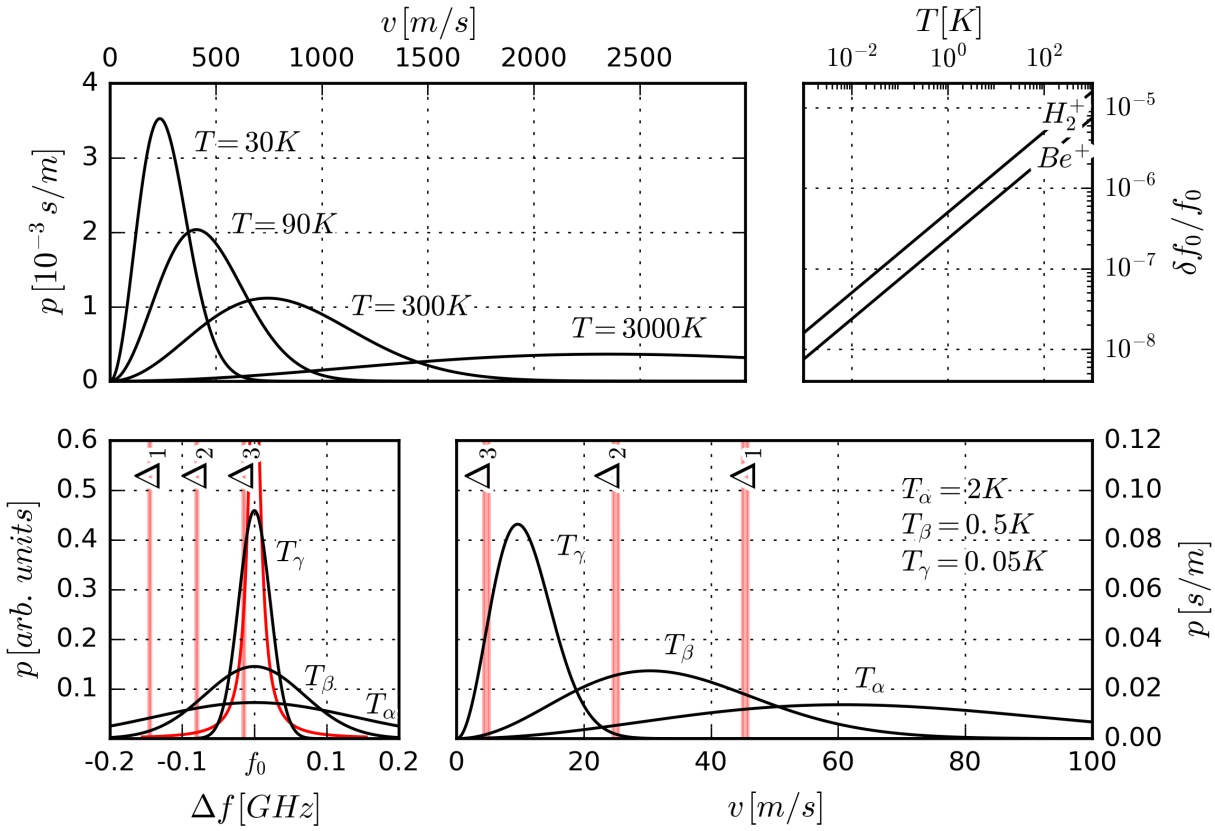

Figure 3.1: *Top left: The Maxwell-Boltzmann distribution for* Be^+ *ions at different temperatures. Top right: The relative Doppler-broadening as a function of the temperature. Bottom left: The Doppler-broadened transition line for* $^2S_{1/2} \leftrightarrow {}^2P_{3/2}$ *in* Be^+ *at different temperatures and a red-detuned laser at different detunings. Bottom right: The Maxwell-Boltzmann distribution for* Be^+ *at different temperatures. Depending on the detuning a narrow-linewidth laser addresses different velocity classes.*

example transition

The $^2S_{1/2} \leftrightarrow {}^2P_{3/2}$ transition in beryllium has a frequency of 957 396 616.6 MHz and a natural linewidth of 19.4 MHz [59], and is a commonly used transition for Doppler cooling. At the bottom left of Fig. 3.1 the Doppler-broadening for this transition is shown at different temperatures $T_\alpha = 2\,\mathrm{K}$, $T_\beta = 0.5\,\mathrm{K}$ and $T_\gamma = 0.05\,\mathrm{K}$.

tunable laser and velocity classes

In order to cool an atomic vapor efficiently, a tunable, narrow-linewidth laser is required. This can be understood by taking a look at the bottom right panel in Fig. 3.1, where the Maxwell-Boltzmann distribution is shown for T_α, T_β and T_γ. The initial temperature of the vapor is assumed to be $T_\alpha = 2\,\mathrm{K}$, and a laser with a linewidth of $\approx 2\,\mathrm{MHz}$ and a detuning of $\Delta_1 = 145\,\mathrm{MHz}$ acts on the particles with a speed of $\approx 45\,{}^m/_\mathrm{s}$. This causes a depletion of the velocity class around $\approx 45\,{}^m/_\mathrm{s}$. Note, that in the case of trapped ions, the Coulomb interaction results in cooling of all the faster particles as well. After thermalization most of the particles are in velocity classes slower than $\approx 45\,{}^m/_\mathrm{s}$ cooling is

not efficient anymore. By successively changing the detuning of the laser from $\Delta_1 = 145\,\mathrm{MHz}$ to $\Delta_3 = 15\,\mathrm{MHz}$, slower and slower velocity classes in the distribution are addressed, leading to smaller and smaller temperatures.

For a quantitative understanding of Doppler cooling a simple model is investigated. A thorough investigation of atomic motion in laser light can be found for example in the Les Houches lectures of C. Cohen-Tannoudji [60].

laser The incident laser is modeled as a monochromatic plane wave, characterized by its frequency ω_L, its wavevector $\boldsymbol{k}_L$, and the amplitude E,

$$\boldsymbol{E}_L(\boldsymbol{r}, t) = E \cos\left[\omega_L t + \boldsymbol{k}_L \boldsymbol{r}\right]. \tag{3.3}$$

atom The atom is modeled as a two level system, with a dipole transition frequency ω_A and natural linewidth Γ.
In Fig. 3.2 the interaction between the laser light and the atom is illustrated.

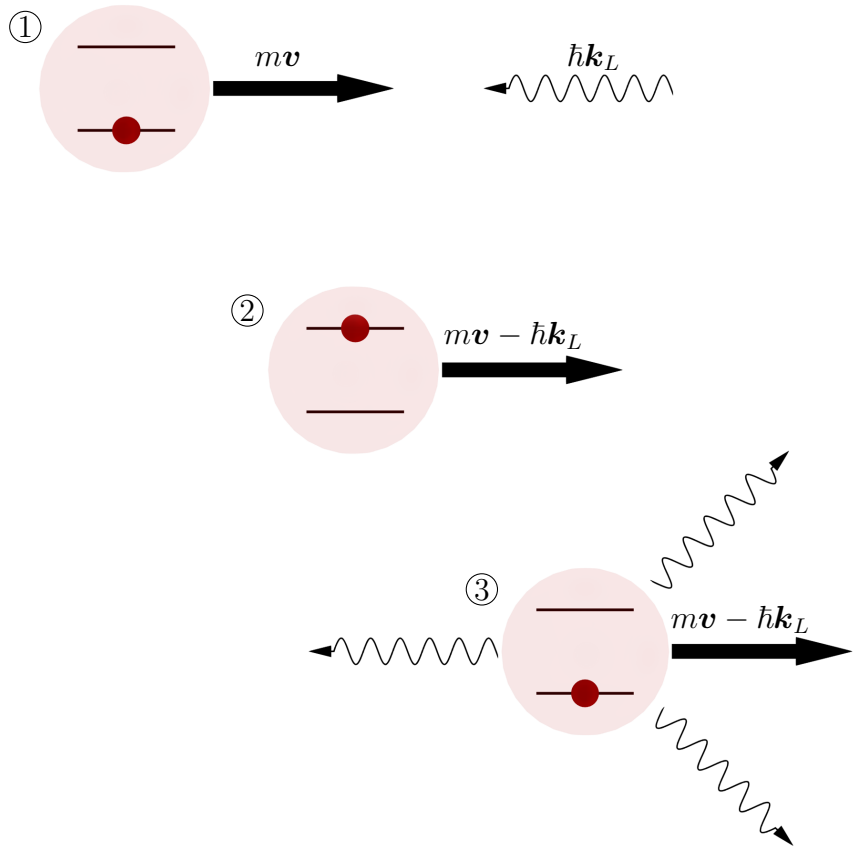

Figure 3.2: *A sketch to illustrate Doppler cooling.*

Part ① depicts the atom moving in the $\hat{z}$ direction with a velocity $\boldsymbol{v}$, and the incident laser beam with a wavevector $\boldsymbol{k}_L$ being antiparallel

to the velocity of the atom. ②: The absorption of a photon results in the reduction of the atomic velocity. ③: The direction for the emitted photon is randomly distributed. The repeated absorption and emission slows the atom down.

friction force

The friction force acting on an atom with velocity $\boldsymbol{v}$ due to a detuned laser beam can be written as [60]:

$$\boldsymbol{F}(\boldsymbol{v}) = \hbar \boldsymbol{k}_L \Gamma_{sc} = \hbar \boldsymbol{k}_L \frac{\Gamma}{2} \frac{\Omega_R^2/2}{(\Delta\omega - \boldsymbol{k}_L \cdot \boldsymbol{v})^2 + \Gamma^2/4 + \Omega_R^2/2}, \tag{3.4}$$

where Ω_R is the Rabi frequency, $\Delta\omega = \omega_L - \omega_A$ the detuning of the laser and $-\boldsymbol{k}_L \cdot \boldsymbol{v}$ the Doppler shift. Additionally the scattering rate Γ_{sc} was introduced, which will be useful later. The Rabi frequency can be expressed as [61]

$$\Omega_R^2 = \Gamma^2 \frac{I}{2\, I_{sat}}, \tag{3.5}$$

with the intensity $I = 1/2 \cdot c\epsilon_0 \left|E\right|^2$ and the saturation intensity $I_{sat} = \frac{\hbar\Gamma\omega_A^3}{12\pi c^2}$. Since we assume the atom moving in the $\hat{z}$ direction and the propagation of the laser beam being orientated in the opposite direction one can write $-\boldsymbol{k}_L\boldsymbol{v} = k_L v$. In the following we consider this one-dimensional situation. The top of Fig. 3.3 shows the friction force as a function of the Doppler shift $k_L v$ for different detunings $\Delta\omega$. Note, that the force is negative, since it is opposed to the direction of the velocity of the atom. A value of $k_L v = 1\Gamma$ can be assigned to a velocity of $\approx 6\,{}^{m}/_{\mathrm{s}}$ of the beryllium ions. For a detuning of $\Delta\omega = \Gamma$ the extremum of the friction force F_z acts therefore on the velocity class with $\approx 6\,{}^{m}/_{\mathrm{s}}$, exerting a friction force of $\approx -8.6 \cdot 10^{-20}\,\mathrm{N}$. Depending on the detuning different velocity classes are addressed.

friction coefficient

To gain more insight into the dynamics of the friction force one can expand the expression in eq. (3.4) around $v = 0$, leading to

$$F_z(v) = F_z(v=0) - \alpha v + \mathcal{O}\left(v^2\right), \tag{3.6}$$

with the so called friction coefficient

$$\alpha = -\hbar k_L^2 \frac{s}{(s+1)^2} \frac{\Delta\omega\Gamma}{\Delta\omega^2 + \Gamma^2/4}. \tag{3.7}$$

The parameter $s = \frac{\Omega_R^2/2}{\Delta\omega^2 + \Gamma^2/4}$ is called the saturation parameter. At the bottom of Fig. 3.3 the friction coefficient is plotted for three different intensities $I_A = 2I_{sat}$, $I_B = I_{sat}$ and $I_C = 1/2\, I_{sat}$.

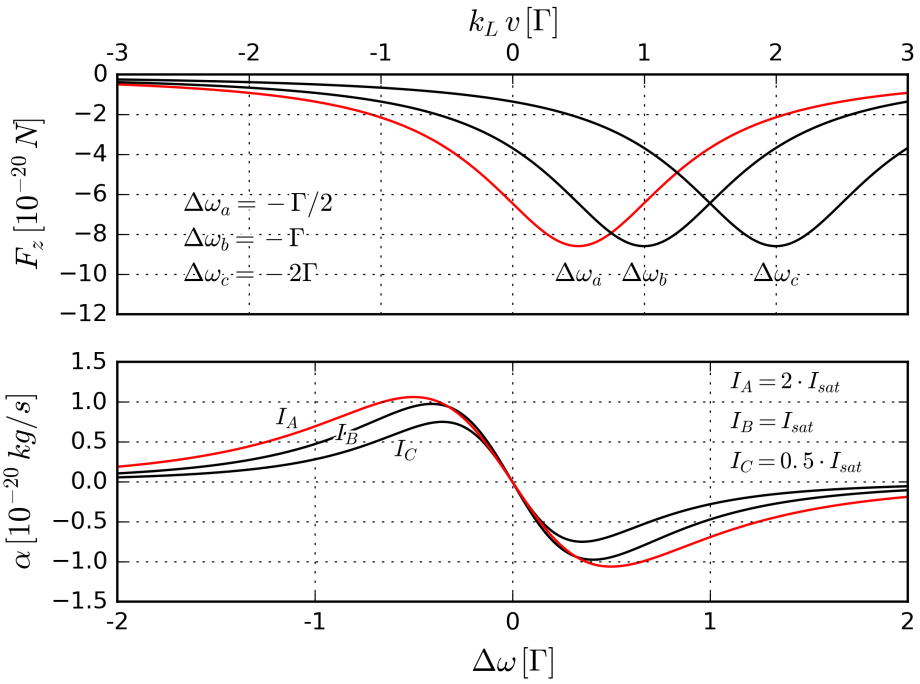

Figure 3.3: *Top: The friction force F_z for different detunings as a function of the Doppler shift. Bottom: The friction coefficent α for different intensities as a function of the detuning. For more see text.*

One can see that the position of the extrema in α depend on the intensity, and one finds

$$\Delta\omega_{1/2}\,(I) = \pm\frac{\Gamma}{2\sqrt{3}}\sqrt{1 + {}^{I}/_{I_{sat}}}, \tag{3.8}$$

which, for $I_A = 2I_{sat}$, simplifies to $\Delta\omega_{1/2}\,(I_A) = \pm{}^{\Gamma}/_{2}$. The corresponding maximum value for the friction coefficient is then $\alpha_{max}\,(I_A) = {}^{1}/_{4}\,\hbar k_L^2$.

damping rate

Using the equation of motion $m_{Be}\dot{v} = -\alpha_{max}(I_A)v$ one finds that the velocity of the atom is damped exponentially with the damping rate to be

$$\gamma = \frac{\alpha_{max}(I_A)}{m_{Be}} = \frac{E_R}{2\hbar}, \tag{3.9}$$

where $E_R = \frac{\hbar^2 k_L^2}{2m_{Be}}$ is the recoil energy a Be^+ ion experiences when it absorbes one photon. The characteristic damping time is therefore $\gamma^{-1} = 1.4\,\mu s$.

limit of Doppler cooling

To find the minimum temperature achievable with Doppler cooling an expression for the cooling and heating rates need to be found. In the following we assume $k_L v_z \ll \Gamma$. Using the expression for the cooling

force in eq. (3.6) one can write the equation of motion $m\dot{v} = -\alpha v$. Multiplying both sides with $\dot{v}$ gives an expression for the kinetic energy K of the particle, and the cooling rate is:

$$\dot{K}_{cooling} = \frac{-2\alpha}{m} K \tag{3.10}$$

For a red-detuning the friction coefficient is positive, and the ion will lose kinetic energy. For the heating rate one has to consider that with each photon absorbtion or emission the ion gains the recoil energy E_R. Therefore one can write by using the scattering rate Γ_{sc} defined in eq. (3.4):

$$\dot{K}_{heating} = 2E_R\Gamma_{sc}. \tag{3.11}$$

At equilibrium cooling and heating rates must be equal but with the opposite sign, $-\dot{K}_{cooling} = \dot{K}_{heating}$. Evaluating this expression leads to the minimal energy at thermal equilibrium,

$$K = -\hbar \cdot \frac{\Gamma^2 I + (\Gamma^2 + 4\Delta\omega^2) \cdot I_{sat}}{16\Delta\omega I_{sat}}, \tag{3.12}$$

which is only depending on the intensity I of the cooling laser and the detuning $\Delta\omega$. For small intensities $I \to 0$ and a detuning of $\Delta\omega = -\Gamma/2$ one finds the Doppler temperature to be

$$T_D = \frac{\hbar\Gamma}{2k_B}, \tag{3.13}$$

which is only depending on the linewidth of the cooling transition. For $I = 2I_{sat}$ this temperature limit is two times larger. For the $^2\mathrm{S}_{1/2} \leftrightarrow {}^2\mathrm{P}_{3/2}$ transition in Be^+ one obtains $T_D(I_{sat}) = 0.47\,\mathrm{mK}$ and $T_D(2I_{sat}) = 0.93\,\mathrm{mK}$.

3.2 Cooling Lasers at 313 nm for Beryllium Ions

Figure 3.4 shows the $^9\mathrm{Be}^+$ energy levels. The electronic configuration is $1s^2\,2s^1$, and the spin of the nucleus is I = 3/2, resulting in a hyperfine splitting of $\nu_{HFS} = 1.25\,\mathrm{GHz}$ between $F = 1$ and $F = 2$ for the $S_{1/2}$ state, and smaller splittings of about 1 MHz

atomic transition

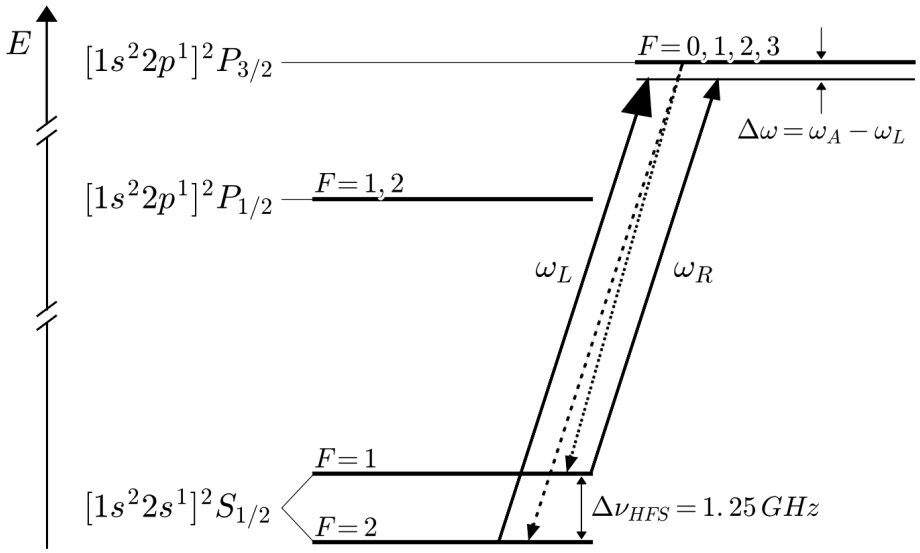

Figure 3.4: $^9Be^+$ *energy levels and relevant transitions.*

from $F = 0$ to $F = 3$ for the P states. The transition we are interested in is $^2S_{1/2}(F = 2) \leftrightarrow {}^2P_{3/2}$, with a corresponding frequency of $f_{Be} = 957\,397\,084.8\,\text{MHz}$ [59] and a natural linewidth of $\Gamma_{Be} = 19.4\,\text{MHz}$.
The excited $^2P_{3/2}$ state can decay into both hyperfine levels of the ground state. One solution to close the transition cycle is the implementation of a second laser with a detuning of 1.25 GHz. In the experiment developed during this thesis the repumping is realized with a resonant electro-optical modulator. Another solution is the usage of optical pumping by σ^+ or σ^- polarized light and a $\boldsymbol{B}$ field parallel to the laser beam, such that only the transition $^2S_{1/2}(F = 2, m_F = \pm 2) \leftrightarrow {}^2P_{3/2}(F = 3, m_F = \pm 3)$ is driven [62].

requirements

While designing the laser source for such a cooling cycle one needs to keep the initial temperature of the ions in mind and the tuning range should cover this. A detuning range of a couple of GHz is sufficient to address all the particles well in the Maxwell Boltzmann distribution of the particles. The requirements are therefore:

- a wavelength at 313.133 nm
- a power output and focalisation reaching the saturation limit of $I_{sat} = 0.83\,\text{mW/mm}^2$
- a detuning range of up to 3 GHz
- a linewidth of $< 2\,\text{MHz}$

Producing light with these properties is not straightforward, since laser sources directly emitting at this wavelength do not exist. Therefore a couple of different solutions were developed in the last years, which can be divided into expensive high power sources and less expensive low power sources.

- high power sources: One solution is the second harmonic generation (SHG) of a dye laser at 626 nm [63], which is demanding concerning the stabilization. Another solution is the sum frequency generation of 626 nm light, based on fiber lasers at 1550 nm and 1051 nm, and thereafter SHG [64]. This very stable approach was used in the experiment presented here and is explained in section 3.2.2. Lo et al. reported in 2015 for a similar setup an overall production of up to 2.4 W at 313 nm [65]. A further high power and stable implementation is based on the frequency quintupling of a laser at 1565 nm [66].

- low power sources: These are based on commercially available laser diodes which are emitting between 635 nm and 637 nm. By cooling these diodes down to $-20\,^{\circ}\mathrm{C}$ - $-40\,^{\circ}\mathrm{C}$ the wavelength can be pushed down to 626 nm and the diodes are usually operated in the Littrow configuration [67, 62].
  As part of this thesis a DBR diode laser in a master slave configuration was developed in collaboration with the Vrije Universiteit Amsterdam and the Johannes Gutenberg-Universität in Mainz (see section 3.2.1). In addition another idea was followed, by implementing an external cavity diode laser (ECDL) with an interference filter, following the idea in [68]. Here the cooled diode and a tunable coupling present a novelty.

frequency doubling

Following the creation of light at 626 nm a frequency doubling cavity with a BBO crystal is used to generate the desired light at 313 nm. The cavity used in this experiment is explained in section 3.2.3.
The master-slave setup for the DBR diode is currently operated at the group of L. Guidoni at Paris 7 in order to detect sympathetically cooled beryllium ions in a strontium ion crystal. The same setup is used at the Universität in Mainz for Be^+/Ca^+ sympathetic cooling experiments. The ECDL configuration is more demanding for stabilization and the testing of different diodes is still ongoing.

3.2.1 Master Slave System

As noted before the ${}^2S_{1/2}(F = 2) \leftrightarrow {}^2P_{3/2}$ transition in beryllium needs a tunable, high power and narrow linewidth continuous wave laser in a frequency range, which is not covered by commercial products.
In Fig. 3.5 one can see an overview over the master-slave setup for the DBR laser diode. The master laser consists of a Distributed Bragg Reflector (DBR) diode laser (see below), and after some beamshaping the output is divided into two beams, one which can be used to monitor the frequency of the master and one for injection locking of the slave laser. The slave injection is done via a double stage optical

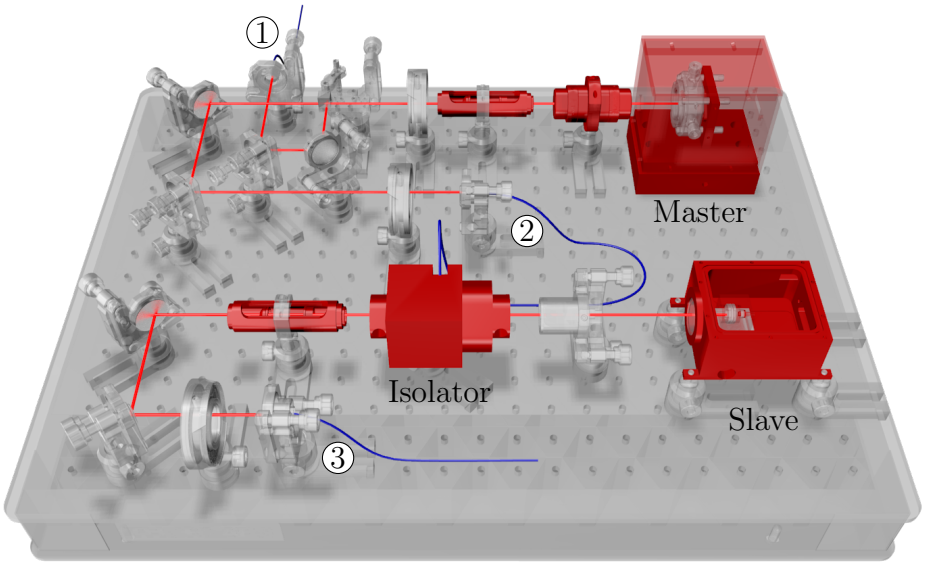

Figure 3.5: *Setup of the master slave setup with optical elements. The fiber port ① is to monitor the master frequency, ② is for the injection of the master laser into the slave via a double stage optical isolator, and ③ goes to the frequency doubling cavity.*

isolator. This way the complete output of the slave laser is available for frequency doubling in a bow tie cavity, ≈ 150 mW at 626 nm before injecting into the fiber and about 70 mW in front of the cavity. This transforms to approximately 1 mW of light at 313 nm.

DBR as master

In the setup presented here a Distributed Bragg Reflector (DBR) diode laser based on AlGaInP is used as master laser [69]. The designers of this diode had cooling of Be^+ in mind. The structure of a DBR is layered, such that the different layers act as an internal grating. This makes the ECDL tuning problems for the grating in the Littrow configuration obsolet. In order to reach the desired wavelength the DBR diode needs to be cooled, for which reason the diode comes with a Peltier element, in a standard TO-3 package and is mounted on a watercooled, custom made brass mount (see Fig. 3.6, top right). To collimate the beam a Thorlabs $\hat{x}\hat{y}$ translation stage with a collimation lens is mounted directly in front of the DBR diode.

The characterization of the DBR can be seen in Fig. 3.6. The detuning range without a mode jump is at −8.6 °C around $\lambda_{626} = 626.265$ nm approximately 20 GHz, which is more than required.
The power output for this choice of parameters is around 35 mW. At the bottom right of Fig. 3.6 a beatnote measurement of the DBR with a fiber laser is shown, which consists of 25 individual measurements. Since the DBR was free running this resulted in a shifted center frequency of the beatnote for each mesurement. To obtain the data which is shown the dataset of each measurement was first fitted with a Lorentzian to determine the line center and then shifted to a

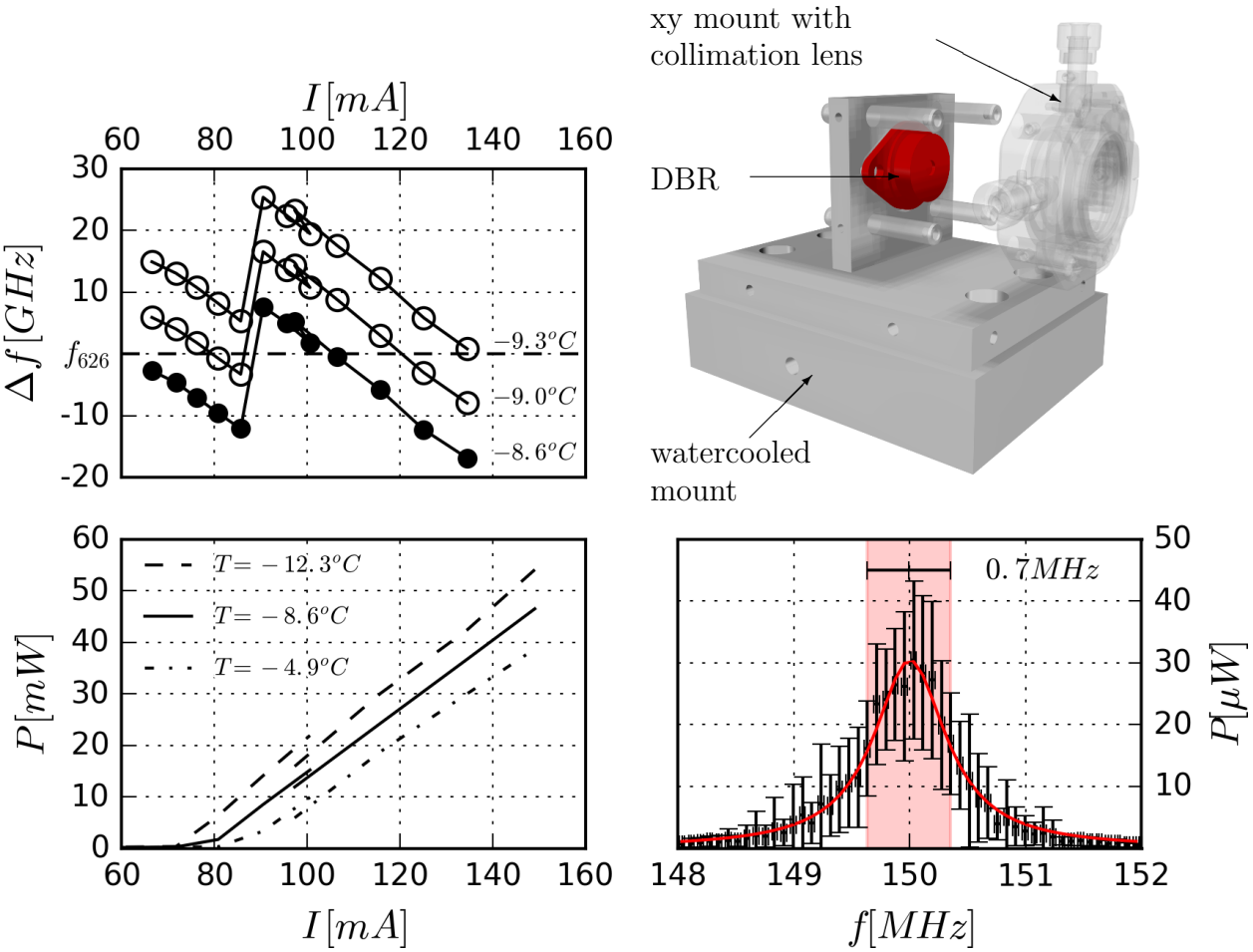

Figure 3.6: *Top left: The emitted frequency around* $f_{626} = 626.265\,\text{nm}$ *depending on the injection current. Top right: Design of the DBR mount. Bottom left: The emitted power as a function of the current. Bottom right: Beatnote with a fiber laser and a Lorentzian fit.*

common position. After averaging the data again another Lorentzian fit was done, resulting in a beatnote linewidth of 0.7 MHz. Since the fiber lasers are much narrower (below 100 kHz), this width can be fully attributed to the DBR laser, and results in a width of 1.4 MHz at 313 nm after SHG.

ECDL as master

The ECDL setup is shown in Fig. 3.7. The laser diode and the collimation lens are mounted on a double stage Peltier element in a waterproof box and operated around −20 °C. The wavelength selection is done by an interference filter instead of a diffraction grating, following the design in [68], which is less sensitive to misalignment than the Littrow grating arrangement. The novelty as compared to the design in [68] is that the setup presented here includes a waveplate and a polarizing beam splitter cube, which allows for a tuning of the feedback ratio and output power.

Two different setups were investigated, in order to get the highest output while keeping enough feedback to have a stable behaviour.

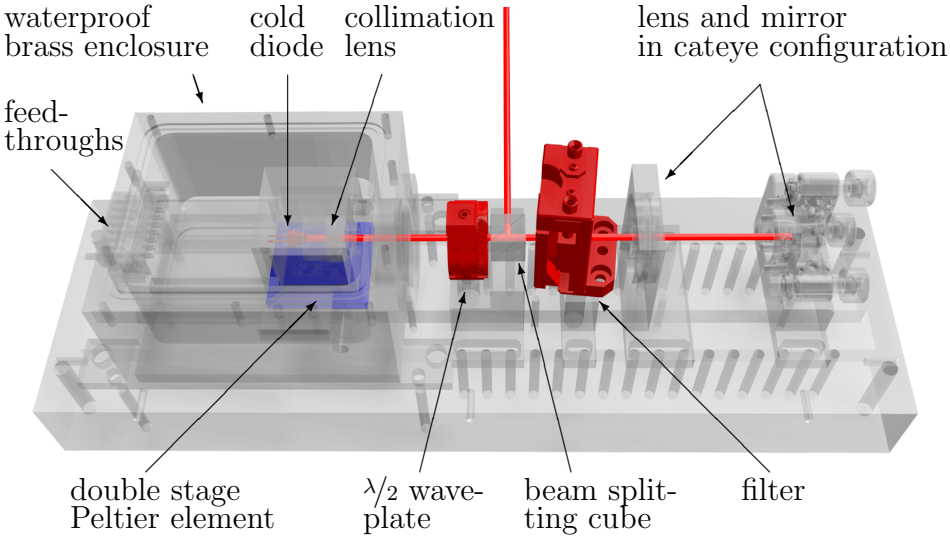

Figure 3.7: *The ECDL laser in the λ/2 configuration. For the λ/4 configuration the beam splitting cube and the waveplate change position.*

The first implementation is shown in Fig. 3.7. The output of the diode is split directly after into two beams, using a λ/2 waveplate and a polarizing beam splitter cube. The output is available after the cube, while the beam for the feedback passes the filter and is reflected back to the diode. In the second configuration the diode-output is completely passing the beam splitting cube and then a λ/4 waveplate. After the filter and the reflection on the mirror a part of the beam is coupled out by the cube, while the other part is used as feedback for the diode. To compare the two setups the Jones calculus [70] is used, which describes the behaviour of polarized light. The Jones matrices for the transmission and the reflection of the beam splitting cube and the mirror are

$$J_{cube,t} = \begin{pmatrix} 1 & 0 \\ 0 & 0 \end{pmatrix}, \; J_{cube,r} = \begin{pmatrix} 0 & 0 \\ 0 & 1 \end{pmatrix} \text{ and } J_{mirror} = \begin{pmatrix} -1 & 0 \\ 0 & -1 \end{pmatrix}, \tag{3.14}$$

and for the waveplates in their eigenbasis

$$J_{\lambda/2} = \begin{pmatrix} -i & 0 \\ 0 & i \end{pmatrix}, \quad J_{\lambda/4} = \frac{1}{\sqrt{2}} \begin{pmatrix} 1-i & 0 \\ 0 & 1+i \end{pmatrix}. \tag{3.15}$$

To take the rotation of the waveplates regarding the eigenaxis of the cube into account, the rotation matrices $J_R(-\theta)$ and $J_R(\theta)$ are used. The total Jones matrices for the λ/2 system can then be written as

$$J^{tot}_{\lambda/2,feedback}(\theta) = \widetilde{J}_{\lambda/2}(\theta) \cdot J_{cube,t} \cdot J_{mirror} \cdot J_{cube,t} \cdot \widetilde{J}_{\lambda/2}(\theta) \tag{3.16}$$

$$J^{tot}_{\lambda/2,output}(\theta) = J_{cube,r} \cdot \widetilde{J}_{\lambda/2}(\theta), \tag{3.17}$$

and for the $\lambda/4$ system

$$J^{tot}_{\lambda/4,feedback}(\theta) = J_{cube,t} \cdot \widetilde{J}_{\lambda/4}(\theta) \cdot J_{mirror} \cdot \widetilde{J}_{\lambda/4}(\theta) \cdot J_{cube,t} \tag{3.18}$$

$$J^{tot}_{\lambda/4,output}(\theta) = J_{cube,r} \cdot \widetilde{J}_{\lambda/4}(\theta) \cdot J_{mirror} \cdot \widetilde{J}_{\lambda/4}(\theta) \cdot J_{cube,t} \tag{3.19}$$

with $\widetilde{J}_{\lambda/n} = J_R(-\theta) \cdot J_{\lambda/n} \cdot J_R(\theta)$. This leads to analytic expressions for the intensities of the feedback and the output of the system,

$$I_{\lambda/2,feedback} = P_{max} \sin^2[2\theta] \text{ and } I_{\lambda/2,output} = P_{max}\,\eta^2 \cos^4[2\theta] \tag{3.20}$$

$$I_{\lambda/4,feedback} = P_{max}\,\eta^2 \sin^2[2\theta] \text{ and } I_{\lambda/4,output} = P_{max}\,\eta^2 \cos^2[2\theta], \tag{3.21}$$

with P_{max} being the output power of the diode laser and $\eta \approx 0.8$ the transmission coefficient of the filter. At the top of Fig. 3.8 these intensities are plotted as a function of the waveplate angle. At the bottom left the measured data is plotted for the $\lambda/2$ configuration, with the diode current as parameter, ranging from $I_{diode} = 55\,\text{mA}$ to 130 mA. The curves fit well with eq. (3.20) if an offset angle $\Delta\Theta$ is introduced. For a small feedback and the highest current one obtains $\approx 70\,\text{mW}$ of red light at 626 nm. The small shift of the symmetry axis in the plot by $\Delta\Theta = 2\,^\circ$ can be attributed to the not perfectly aligned eigenaxis of the laser diode and the eigenaxis of the beam splitting cube, since it is difficult to position the small diode at the ideal angle.

Operating the laser diode in a stable regime does not require a big amount of feedback. In Fig. 3.8 at the bottom right the output power is plotted as a function of the feedback, using equations (3.20) and (3.21). For a small feedback the $\lambda/2$ configuration delivers a higher output, while for a higher feedback the $\lambda/4$ configuration delivers only a little bit more power. This changes depending on the transmission of the used filter. For a very high transmission of $\eta \approx 1$ the $\lambda/4$ configuration would give a higher output at the same feedback, but due to the 80% transmission of the used filter the $\lambda/2$ configuration leads to a higher power output, since the output beam is not absorbed twice in the filter. In summary one can say:

- The ECDL output power is high enough to perform SHG and use the light at 313 nm with $\approx 1/4\,\text{mW}$ as repumping beam or

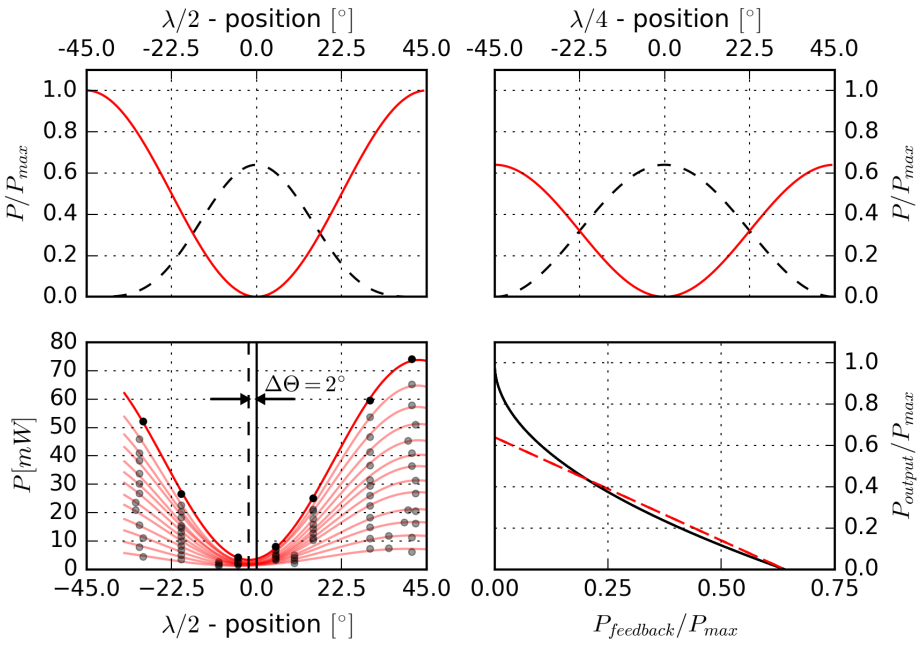

Figure 3.8: *Top: The feedback (dashed lines) and output intensities (solid lines) for the two different configurations from eq. (3.20) and (3.21). Bottom left: Fitted measurement of the power output for the configuration with the λ/2 waveplate. The first ten curves (from bottom to top) correspond to diode currents from* 55 mA *to* 100 mA *in steps of* 5 mA*, and the last three are for* 110 mA, 120 mA *and* 130 mA*. Bottom right: The output intensities as a function of the feedback.*

Doppler cooling beam. The power of the ECDL alone is not high enough for SHG and Doppler cooling.

- The ECDL shows less stable behaviour compared to the DBR diode laser, making the operation more challenging.
- The fact that laser diodes at 633 nm are commercially available makes the ECDL setup a cheaper solution than for example the usage of an electro-optical modulator to generate repumping sidebands.

slave laser

For the slave laser a commercial GaAs laser diode Opnext HL63133DG is used. This diode operates at room temperature at ≈ 635 nm and needs to be cooled down to −30 °C to operate at 626 nm. In order to avoid condensing a hermetic enclosure was designed, which can be water cooled and is shown in Fig. 3.9.

The diode itself is mounted into a custom made aluminum cube, including the collimation lens. The aluminum cube is placed on a Marlow NL2063T double stage Peltier element, which is glued to the brass enclosure. Since the housing must be airtight, all the openings are designed keeping this in mind. The electrical DB9 connector is watertight, and an O-ring is used in between the brass enclosure and

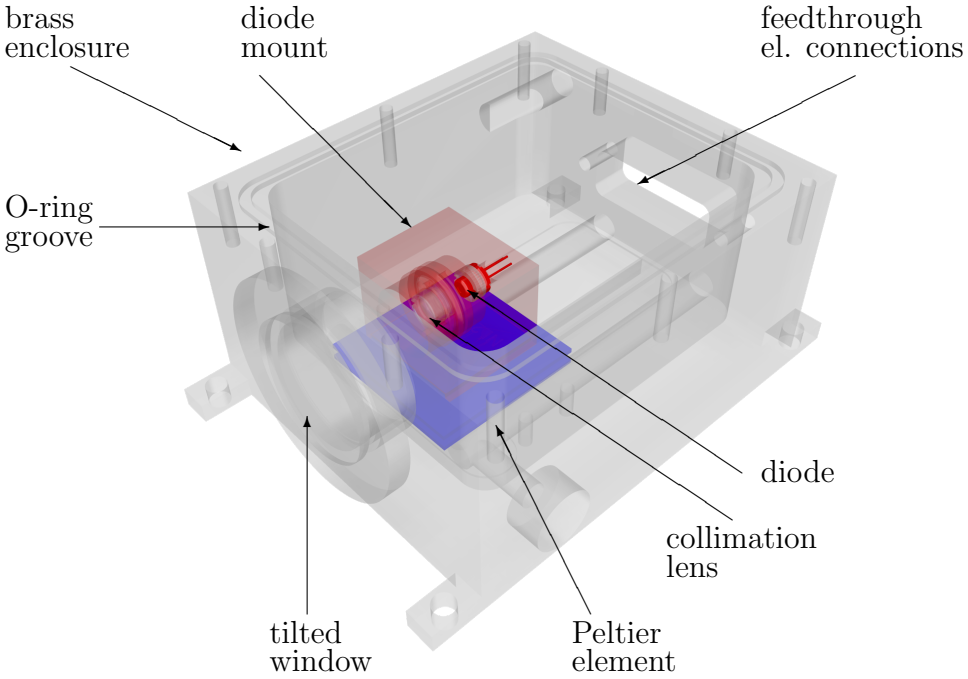

Figure 3.9: *The hermetic enclosure for the slave laser and collimation objective.*

the cover. The window for the exit of the laser light is glued with Araldite and mounted with a small angle to ensure no backreflections. The brass enclosure also has two openings to apply water cooling via a chiller.

In Fig. 3.10 beatnote measurements of the free running slave and the injected slave with a fiber laser are shown. The injection narrows the linewidth from 33.6 MHz down to 0.7 MHz, the linewidth of the DBR master laser.

3.2.2 Fiber Laser

A reliable and easy to maintain, but expensive source for 626 nm light is sum frequency generation with two fiber lasers at 1051 nm and 1550 nm, as originally developed at NIST [64]. The setup is shown in Fig. 3.11.

The first laser (fl-1) is a NKT fiber laser, which delivers up to 10 mW at 1051 nm and is subsequently amplified in a NKT fiber amplifier (ampl-1), resulting in up to 4.5 W. The second fiber laser (fl-2) is also a NKT product, producing 45 mW at 1550 nm which are also amplified (in ampl-2), delivering up to 5.25 W. The settings used to obtain the results of the next chapter are shown in table 3.1, where the pump current of both amplifiers is set to 4.5 A.

In order to take the light from the two amplifiers to the optical table

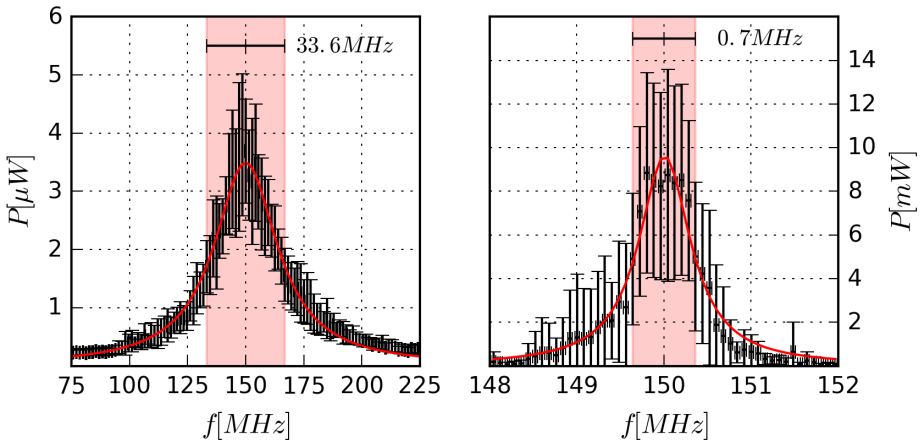

Figure 3.10: *Left: Beatnote of the free running slave laser with the fiber laser output and a Lorentzian fit. Right: Beatnote of the injected slave laser with the fiber laser and a Lorentzian fit.*

	fl-1	ampl-1	fl-2	ampl-2
wavelength	1050.892 nm		1549.950 nm	
output power	10 mW	2.0 W	10 mW	1.3 W

Table 3.1: *Settings for the fiber lasers*

polarization maintaining fibers are used. The output collimators deliver beams with a $1/e^2$ diametre of 2 mm. The light exiting these two fibers is combined using a longpass dichroic filter (model DMLP1180 from Thorlabs), with a reflectivity close to 1 for the 1051 nm light and a transmission of > 0.95 for the 1550 nm light. Thereafter the combined beams are sent to a PPLN crystal from Covesion. The dimensions of the crystal are 40 mm × 10 mm × 0.5 mm ($l \times w \times h$) and the input and output facets are AR coated with a reflectivity of less than 1% for light at 626 nm, 1051 nm and 1550 nm. The PPLN crystal is placed in an oven, which is heated to 173.52 °C. This temperature is chosen to optimize the sum frequency generation efficiency. The 626 nm output is coupled into a fiber for a convenient guiding to the cavity (see below).

3.2.3 Bow Tie Cavity

The cavity used in this experiment is similar to the one used in [62] and [71], and was designed by F. M. J. Cozijn et al. in Amsterdam. Similiar to the recent publication by Schmidt et al. the cavity consists of one monolithic block in order to minimize mechanical instabilities [72]. In Fig. 3.12 the complete setup for the generation of 313 nm light including the repumping beam is shown.

The red 626 nm light is brought to the setup by a fiber, having the

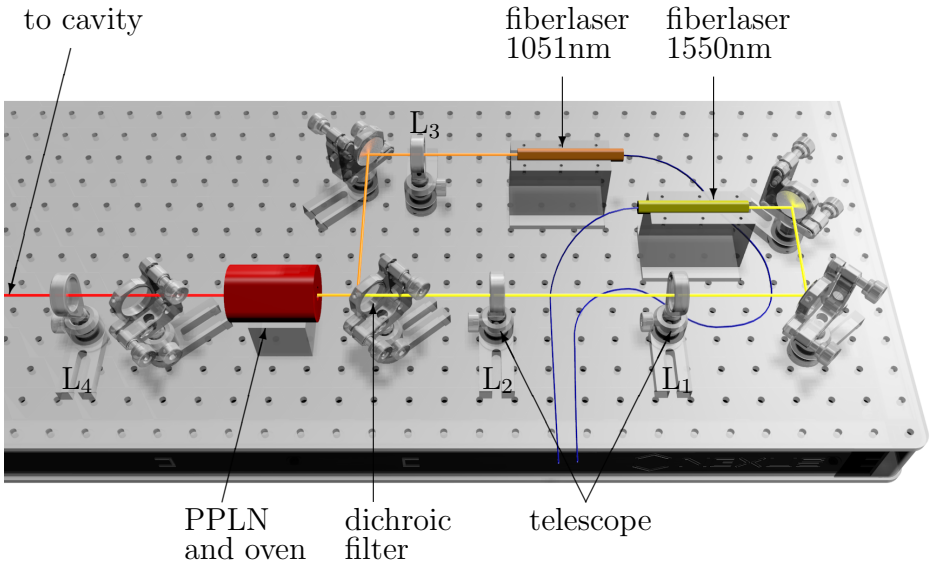

Figure 3.11: *Setup of the two fiber lasers for the sum frequency generation of* 626 nm *light. The focal lengths of the lenses* L_i *are:* $f_{L_1} = -50\,\text{mm}$, $f_{L_2} = 60\,\text{mm}$, $f_{L_3} = 125\,\text{mm}$ *and* $f_{L_4} = 200\,\text{mm}$.

advantage of being able to quickly change between the master-slave setup and the fiber laser setup as a source of light. Thereafter the two lenses $f_{L_1} = 35\,\text{cm}$ and $f_{L_2} = 50\,\text{cm}$ modify the beamsize to fit the cavity beam profile. A small part of the 626 nm beam is coupled into another fiber, in order to monitor the frequency with a wavemeter. The cavity length is stabilized by using the Hänsch-Couillaud scheme [73], which uses the reflection of the incoming beam to apply feedback to a piezoceramic actuator, which is mounted behind mirror M_3. The repumping beam with a detuning of 1.25 GHz is provided by a resonant EOM developed by QUBIG, which is designed for this purpose.

phase matching

The core of the frequency doubling cavity is a 12 mm long, Brewster-cut Beta-Barium-Borate ($\beta - BaB_2O_4$, BBO) nonlinear crystal for second harmonic generation (SHG) of 313 nm light. In order for the SHG to be efficient, the wavevectors of the fundamental and second harmonic beam must fulfill the phase-matching condition $\boldsymbol{k}_{313} = 2\boldsymbol{k}_{626}$, otherwise destructive interference minimizes the efficiency of the crystal. However, chromatic dispersion causes a phase mismatch between the wavevectors. In order to overcome this problem one can take advantage of the birefringence of the BBO, which causes different refraction indices for the ordinary and extraordinary polarizations. By choosing an appropriate angle Θ_{pm} for the beams with the optical axis of the crystal, the phase-matching condition can be satisfied. For the SHG with 626 nm the phase-matching angle is $\Theta_{pm} = 38.4\,^\circ$ [72]. However, one problem in a birefringent crystal is the resulting angle between the Poynting vectors of the fundamental beam and the second harmonic. This angle is called walk-off angle, and for the present case has a value of $\rho = 4.6\,^\circ$ [64]. It leads to a walk-off parameter

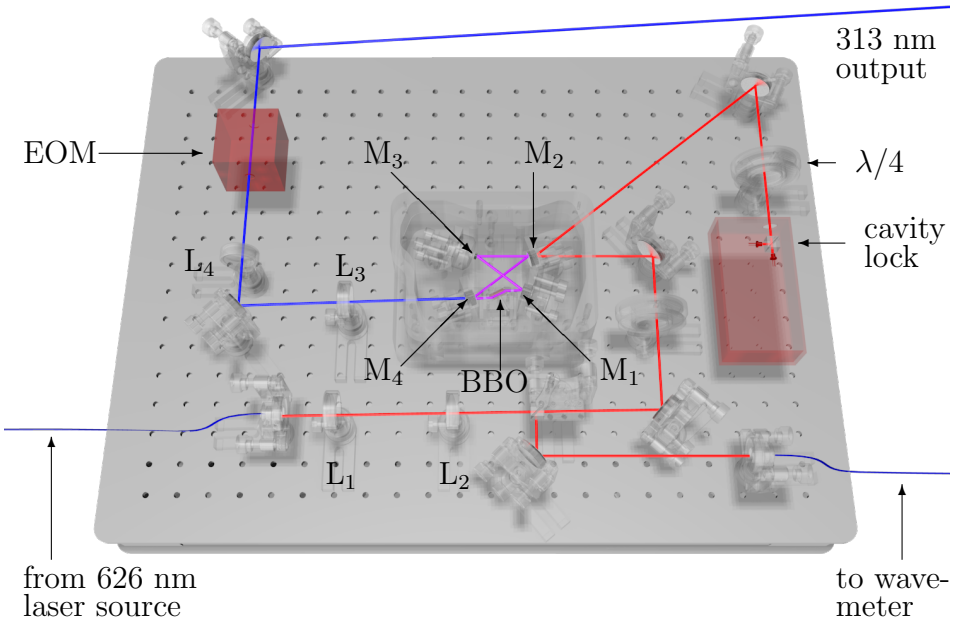

Figure 3.12: *The bow-tie shaped enhancement cavity.*

$B = \rho/2\sqrt{l_c k}$ which is large for BBO. This strong walk-off requires a small focus of the beam inside the crystal, in order to maintain an overlap between the fundamental and the SHG beam.

Brewster cut In order to minimize losses of the fundamental beam due to reflection at the transition air-crystal, the BBO is Brewster-cut for the fundamental beam. For 626 nm in a BBO crystal Brewster's angle is $\Theta_B = \arctan[n_0] = 59.05\,^\circ$, with n_0 being the index of refraction for the fundamental beam.

beam waist The SHG power generated in a BBO is proportional to the square of the fundamental beam intensity if the pump depletion regime is not reached. A smaller waist of the fundamental beam in the crystal increases the intensity at the focus, but reduces the intensity away from the focus. Using the Boyd and Kleinman model [74] one can find an optimum focusing ratio $l_c/b = 2.84$, with the crystal length l_c and the confocal parameter $b = w_0^2 k$, where $k = 2\pi/\lambda$. For a crystal length of $l_c = 12\,\text{mm}$ one obtains an optimal waist of $w_0 \approx 20.5\,\mu\text{m}$.

cavity design The single-pass conversion efficiency of a BBO crystal is typically $< 0.01\%$. To enhance the power output a bow-tie cavity is build around the crystal. Once the optimum beam waist is found, one can design a cavity which provides this waist. This waist inside the crystal is determind by the curvature of and the distance between the mirrors M_1 and M_4 (see Fig. 3.13).
The behaviour of a Gaussian beam in the cavity can be analyzed using the $ABCD$ matrix formalism. A Gaussian beam is described by the complex parameter $q(z)$, which is connected to the real beam parameters $R(z)$, the radius of curvature of the beam, and $w(z)$, the waist of the beam, by the relation [50]

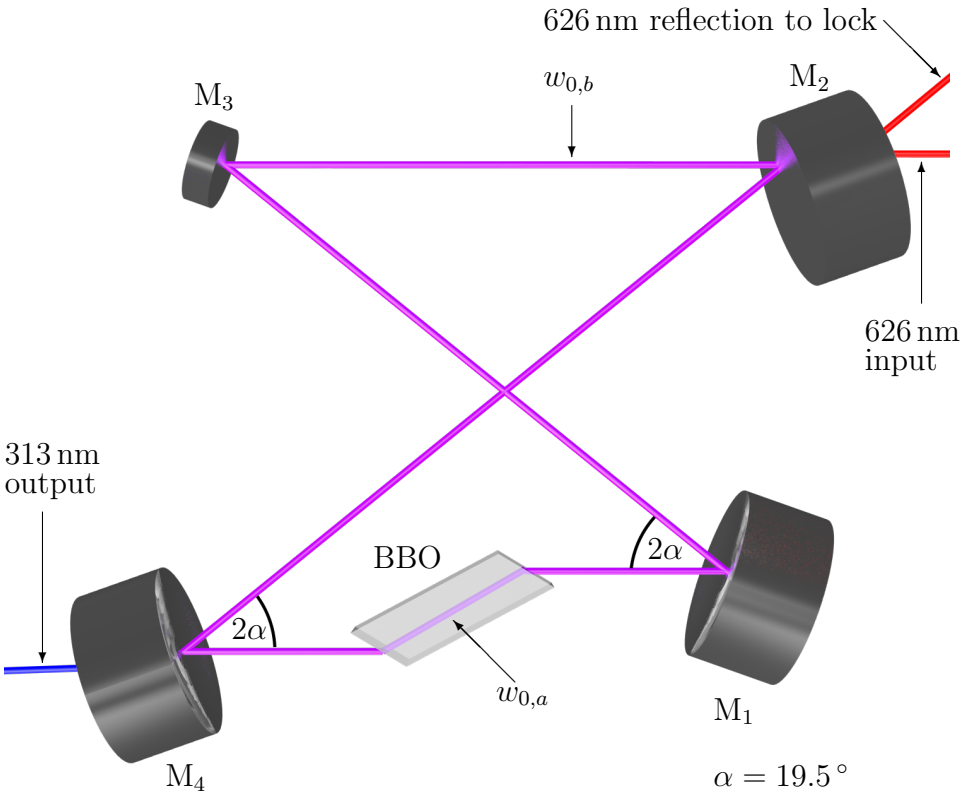

Figure 3.13: *Layout of the bow-tie cavity with relevant geometric parameters. Values for the beamwaists can be found in table 3.2.*

$$\frac{1}{q(z)} = \frac{1}{R(z)} - i\,\frac{\lambda}{\pi n w^2(z)} \tag{3.22}$$

The propagation of Gaussian beams through different optical elements is then described using the $ABCD$-matrix formalism. The ray transfer matrices are applied on the q parameter

$$\boldsymbol{M} = \begin{pmatrix} A & B \\ C & D \end{pmatrix} \rightarrow q_1 = \frac{Aq_0 + B}{Cq_0 + D}, \tag{3.23}$$

where q_0 is the initial value and q_1 the one found after propagation through the optical element(s) described by the matrix $\boldsymbol{M}$. For stable operation the q parameter of the beam must be the same after one roundtrip in the cavity, such that $q_0 = q_1$. This condition leads to an expression for the beamwaist

$$w_0 = \sqrt{\frac{\lambda}{\pi\, n}\sqrt{-B/C}}. \tag{3.24}$$

The geometry of the cavity is shown in Fig. 3.13. For the investigation of this cavity three different kind of ray matrices are needed:

$$\boldsymbol{M}_p(d) = \begin{pmatrix} 1 & d \\ 0 & 1 \end{pmatrix}, \; \boldsymbol{M}_r(n_1/n_2) = \begin{pmatrix} 1 & 0 \\ 0 & n_1/n_2 \end{pmatrix}, \\ \text{and } \boldsymbol{M}_m(f) = \begin{pmatrix} 1 & 0 \\ -1/f & 1 \end{pmatrix}, \tag{3.25}$$

where $\boldsymbol{M}_p(d)$ describes the propagation of the beam for a distance d, $\boldsymbol{M}_r(n_1/n_2)$ the effect of passing through a dielectric plane with refraction indices n_1 and n_2, and $\boldsymbol{M}_m(f)$ a thin lens or mirror with focal length f. Chosing the center of the crystal as a starting point, the complete effect of the cavity can then be written as

$$\begin{aligned} \boldsymbol{M}_{tot} =& \boldsymbol{M}_p(l_c/2) \cdot \boldsymbol{M}_r(1/n_c) \cdot \boldsymbol{M}_p((d-l_c)/2) \cdot \boldsymbol{M}_m(f) \cdot \boldsymbol{M}_p(l-d) \\ & \cdot \boldsymbol{M}_m(f) \cdot \boldsymbol{M}_p((d-l_c)/2) \cdot \boldsymbol{M}_r(n_c/1) \cdot \boldsymbol{M}_p(l_c/2). \end{aligned} \tag{3.26}$$

Because of the angle α (see Fig. 3.13) of the mirrors with respect to the beam, the focal lengths for the mirrors need to be corrected, which leads to different waists in the sagittal (the plane defined by the beampath in the cavity) and tangential plane (perpendicular to the sagittal plane). These corrections are

$$f_{sag} = \frac{r}{2} \frac{1}{\cos[\alpha]} \text{ and } f_{tan} = \frac{r}{2} \cos[\alpha]. \tag{3.27}$$

Additionally, in the tangential plane, the astigmatism compensation due to the Brewster cut needs to be taken into account. This leads to a modified matrix for the transition between crystal and air and vice versa:

$$\boldsymbol{M}_r(n_1/n_2) \rightarrow \boldsymbol{M}_{Brewster}(n_1/n_2) = \begin{pmatrix} n_2/n_1 & 0 \\ 0 & n_1^2/n_2^2 \end{pmatrix}. \tag{3.28}$$

The top of Fig. 3.14 shows the dependence of the beam waists $w_{0,a}$ and $w_{0,b}$ of the distance d in between mirrors M_1 and M_4 in the sagittal and tangential plane. The cavity is operated at a distance $d = 40\,\text{mm}$. The resulting values for the waists can be seen in table 3.2.

build-up

Since the power of the SHG increases quadratically with the power of the fundamental beam, the power at 313 nm increases strongly with the build-up in the cavity. The build-up in a cavity can be calculated by using [75]

$$P_{bu} = \frac{T_2\, P_{626}}{(1-\sqrt{R_2 R})^2 \,+\, 4\sqrt{R_2 R}\,\sin^2\left[\phi/2\right]}, \tag{3.29}$$

where T_2 and R_2 are the transmission and the reflectivity of the incoupling mirror M_2, $R = (1-L_L)(1-L_{NL})$ with L_L being all the linear losses in the cavity and L_{NL} the non-linear losses in the crystal.

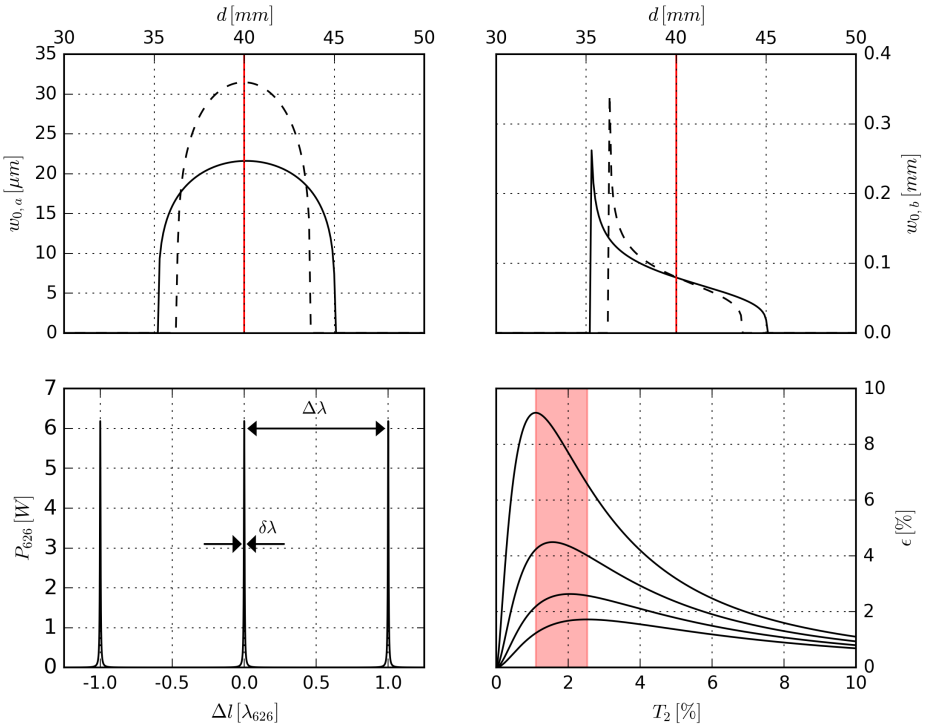

Figure 3.14: *Top: The beamwaists $w_{0,a}$ (left) and $w_{0,b}$ (right) in the sagittal plane (solid line) and the tangential plane (dashed line) as function of the distance d between the curved mirrors (relevant parameters can be found in Table 3.2). Bottom left: Airy function of the cavity as a function of the detuning of the cavity length in units of the wavelength for the red light. Bottom right: The doubling efficiency for different total linear losses in the cavity, as a function of the transmission T_2 of the incoupling mirror M_2. The linear losses range from $L_L = 1.0\,\%$ (top curve) to $L_L = 2.5\,\%$ (bottom curve) in steps of $0.5\,\%$. The colored area marks the region of the maxima of the curves.*

$\phi = 2\pi L/\lambda$ is the phase of the fundamental beam after one roundtrip, with the optical length L of the cavity. At the bottom left of Fig. 3.14 the build up P_{bu} of the cavity is plotted for an input power of 100 mW as a function of the detuning of the cavity length, and the free spectral range $\Delta\lambda$ and the full-width half-maximum $\delta\lambda$ are indicated as well. The finesse of the cavity is given by $\mathcal{F} = {}^{\Delta\lambda}/_{\delta\lambda} \approx 184$.

efficiency

The conversion efficiency is defined as $\epsilon = {}^{P_{313}}/_{P_{626}}$, and one can find an implicit expression for the conversion efficiency [76]

$$\sqrt{\epsilon} = \frac{4T_2\sqrt{L_{NL}\,P_{626}}}{\left[2-\sqrt{1-T_2}\,(2-L_L-\sqrt{\epsilon L_{NL}P_{626}})\right]^2}. \tag{3.30}$$

impedance matching

In order to couple the complete fundamental power P_{626} into the cavity, the transmission of the incoupling mirror must compensate all the losses in the cavity. At the bottom right of Fig. 3.14 the conversion efficiency is plotted as a function of T_2, with $L_{NL} = 1.1 \cdot 10^{-4}$ and four different values for the linear losses $L_L = 0.010$, 0.015, 0.020 and 0.025. Depending on the parameter L_L the maximum of these curves ranges in between $T_2 = 1.1\%$ and $T_2 = 2.5\%$. Since it is difficult in a real setup to estimate all the losses, mirrors with transmissions $T_2 = 0.7\%$, $T_2 = 1.2\%$ and $T_2 = 1.8\%$ have been tested. Best results were obtained for $T_2 = 1.8\%$. In Table 3.2 the parameters of the cavity are summarized.

BBO dimensions	$l \times w \times h = 12 \times 4 \times 4\,\mathrm{mm}^3$
phasematching angle	$\Theta_{pm} = 38.4\,^\circ$
Brewster's angle	$\Theta_B = 59.05\,^\circ$
radius of curvature M_1 and M_4	$r = 30\,\mathrm{mm}$
angle on curved mirrors	$\alpha = 19.5\,^\circ$
distance mirror to crystal	${}^{(d-l_c)}/_2 = 14.6\,\mathrm{mm}$
geomeric roundtrip length	$l_{roundtrip} = 184.9\,\mathrm{mm}$
waist sagittal in crystal	$w_{0,a}^{sag} = 21.3\,\mu\mathrm{m}$
waist tangential in crystal	$w_{0,a}^{tan} = 30.9\,\mu\mathrm{m}$
waist sagittal between M_2 and M_3	$w_{0,b}^{sag} = 88.7\,\mu\mathrm{m}$
waist tangential between M_2 and M_3	$w_{0,b}^{tan} = 92.4\,\mu\mathrm{m}$
finesse of the cavity	$\mathcal{F} \approx 184$

Table 3.2: *Parameters of the BBO and the cavity*

power output

In Fig. 3.15 the output power of the cavity depending on the input power is shown. For this measurement the fiber system described in the section before was used, and a comparison with the results in [64] shows that the cavity is well matched. We obtain up to 25 mW of 313 nm light for 360 mW of red light in front of the cavity.

3.3 Other Laser Sources in this Experiment

In addition to the cooling laser for beryllium three other laser sources are required, including the ionization laser for the state selected preparation of the H_2^+ ions, the spectroscopy laser, and the dissociation laser. In the following a short overview is given for each of the necessary setups.

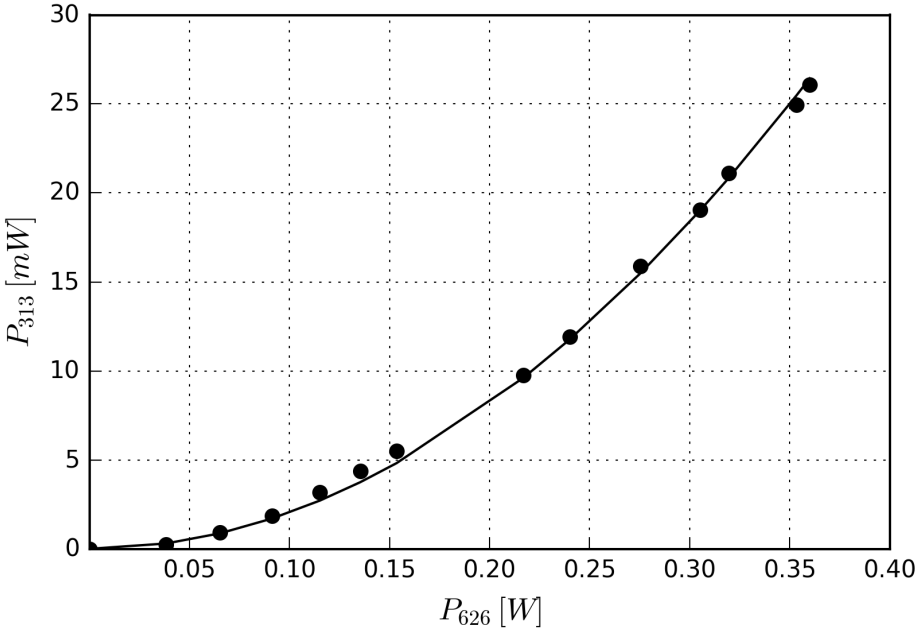

Figure 3.15: *Cavity power output*

3.3.1 The REMPI Laser

A simple way for H_2 ionization is by electron impact ionization, using an e-gun. However, using this process one ends up with only $\approx 1.4\%$ of the H_2^+ ions in the ro-vibrational state $\nu = 0, L = 2$, the ground-state for the transition from interest [77].
In order to create a higher percentage of the H_2^+ ions in the right ro-vibrational state, resonance-enhanced multiphoton ionization (REMPI) is used. The principle of this process can be divided into two parts, where both parts can utilize one or more photons. First the H_2 molecules are excited by absorption of n photons in an intermediate state, often a Rydberg state. In the second step the excited molecule is ionized, using m photons, where the energy of the m absorbed photons can be higher than the needed energy for ionization. The difference in energy is then mainly carried away by the free electron in form of kinetic energy.
The REMPI scheme in this experiment is an $(n = 3) + (m = 1)$ ionization process, with identical wavelength $\lambda = 303\,\text{nm}$ of all the participating photons. The feasability of photoionization using REMPI in H_2 was demonstrated in 1984 by Pratt et al. [78]. The probability for such a $3 + 1$ photon transition with an intermediate state after the absorption of the first $n = 3$ photons scales as $P \propto I^{n+m}$ if the intensity is below the saturation of the final transition, and scales as $P \propto I^n$ above the saturation of the final transition. Therefore a high intensity and tight focusing are necessary.
The experimental setup to provide light at 303 nm with a high enough intensity follows closely the design described in [78] and is explained

in greater detail in [79]. The setup consists of two commercial lasers, a pulsed, frequency doubled Nd : YAG laser (from Quantel) as a pump laser, and a pulsed dye laser (from Sirah) at 606 nm, which is subsequently also frequency doubled. The Nd : YAG laser produces 5 ns pulses of light at 532 nm with a 20 Hz repetition rate, producing up to 160 mJ per pulse. The output of the frequency doubled Nd : YAG laser is used for optical pumping of the dye, resulting in 16 mJ of red light at 606 nm for the dye laser, and approximately 4 mJ at 303 nm after the frequency doubling.

Nd : YAG **laser**

dye laser

This approach should generate up to 90 % of the H_2^+ ions in the vibrational ground state [80], in which 97 % should populate the rotational state $L = 2$ [79]. This would lead to a population of 87.3 % of the H_2^+ ions in the ro-vibrational state $\nu = 0, L = 2$, which means an improvement of a factor of ≈ 60 compared to the production via electron impact. The experimental verification for that claim is currently carried out.

3.3.2 The Spectroscopy Laser

In order to probe the $(\nu = 0, L = 2) \leftrightarrow (\nu = 1, L = 2)$ two-photon transition in H_2^+ with an accuracy of 10^{-11} or better, one needs a narrow-linewidth, tunable laser source at 9.166 μm. In this wavelength range two laser sources are available: CO_2 lasers and quantum cascade lasers (QCL). While CO_2 lasers exhibit narrow linewidths, extreme stability and high power, the emission lines do not overlap with the transitions in H_2^+ (see Tab. 3.3, after [81]). Furthermore, CO_2 lasers have only a limited tunability of ≈ 100 MHz, such that the transitions of interest in H_2^+ cannot be reached.

H_2^+ transition (ν, J)	CO_2 emission line	$f_{H_2^+} - f_{CO_2}$
$(0,0) \leftrightarrow (1,0)$	9R(52)	−3.08 GHz
$(0,1) \leftrightarrow (1,1)$	9R(48)	4.37 GHz
$(0,2) \leftrightarrow (1,2)$	9R(42)	−1.66 GHz
$(0,3) \leftrightarrow (1,3)$	9R(34)	−13.62 GHz

Table 3.3: *The offset between the transitions of interest in* H_2^+ *and the emission lines of a* CO_2 *laser [81].*

QCLs on the other hand are easily and widely tunable over a range of > 200 GHz, but present a wide free-running linewidth of about 5 MHz. Therefore in 2007 a laser setup was developed by Hilico et al., which combines the spectral properties of the CO_2 laser with the tunability of a QCL [82].

CO_2 **laser**

The CO_2 laser is a 1 m long, single longitudinal-mode laser, where the cavity is closed by a R_{max} mirror at 9.2 μm and a 150 lines/mm grating in the Littrow configuration. Frequency stabilization of the CO_2 laser is done by locking to an intracavity saturated absorption signal

of formic acid (HCOOH). The small gap of 128 MHz between the CO_2 laser and the formic acid line is bridged using a 64 MHz double pass acousto-optic modulator (AOM).

the QCL

The QCL is a 100 mW single-mode distributed-feedback laser from AlpesLaser (SBCW496DN) and is mounted in a cryogenic environment. At 77 K it delivers up to 160 mW and is tunable between 9.16 μm and 9.24 μm, which translates to 32.73 THz and 32.44 THz. The tunabilities are 3 GHz/K and 150 MHz/mA.

phase locking

Subsequently the beatnote between the frequency locked CO_2 laser, operating at the 9R42 emission line, and the QCL is produced and measured at a fast, room-temperature detector. The QCL spectrum is then phase locked to that of the CO_2 laser with a 1.7 GHz frequency offset using an RF synthesizer.
Comparison of the beatnote spectrum of the free-running and the phase-locked QCL with the CO_2 laser shows an efficient reduction of the linewidth of the QCL down to the kHz range, making it suitable for high-precision spectroscopy of H_2^+.

3.3.3 The Dissociation Laser

In order to detect if the excitation of the H_2^+ ions by the spectroscopy laser was successful, the subsequent dissociation by a 213 nm laser is planned. The signal to measure is then the number of H_2^+ ions, since the products H and H^+ will quickly undergo chemical reactions and, being neutral atoms now, will not be trapped anymore. In addition the stability diagram (see Fig. 2.12) for the present trap parameters shows that the high RF amplitude does not allow stable confinement of ions with mass 1 amu.

Nd : YVO_4 laser

The dissociation laser at 213 nm is a commercial laser from Xiton Photonics (model Impress 213). It consists of a pulsed, frequency quintupled 1064 nm Nd : YVO_4 laser, which is pumped by a diode laser, and is delivered within a compact setup. It delivers up to 170 mW of light output at a repetition rate of 12.5 kHz.

frequency quintupling

Internally the working method is the following: First a second harmonic of the Nd : YVO_4 is generated, which then undergoes a sum-frequency generation (SFG) with a part of the original beam to create the third harmonic. Thereafter another SFG is performed with the third and second harmonic, creating the fifth harmonic. All the nonlinear crystals are placed within the commercial laser device, making maintenance of the device in principle not necessary.
The characterization of H_2^+ photodissociation at 213 nm is part of the PhD thesis of N. Sillitoe [32]. There it is shown, that operating the dissociation laser for 2 s results in a dissociation of 74 % of the H_2^+ ions in the vibrational state $\nu = 1$, while only 2 % of the ions in the vibrational state $\nu = 0$ are dissociated.

Chapter 4

Crystallized Ions

This chapter summarizes the first results and demonstrates that all the previously presented parts of the experiment are working as intended. The first two sections contain a short review over the development in the field of Coulomb crystals and what parameter settings led to the first observation of Be^+ crystals in our setup.
The third section discusses the minimization of excess micromotion by exploting the correlation between the fluorescence signal of an ion string and the RF period.
In the fourth section the magnification of the imaging system is obtained by moving a large Coulomb crystal along the $\hat{z}$ axis and comparing the results with results obtained by a SIMION investigation.
The fifth section is dedicated to an analysis of a large, three dimensional Coulomb crystal. The methods presented there allow to estimate the size and number of ions contained in such a crystal. Furthermore, a purity condition is presented, which allows to detect lighter and sympathetically cooled ions along the nodal line of the RF field.
Section six reasons the necessity of sympathetic cooling to cool H_2^+ ions, and furthermore gives a short review of the development of sympathetic cooling. It also presents the first evidence for sympathetic cooling in the setup developed during this thesis.
The seventh section explains how the operation of the trap as a mass spectrometer helped to find evidence for sympathetically cooled H_2^+ ions. Moreover, it presents the observation of a large, presumably purely two dimensional Be^+ crystal of approximately 300 ions. Additionally, the methods from section five are modified and allow to distinguish between two- and three dimensional crystals by exploiting the shape of the fluorescence projections. It also shows how the methods developed in section five allow to locate a single H_2^+ ion in a two dimensional Be^+ crystal of 111 ions. Finally, it presents data for a flat Be^+ crystal with multiple sympathetically cooled H_2^+ ions.
The last section presents a Be^+ crystal with two different sympathetically cooled species, a lighter and a heavier one than Be^+.

4.1 Coulomb Crystals

Confined and charged particles can undergo a phase transition from a disordered, gaseous state to an ordered, (pseudo-)crystalline structure when their potential inter-particle energy exceeds the kinetic energy. These structures were considered first by Wigner in 1934, treating the interaction of electrons in metals [83]. The structures are called Coulomb crystals due to the nature of their dominant interactions. First observations of this phenomena in Paul traps were reported in 1987 by Diedrich et al. [84] and shortly after by Wineland et al. [85]. In both experiments the trap was loaded with atomic ions (Mg^+ in the case of Diedrich, Hg^+ in the case of Wineland), and thereafter Doppler-laser cooled, reducing the kinetic energy of the ions.

crystallization condition

When applying laser cooling, there is a certain point where the ions lost enough kinetic energy E_{kin} such that the potential energy E_{pot} between the trapped particles dominates. In that region the particles form an ordered structure. The condition for crystallization can be expressed by the ratio of the inter-particle potential energy to their kinetic energy,

$$\Gamma = \frac{E_{pot}}{E_{kin}} = \frac{q^2}{4\pi\epsilon_0 a_{WS}\, k_B T}. \tag{4.1}$$

This parameter is also called the plasma-coupling parameter, where a_{WS} is the Wigner-Seitz radius, the radius of the volume element occupied by one ion. Crystallization occurs for $\Gamma \geq 170$ [86]. Together with a value for the Wigner-Seitz radius a lower limit for the temperature of the particles can be given, before crystallization occurs. For $a_{WS} \approx 10\,\mu$m this temperature is approximately 10 mK.

crystal shape

The shape of these Coulomb crystals depends on the trapping potential, as well as on the number of trapped ions. The latter effect was already investigated in the group of Walther in 1992 [87, 88]. With an increasing number of laser cooled Mg^+ ions in a quadrupole storage ring first chains of ions, then zig-zag patterns, helical structures and finally large three dimensional crystals were detected. Depending on the shape of the trapping potential also purely two-dimensional lattices were observed. In linear Paul traps up to 19 Ca^+ ions in a two-dimensional pattern were reported in 2000 [89], while in surface traps more than 150 Sr^+ ions in a purely two dimensional crystal were observed [35].

crystal size

For the purpose of the project at hand large ion crystals are desired, in order to cool as many H_2^+ ions as possible. Simulations for the GBAR project have also shown the necessity of big ion crystals in order to capture and cool injected $\bar{H}^+$ efficiently [32]. In 1998 Drewsen et. al reported the observation of more than 10^5 crystallized Mg^+ in a linear Paul trap [90]. The crystal consisted of up to ten concentric shells

around a linear string of ions in the trap center, demonstrating the feasability of creating large Coulomb crystals in linear traps. In the next section first Coulomb crystals observed during this PhD project are shown.

4.2 First crystallized Be^+ Ions

Testing and assembling of the relevant parts for the creation of Be^+ Coulomb crystals was finished in the spring of 2017. This includes the linear Paul trap and the affiliated voltage supplies (sections 2.2 and 2.3), the Be^+ source (section 2.4), the vacuum setup (section 2.5), the imaging system (section 2.7), the software control (section 2.8) and the laser-cooling system (section 3.2). Subsequently, the search for a fluorescence signal of trapped and laser cooled Be^+ ions was started. Having found first evidence for trapped and cooled Be^+ ions, the parameters were optimized, and a reproducible way to create Be^+ Coulomb crystals was established. The parameters are given in Table 4.1 below.

first parameter set

RF frequency $f = \Omega/2\pi$	13.37 MHz
RF amplitude V_0	518 V
DC voltage endcaps $U_{endc.}$	+9 V
DC voltage center U_{center}	0 V
DC voltage RF electrodes U_0	0 V
current Be-oven	3.1 A
current e-gun	1.49 A
voltage filament e-gun	−145 V
voltage Wehnelt e-gun	−140 V
duration Be-oven and e-gun	30 s
detuning cooling laser start f_{start}	145 MHz
detuning cooling laser stop f_{stop}	15 MHz
power cooling laser	$\approx$ 5 mW
camera temperature	−55 °C
camera gain	50
camera exposure time	0.1 s
vacuum chamber pressure	$\approx 3 \cdot 10^{-10}$ mbar

Table 4.1: *Parameters of the experimental setup to create the first* Be^+ *Coulomb Crystals.*

first crystallizations

At this time no $\boldsymbol{B}$ field was applied, and the repumping was done with the EOM. No crystallization could be directly observed by tuning the frequency between f_{start} and f_{stop}, but crystallization was possible by additional steps concerning the trapping potential. After loading the trap, a first frequency shift from f_{start} of about 30 MHz was applied. Thereafter, the RF amplitude was lowered to $\approx$ 370 V and fast changes

of the trap depth were applied, changing the DC voltages U_{center} at the center electrodes and the RF electrodes U_0 abruptly and simultaneously to $-10\,\mathrm{V}$. After changing a couple of times between the two trap depths and further detuning of the cooling laser towards the final frequency f_{stop}, crystallization took place. A possible explanation for the success of this recipe is as follows: The initial voltage settings of the trap allow confinement of particles with mass $> 9\,\mathrm{amu}$, and the e-gun does not only ionize Be, but also heavier ions from the residual gas like OH^+ or N_2^+. These heavier ones disturb the Be^+ ions enough to prohibit crystallization. The idea of heavier ions being present is further supported by the observation of deformed Coulomb crystals, if crystallization occured. The reduction of the radial confinement by reducing the RF amplitude in combination with the fast change of the DC voltages might create a trapping potential which is not sufficiently attractive for heavier ions, which are therefore lost, and efficient cooling and subsequently crystallization of the Be^+ ions can take place. Figure 4.1 shows the temporal evolution of a Coulomb crystal obtained by this method.

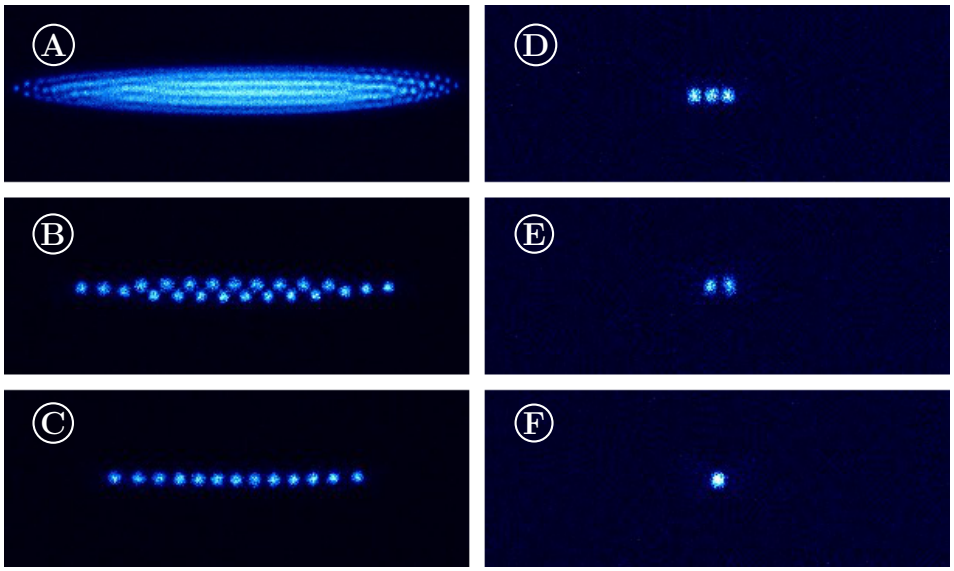

Figure 4.1: *False-color images of first* Be^+ *Coulomb crystals.* Ⓐ *shows the initially created Coulomb crystal with a couple of hundred ions.* Ⓑ *and* Ⓒ *show zoomed in images, and demonstrate the transition from a zig-zag pattern to a string.* Ⓓ, Ⓔ *and* Ⓕ *show a further zoomed in image, and demonstrate the ability to detect single ions. The ion loss is due to collisions with the residual gas.*

First the crystal in Fig. 4.1 Ⓐ was created. After waiting for a couple of minutes (or repeating the alternation between deep and shallow potentials) enough ions were lost to observe the formation of a zig-zag pattern, as shown in Ⓑ. Further loss of ions lead to a string of cold Be^+ ions as seen in Ⓒ, while no manipulations at the trap voltages were carried out. The time difference between the two images is $\approx 80\,\mathrm{s}$. The images Ⓓ - Ⓕ show the decrease from three trapped ions to

only one. The time difference between the shots is $\Delta t_{D\to E} \approx 17\,\mathrm{s}$ and $\Delta t_{E\to F} \approx 120\,\mathrm{s}$. The stability of the crystals depends on the residual gas in the vacuum setup and improves with lower pressure.

4.3 Minimizing the Micromotion

Ions in an ideal linear Paul trap, located at the nodal line of the RF field, do not experience any excess micromotion. However, in real Paul traps phase differences between the frequency at the RF electrodes, and residual DC fields (or geometric asymmetries due to imperfections of the trap) can cause avoidable micromotion. In order to prevent phase differences at the RF electrodes the copper wires for the RF signal were designed to have the same length (see also Fig. 2.17). The effect of residual DC fields was investigated in section 2.2 and is shown in Fig. 2.14. These additional DC voltages displace the ions from the nodal line of the RF field. The effect can be compensated by applying additional DC voltages at the electrodes, in order to shift the minimum of the effective potential back to the nodal line of the RF field.

RF and fluorescence correlation

One method to detect and minimize excess micromotion is by monitoring the correlation between the fluorescence of the ions and the RF frequency [91], since the micromotion is $\propto \cos[\Omega(t-t_0)]$, as can be seen in eq. (2.18). Ions further away from the nodal line of the RF always experience micromotion. To increase the signal-to-noise ratio in the fluorescence signal, a string of ions is analysed. The duration of an RF period is $\approx 75\,\mathrm{ns}$. During this period the overall detection efficiency of the imaging system allows only to detect on average less than one photon, if a string of ≈ 10 ions is investigated. This does not enable a direct investigation of a correlation between the RF frequency and the fluorescence. A solution is to measure the arrival time of the photons with respect to the RF period, and create a histogram of the photon phase with respect to the RF. For the histograms presented in Fig. 4.2, approximately 10 000 arriving photons were used. The data is fitted with $f(t) = A\cos[\Omega t + B] + C$. By applying additional DC voltages to shift the position of the ion string in the $\hat{x}\hat{y}$ plane this correlation can be minimized, which can be measured in a decrease of the value for A in the fit function. Trying multiple positions we end up with a minimum for the correlation by applying $+0.25\,\mathrm{V}$ at electrodes $1, 5, 6$ and 7 and $-0.24\,\mathrm{V}$ at electrodes $5, 6, 7$ and 8. Thereafter, the Coulomb Crystals appear more symmetric and the individual ion spots are sharper, as can be seen for example in Fig. 4.3.

using the crystal shape

Another possibility to minimize the micromotion is to exploit the shape of the crystals detected with the CCD cameras [92]. With the increasing quality of the imaging systems the deformations caused by heavier ions around the Coulomb Crystal can be detected.

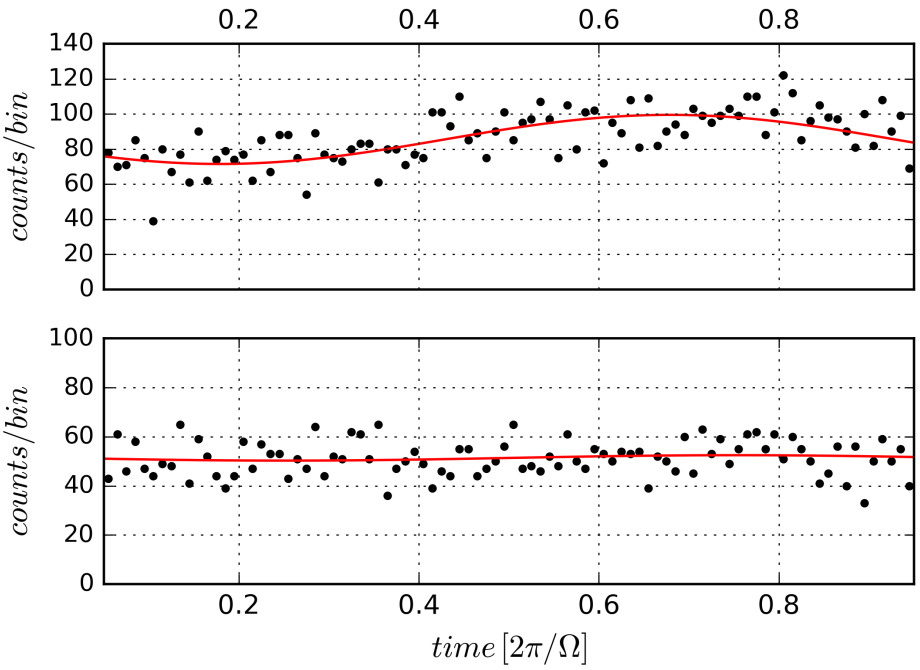

Figure 4.2: *Fluorescence modulation signal of an ion string of approximately* 10 *ions, before (top) and after (bottom) compensation of the excess micromotion.*

By shifting the crystal in the same way as the string before, these deformations change positions. When the deformations appear symmetric, the crystal is positioned symmetrically around the nodal line of the RF field and the excess micromotion is compensated. This technique has the advantage of not only working with a string of ions. In the present experiment the enclosed H_2^+ ions offer a similiar possibility.

4.4 Magnification of the Imaging System

displacement of the trap minimum

Changing the voltage at the two endcap electrodes on one end of the trap displaces the minimum of the potential along the $\hat{z}$ axis, and results in the displacement of an ion crystal. Comparing this effect with the results of a SIMION analysis for the same voltage changes allows to estimate the μm/pixel the CCD cameras detect. The $\hat{z}$ axis is chosen for two reasons: Firstly, a shift along the $\hat{z}$ axis does not increase the micromotion in the crystal. Secondly, since the potential is rather flat in the $\hat{z}$ direction (see section 2.2.2) asymmetric deformations and compressions of the crystal are minimized.

experiment

In a first step, a large Coulomb crystal was created. Larger crystals reduce errors caused by the loss of ions and the accompanied change of the crystal size. The initial DC voltages at the electrodes can be seen in Table 4.2.

electrode	1	2	3	4	5	6	7	8
DC voltages experiment [V]	0.4	9.0	0.0	9.0	9.8	0.8	9.8	0.4
DC voltages SIMION [V]	0.4	9.4	0.4	9.4	9.4	0.4	9.4	0.4

Table 4.2: *The initial values of the DC voltages at the trap electrodes.*

Thereafter, the voltages at the endcap electrodes 2 and 7 were lowered in ten steps of each 0.2 V, resulting in a voltage difference $\Delta U_{endc.}$. The displacement of the crystal was detected with the top camera (see section 2.7) and the results can be seen in Fig. 4.3. This allows to establish a connection between the applied voltage changes and the movement of the crystal center in units of pixel/V.

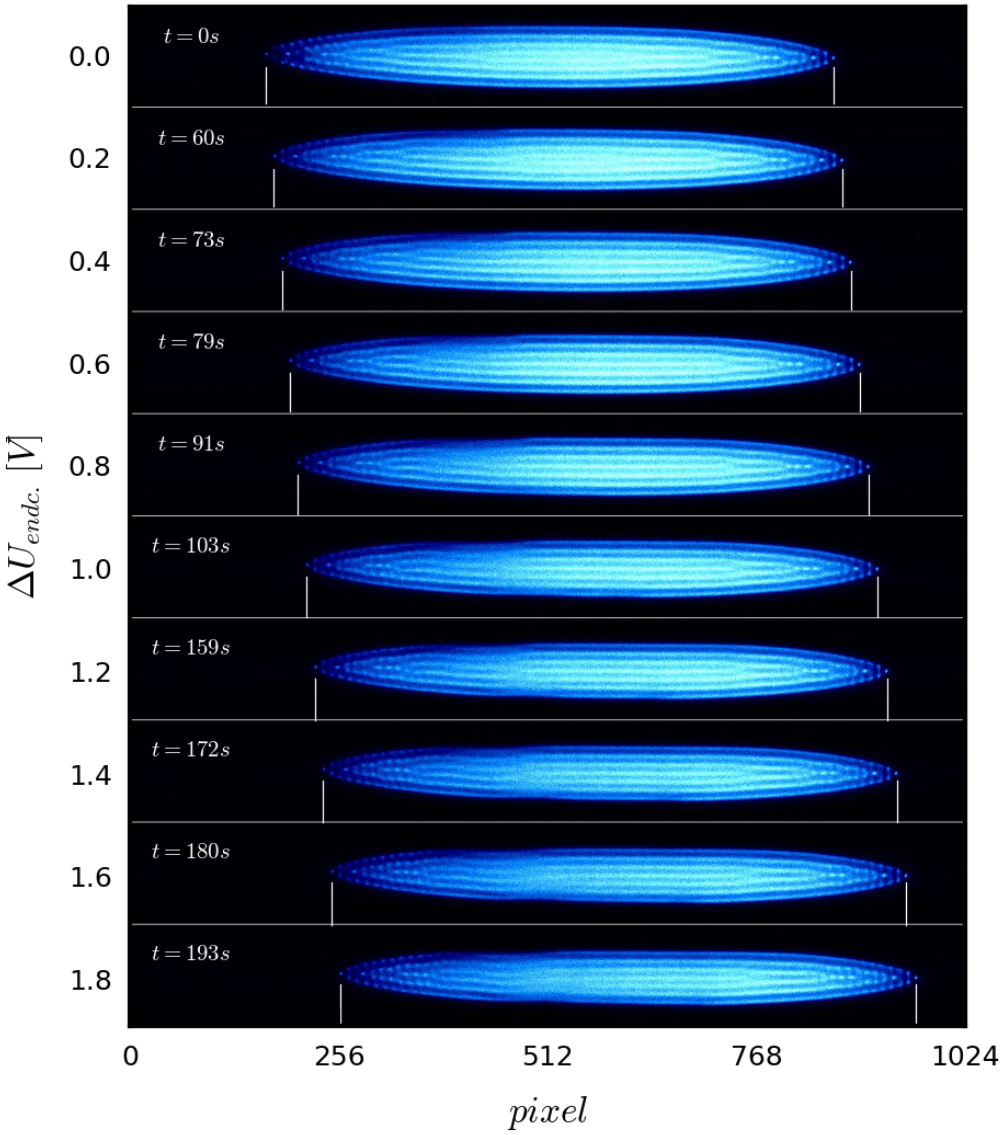

Figure 4.3: *Displacement of an ion crystal along the $\hat{z}$ axis, depending on the voltage difference $\Delta U_{endc.}$ between the endcaps.*

SIMION

Taking a look at Tab. 4.2, one can see that in an ideal trap these DC voltages would not create a symmetric potential, but are chosen to compensate for the micromotion. For the SIMION analysis, symmetric voltages need to be used, being as close as possible to the experimental case (see also Table 4.2). The RF amplitude and frequency are in both cases the same, 512 V and 13.37 MHz. After setting up the effective potential (see subsection 2.2.3) for each of the ten voltage configurations the position of the potential minimum is determined. Figure 4.4 shows the comparison between the experimental data and the SIMION results for the evolution of the crystal center and the potential minimum. Fitting both sets of data points results in 53.2 ± 1.1 pixel/Volt and $106.3 \pm 4.3\,\mu$m/Volt, so that we finally obtain a value of $1.997 \pm 0.091\,\mu$m/pixel for the top camera.

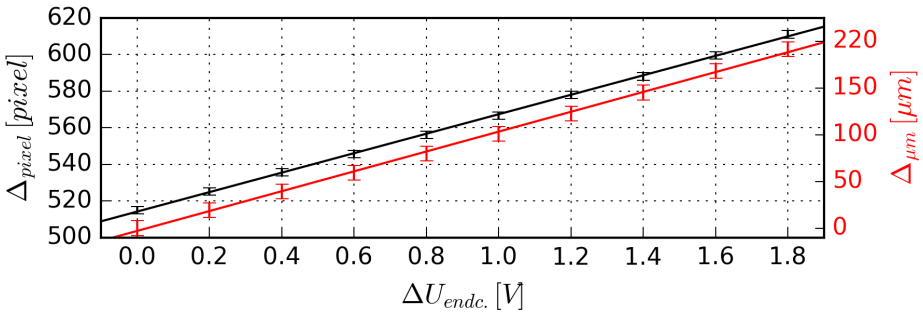

Figure 4.4: *Displacement of an ion crystal depending on the voltage difference $\Delta U_{endc.}$ at the endcaps. The top points (and left axis) show the experimental data and the bottom data points (and right axis) show the SIMION results. Both data sets were fitted with a linear function.*

Having obtained this value allows now for an estimation of the absolute crystal sizes and the spacing between the ions, which is with $\approx 20\,\mu$m comparable to results found elsewhere (for example [90, 86, 93, 94]). This allows to cross-check the plausibility of the SIMION results.

magnification

In order to determine the μm/pixel value for the second camera, an identical crystal is observed with both cameras, resulting in a value of $\approx 1.68\,\mu$m/pixel for the second camera. One can note that the $1024 \times 1024\,\text{pixel}^2$ of the top camera depict an area of $2.06 \times 2.06\,\text{mm}^2$, while the side camera with a CCD chip of $512 \times 512\,\text{pixel}^2$ depicts an area of $0.86 \times 0.86\,\text{mm}^2$. Since the edge length of the pixels on both cameras is known (see section 2.7) the magnification for the top camera can be determined by dividing the size of a pixel through the value obtained above for the μm/pixel, leading to a magnification of 6.51 ± 0.30. The magnification for the side camera is ≈ 9.5. The magnification of the top camera can also be estimated using the lensemaker's equation. The distance between the trap center and the center of the objective (see Fig. 2.29) is estimated by $p_1 = 87.2 \pm 10\,\text{mm}$ and the distance between the center of the objective and the CCD chip by $p_2 = 555 \pm 20\,\text{mm}$,

resulting in a magnification of 6.4 ± 0.6. While both methods agree with each other, the uncertainty of the first method is smaller.

4.5 Three-dimensional Be^+ Crystals

Two principal reasons to obtain large Coulomb Crystals can be recalled. The first is to be able to sympathetically cool as many H_2^+ ions as possible to increase the signal-to-noise ratio for the H_2^+ spectroscopy experiment. The second one is in regard of externally produced ions, where bigger crystals mean faster cooling of the injected ions. This is for example the case in the GBAR project, where the $\bar{H}^+$ ion will be injected with a kinetic energy of approximately 1 eV (see thesis of N. Sillitoe [32]).

second parameter set

The trap, laser, and camera parameters are the same as in section 4.2 and are shown in Table 4.1, but include compensated micromotion and the exposure time of the cameras is five times larger than before, now equalling to 0.5 s.

number of ions

Two approaches are taken to estimate the amount of Be^+ ions in a crystal; both are based on the fluorescence images recorded with the CCD cameras, and the crystal shown in Figure 4.5 will serve as an example. The bottom left panel shows the data recorded with the top camera, after it was imported into Python and a threshold for the fluorescence signal was applied. This removes noise due to dark current and reflections. Pictured above and right to the image are the projections of the fluorescence signal along the radial direction and the $\hat{z}$ direction.

volume method

The first option to evaluate the amount of crystallized ions is by determining the volume occupied by a single Be^+ ion, and the volume of the Coulomb crystal. The zoomed inset of Fig. 4.5 shows six equally spaced Be^+ ions along the $\hat{z}$ axis, which allow to estimate the Wigner-Seitz radius at $a_{WS} \approx 12.5 \pm 0.3\,\mu$m. The total crystal length l_z along the $\hat{z}$ axis is approximately $1128 \pm 5\,\mu$m and the width w_r is $136 \pm 5\,\mu$m, assuming the crystal to be symmetric in the radial direction. Therefore, the total volume can be estimated as the volume of an ellipsoid with $V = {}^4\!/_3\,\pi \cdot {}^{l_z}\!/_2 \cdot ({}^{w_r}\!/_2)^2$. By dividing the total volume by the volume of a sphere with the Wigner-Seitz radius one ends up with 1374 ± 193 beryllium ions. However, this method allows only to analyze single-component crystals, since it is difficult to estimate defects in form of enclosed sympathetically cooled ions (see section 4.6).

fluorescence method

The second method is by numerically integrating the fluorescence signal in a flat region of the crystal, where the number of ions can be counted. In Fig. 4.5 such regions are at both ends of the crystal in the $\hat{z}$ direction. The number of ions in both end regions is estimated as seven, eight or nine ions, since it is not obvious if below the ions closer to the center of the crystal additional ions are hidden. The parts of the fluorescence signal in the $\hat{z}$-projection which are associated with

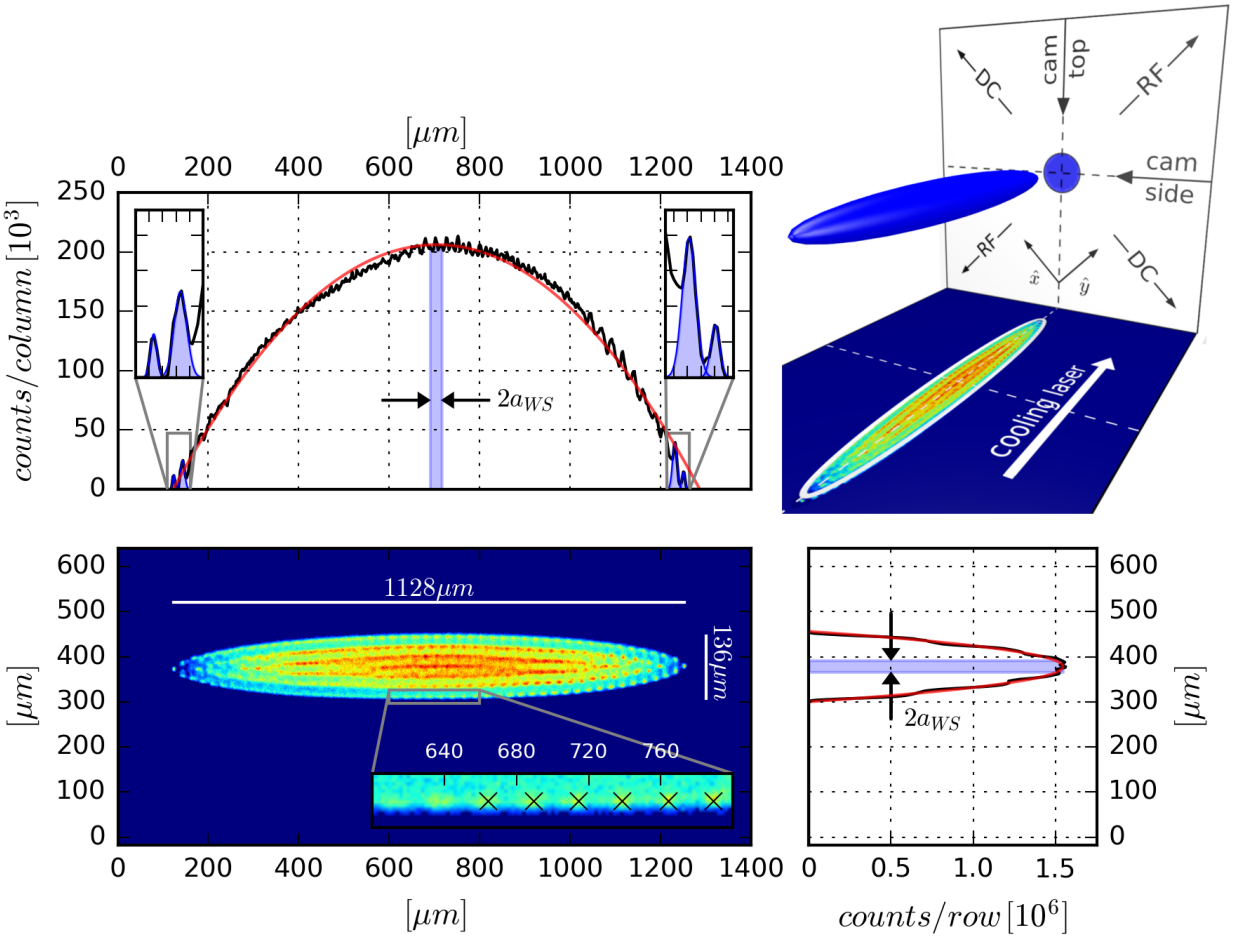

Figure 4.5: *A Coulomb Crystal of* $\approx$ 1350 Be^+ *ions. The bottom left shows the data obtained with the top camera. The inset shows eight uniformly spaced ions with marked positions for six of them. Above and right to the data of the camera the projections along the columns and rows are shown, together with quadratic fits (see text). The marked regions around the crystal center show the integration interval to determine the number of ions in the corresponding slices. The insets in the top projection shows Gaussian fits for ions at the end of the crystal. The top right image shows the position of the RF and DC electrodes with respect to the crystal, the direction of the cooling laser and the positions of the cameras.*

these two regions are shown in the inset of the plot. By fitting the peaks of the fluorescence with a Gaussian, and subsequently integrating, a value for the fluorescence caused by these ions is obtained. The integral associated with the single ion at the outer right has a value of $\approx 61 \cdot 10^3$ counts. Based on the linewidth of the transition and the exposure time one expects $\approx 10^7$ photons/ion. Considering the overall collection efficiency of the imaging system one ends up with $\approx 60 \cdot 10^3$ photons/ion, which fits well with the measured value. The ratio of the integrals with respect to each other allows to validate the number of ions identified with the integrals. This method has the ad-

vantage of also allowing to determine the number of ions if the crystal is not symmetric in the radial direction. Note, however, that it is important that all the ions in the crystal receive the same amount of cooling light, or the transitions are saturated. In the current configuration of the setup the waist of the cooling beam is larger than all the observed ion clouds. The results for different assumed numbers of ions are listed in the table below and compare well with the result of the first method.

method	number of ions
volume method, spherical ion volume	1374 ± 193
fluorescence method, 8 ± 1 ions	1311 ± 164

Table 4.3: *The number of ions in the crystal shown in Fig. 4.5, obtained by the two different methods.*

fitting the fluorescence

In order to gain more insight into the information contained in the projections of the fluorescence, the shape of the projections is further investigated. Assuming the Be^+ ions within the crystal to be uniformly distributed, the projection of the fluorescence signal is proportional to the cut surfaces of the ellipsoid along the projection directions.

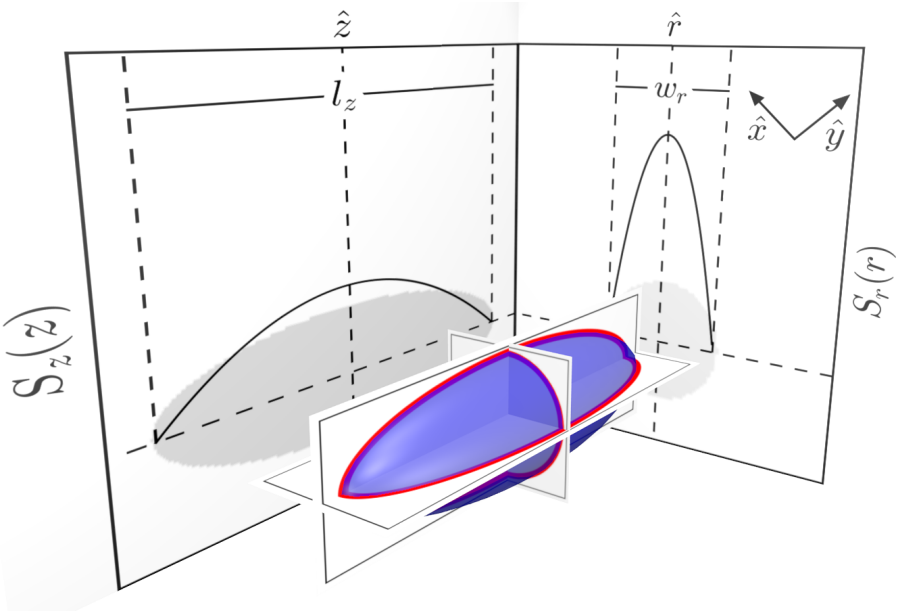

Figure 4.6: *Sketch of an ellipsoid with its cut surfaces through the center (r_0, z_0). The cut surface S_z is parallel to the $\hat{x}\hat{y}$ plane and the cut surface S_r is perpendicular to S_z. The functions for the cut surfaces along the $\hat{z}$ and $\hat{r}$ axis are also plotted.*

fit along the $\hat{z}$ axis

For a crystal which is symmetric along the radial direction the cut surface perpendicular to the $\hat{z}$ axis of the crystal is a circle, as can be seen in Fig. 4.6. The radius of this circle is depending on the

$\hat{z}$ coordinate and follows the elliptical shape of the crystal. The cut surface is therefore

$$S_z(z) = \pi \cdot \frac{w_r^2}{l_z^2} \cdot \left[(l_z/2)^2 - (z - z_0)^2 \right], \tag{4.2}$$

fit along the $\hat{r}$ axis

with the dimensions l_z and w_r, and z_0 being the center of the crystal. The cut surface perpendicular to the $\hat{r}$ axis has the shape of an ellipse with the major axis being the extension along the $\hat{z}$ axis and the minor axis being the extension along the $\hat{x}$ and $\hat{y}$ axis. While the minor axis evolves like a circle when the cut surface is displaced along the $\hat{x}$ or $\hat{y}$ axis, the major axis itself evolves like an ellipse. The cut surface perpendicular to the $\hat{x}$ and $\hat{y}$ axes is therefore

$$S_r(r) = \pi \cdot \frac{l_z}{w_r} \cdot \left[(w_r/2)^2 - (r - r_0)^2 \right], \tag{4.3}$$

with r_0 being the center of the crystal along the $\hat{r}$ axis. The resulting fits can be seen as solid curves in the fluorescence projections of Fig. 4.5 and are in good accordance with the data.

number of ions in crystal slices

To obtain the number of ions in such a cut surface one has to take into account the finite width of the space occupied by the ions. This width can be estimated using the Wigner-Seitz radius a_{WS} and one can write for the integrated count number N_{count}

$$N_{count} = \int_{\widetilde{u}-a_{WS}}^{\widetilde{u}+a_{WS}} C_u(u)\mathrm{d}u = n_u\, \bar{c} \int_{\widetilde{u}-a_{WS}}^{\widetilde{u}+a_{WS}} S_u(u)\mathrm{d}u, \tag{4.4}$$

where C_u is the projection of the detected fluorescence count signal, n_u the ion density in the volume element spanned by $\widetilde{u} \pm a_{WS}$, $\bar{c}$ the average fluorescence count signal per ion and $u = r, z$. For $\widetilde{u}$ close to the center of the crystal, where S_u does not change too strong over a distance of $2a_{WS}$, the right side of the equation above can be approximated as $n_u\, \bar{c}\, S_u(\widetilde{u}) \cdot 2a_{WS}$, so that one can write for the number of ions in the investigated volume element

$$N_{ions} = \frac{1}{\bar{c}} \int_{\widetilde{u}-a_{WS}}^{\widetilde{u}+a_{WS}} C_u(u)\mathrm{d}u. \tag{4.5}$$

For the two slices around the center (r_0, z_0) of the crystal shown in Fig. 4.5, this results in 43 ions in the slice around $S_z(z_0)$ and 328 ions

in the slice around $S_r(r_0)$.

purity condition

Assuming a highly ordered structure of the ions in the cut surfaces, having the same ion density n_u, the same average fluorescence signal $\bar{c}$ and Wigner-Seitz radius a_{WS}, the ratio of the integrated count numbers $C_r(r)$ and $C_z(z)$ is equal to the ratio of the projected surfaces:

$$r_S(r,z) := \frac{S_r(r)}{S_z(z)} = \frac{C_r(r)}{C_z(z)} =: r_C(r,z). \tag{4.6}$$

This condition indicates how well the assumption of a uniform Be^+ distribution in the cut surfaces is justified. It breaks down if either one of the assumptions above is violated and for crystals containing impurities like sympathetically cooled ions, which are not contributing to the fluorescence signal.
For the cut surfaces through the crystal center and using eq. (4.2) and eq. (4.3) this condition simplifies to

$$r_S(r_0,z_0) = \frac{l_z}{w_r} = \frac{C_r(r_0)}{C_z(z_0)} = r_C(r_0,z_0). \tag{4.7}$$

Using the crystal dimensions and count maxima obtained by the fits for the crystal in Fig. 4.5 one obtains $r_S(r_0,z_0) = 7.45 \pm 0.20$ and $r_C(r_0,z_0) = 7.50$, which indicates no enclosed, sympathetically cooled ions in the corresponding slices.

smaller crystals

As mentioned before, this method only works under certain conditions, but can be useful to detect $\bar{H}^+$ ions in large Be^+ crystals. It is difficult to estimate down to which number of ions these considerations stay true. In Fig. 4.7 a smaller Be^+ crystal is analysed. The same methods as before are applied, and the image detected with the top camera is shown at the bottom left of Fig. 4.7. The projections of the fluorescence signal along the $\hat{z}$ and $\hat{r}$ axis are again above and right to the image. The number of ions estimated with the two methods presented in before are shown in Table 4.4.

method	number of ions
volume method, spherical ion volume	509 ± 89
fluorescence method, 8 ± 1 ions	457 ± 57

Table 4.4: *The number of ions in the crystal shown in Fig. 4.7, obtained by the two different methods.*

The fluorescence projections are fitted as described above and are in good accordance with the data. For the number of ions in the slices around the trap center, one obtains 27 ions for $S_z(z_0)$ and 148 for $S_r(r_0)$.

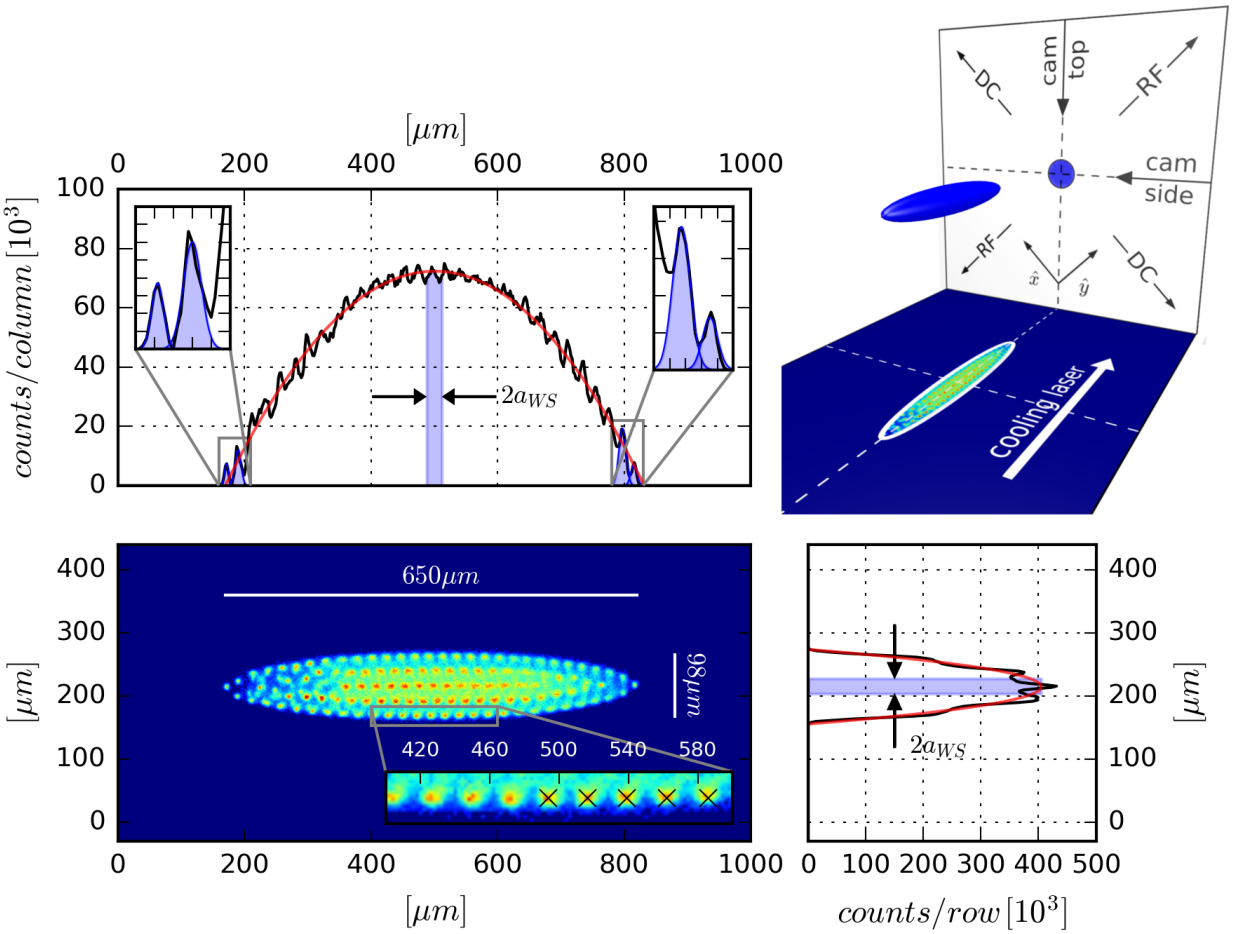

Figure 4.7: *A symmetric* Be^+ *crystal with approximately* 480 *ions. Further explanations can be found in the caption of Fig. 4.5*

The two ratios from eq. (4.7) match with $r_S(r_0, z_0) = 5.60 \pm 0.18$ and $r_C(r_0, z_0) = 5.59$. Despite the fact that the disordered area at the left of the crystal suggests some enclosed, sympathetically cooled ion(s), the fluorescence projection along the $\hat{z}$ axis and the two matching ratios r_S and r_C do not support that assumption.
For both examples the estimation of the ion number for the two different methods agree within their errors and can serve as a rough estimation. A technique which allows for a more precise estimation can be found here [95] and relies on the ion cloud being in a so called cold fluid state. This technique is more demanding and is not discussed here.

4.6 Sympathetic Cooling

Doppler laser cooling is restricted to atoms and ions with a suitable, closed transition. The complex energy structure of molecular ions makes it difficult to tailor cooling schemes and would need many dif-

ferent repumpers to close the transitions. In addition, homonuclear molecules (in their ground state) do not possess permanent electric dipole moments, such that the selection rules prohibit one-photon transitions. Another problem can be the non-availability of laser sources at the required wavelength. Finally, as is the case e.g. for the antimatter $\bar{H}^+$ ions in the GBAR project, the ion of interest may have only one bound state, such that direct laser cooling is not possible at all.

A convenient solution to these difficulties can be sympathetic cooling. This allows to cool down particles which cannot be directly adressed, like in our case the homonuclear molecular hydrogen ion H_2^+. Particles with an easy cooling transition are trapped together with the particles of interest, and due to the long range Coulomb interaction between the ions cooling of one species leads to cooling of the other species.

atomic ions

The first time sympathetic cooling was proposed was in 1978 by D. Wineland et al. [58] and it was shown to work in a Penning trap with laser cooled $^{24}Mg^+$ ions and its sympathetically cooled isotopes $^{25}Mg^+$ and $^{26}Mg^+$ [96]. In 1986, Larson et al. reported sympathetic cooling of $^{198}Hg^+$ by Doppler cooling of $^{9}Be^+$ in a Penning trap, showing that sympathetic cooling is also applicable to two ion species with a mass ratio of $m_{coolant}/m_{cooled} = 22/1$ [97].

The first evidence for sympathetic cooling in RF traps was observed in 1992 [88]. While investigating the ordered structures of trapped and cooled $^{24}Mg^+$ ions, dark spots in the crystal-like structures could be seen, and were identified as representatives of the two other magnesium isotopes and/or other ions originating from the residual gas.

molecular ions

Nearly twenty years after the proposal of Wineland et al., first sympathetic cooling of molecular ions was reported [98]. Laser-cooled $^{24}Mg^+$ ions were used as a coolant species in a linear Paul trap, and by controlled introduction of air into the vacuum chamber, and proton transfer to the neutral molecules, sympathetically cooled molecular ions could be observed. The way of detection also presented a novelty - by excitation of the secular frequencies of the trapped molecular ions, the $^{24}Mg^+$ were heated as well and therefore the measured fluorescence decreased.

limits of sympathetic cooling

While in the publications mentioned before the number of coolant ions was larger than the amount of cooled ions, Drewsen et al. reported in 1999 sympathetic cooling of up to 15 ions by one laser-cooled ion, and for larger ion crystals a ratio of more than 50% for the number of sympathetically cooled ions to coolant ions [93]. Molecular dynamics simulations helped to understand the range of mass ratios $m_{coolant}/m_{cooled}$ for which sympathetic cooling is applicable [99, 100]. As a result of these simulations it was shown, that the two coolant species $^{9}Be^+$ and $^{137}Ba^+$ are sufficient to acchieve sympathetic crystallization for molecules with a single positive charge and a mass ranging from 2 amu to 2000 amu.

In our setup, first evidence for sympathetic cooling was found by observing beryllium ion strings in a symmetric trap configuration. In

this configuration the a_i parameter of the trap is close to zero. Since the ions are on a string there is no radial separation between heavier and lighter ions, and since the trap potential along the $\hat{z}$ axis is flat one can not jump to the conclusion which masses are trapped within the string. It can be ions heavier or lighter than Be^+.

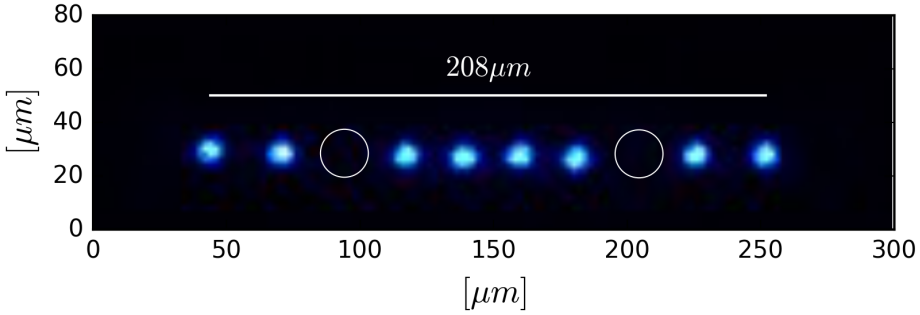

Figure 4.8: *An ion string of eight laser cooled beryllium ions with two sympathetically cooled ions, indicated by the empty circles.*

4.7 Flat Be^+ Crystals and sympathetically cooled H_2^+ Ions

During the loading of the trap with beryllium ions by electron impact, the e-gun ionizes also other particles in the residual gas. In well-baked chambers the main components found in the residual gas are H_2, H_2O and OH, N_2, as well as CO and CO_2 [101]. Except for the hydrogen molecule all these molecules are heavier than Be^+, with OH as the lightest having a mass of 17 amu. If ionized, these heavier molecules gather around the Be^+ and make it more difficult to cool the Be^+ ions down to crystallization, and, additionally, disturb the crystal shape if crystallization is successful.

trap as mass spectrometer

To overcame this obstacle one can operate the trap in a parameter region where the trapping conditions are not stable for heavier ions. Figure 4.9 shows the parameter space which can be reached with the setup described in section 2.3, and the areas of stability according to the Mathieu equations are shown. By keeping a certain value for the amplitude of the RF voltage and increasing the DC voltage U_0, the trapping potential becomes step by step unstable for particles with different masses, starting with the heavier ones. At an RF amplitude of $V_0 \approx 500\,\mathrm{V}$ the DC voltage needs to be approximately 15 V in order to create a trapping potential which is only stable for Be^+ or lighter ions. Real mass spectrometers are working by changing V_0 and U_0 simultaneously, but with a fixed ratio to each other, such that the trapping potential is only stable for one distinct species at a time (see Fig. 2.12 and text there).

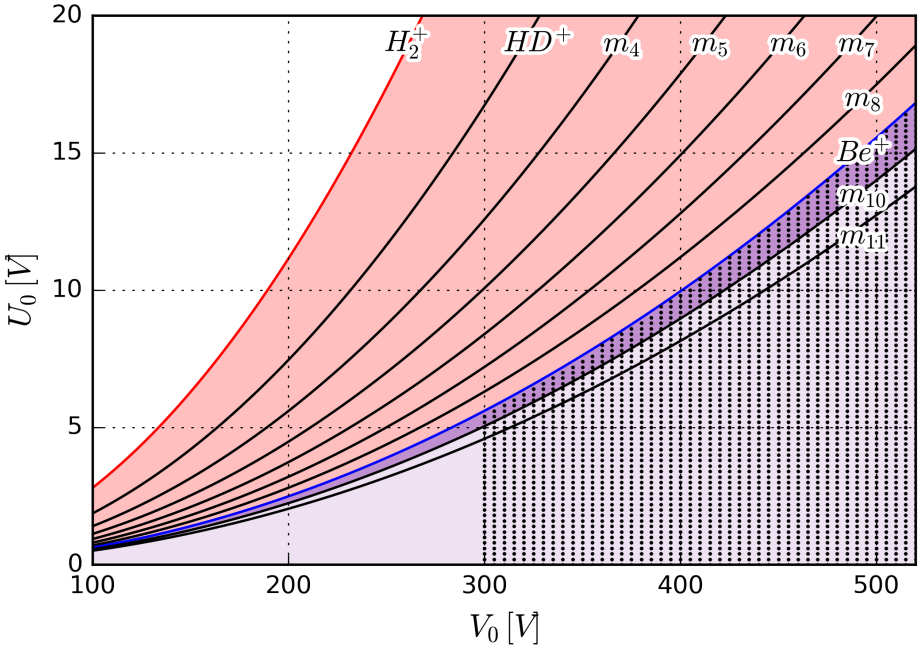

Figure 4.9: *The stability diagram for particles with different masses in the parameter region which is accessible with the trap voltages. The dotted area shows the results for a SIMION analysis with an endcap voltage of* 2 V.

The manipulation of only the DC voltage U_0 allows to confine simultaneously ions with a mass smaller than a certain value.

Mathieu vs SIMION

The dotted area in Fig. 4.9 shows the results for a SIMION analysis for the trap in this setup. Unlike the Mathieu stability condition, such a simulation can also take the endcap voltage U_{endc} into acount. For the present case, U_{endc} was kept constant at 2 V, and although the endcap voltages cause a deconfining potential in the $\hat{x}\hat{y}$ plane, here this effect is negligible for small endcap voltages.

One can summarize that another option (instead of using the recipe described in section 4.2) to drive out impurities of the trapped ion cloud is either to load beryllium ions in a symmetric trap configuration ($a_u = 0$) and then clean the cloud by changing the DC voltages such that heavier particles become unstable, or by loading the trap directly in that constellation. The former leads, if done too fast, to ion loss, while the latter reduces the number of initially trapped Be^+ ions.

secular frequency excitation

Another method for removing heavier ions from the trap is by excitation of the corresponding secular frequencies. This method is not yet fully functional in our setup, but should allow to load in a symmetric trap configuration and result therefore in more trapped Be^+ ions, and finally in larger Coulomb crystals.

4.7.1 A two-dimensional Be^+ Crystal

From Fig. 4.9 one can see that at an RF amplitude of ≈ 500 V (and a frequency of 13.337 MHz) confining only ions with a mass of 9 amu or lighter a U_0 of ≈ 14.5 V needs to be applied. Since the voltage range at the DC electrodes is between ±10 V (see section 2.3.2) the ground at the center electrodes 3 and 6 needs to be shifted to negative voltages. The resulting DC trap voltages are shown in Table 4.5. The deviations are due to the compensation of the micromotion.

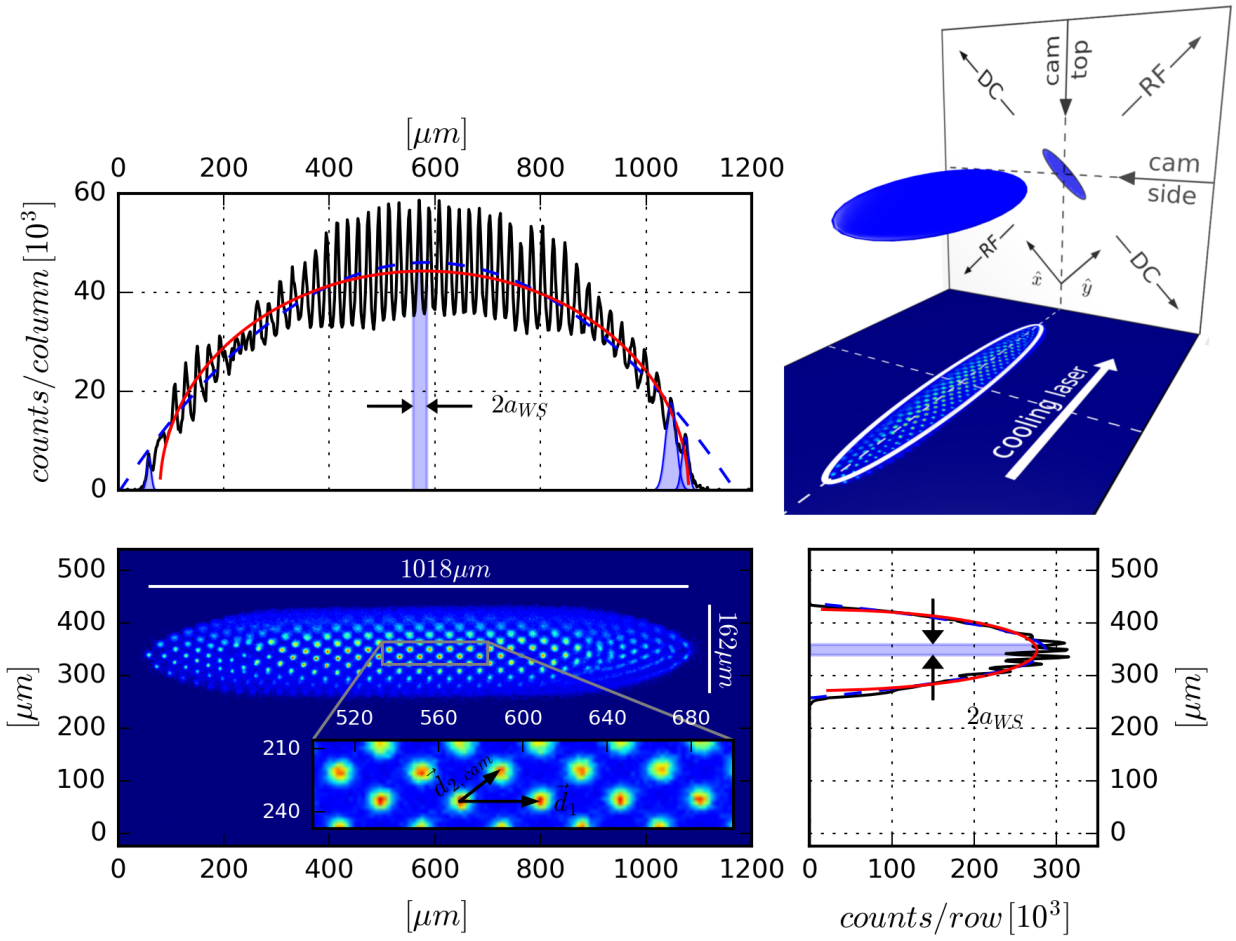

Figure 4.10: *A two-dimensional* Be^+ *crystal, consisting of approximately* 300 *ions. The inset of the bottom left image shows the highly ordered structure of the ions in the crystal center of a centered square lattice. The two arrows show the primitive lattice vectors. To obtain the ion number in the crystal the fluorescence signal of the countable ions was fitted with a Gaussian. The dashed lines in the projections of the fluorescence is the quadratic fit as explained in section 4.5. The solid lines show an ellipse (see text). In both fluorescence projections the marked area shows the integration interval for the determination of the ion number in the corresponding slices. The orientation of the two-dimensional crystal with respect to the trap electrodes and cameras is shown at the top right.*

electrode	1	2	3	4	5	6	7	8
DC voltages [V]	8.52	−4.00	−6.00	−4.00	−3.08	−5.08	−3.08	8.40

Table 4.5: *The DC voltages at the trap electrodes with* $U_{endc} = 2\,\mathrm{V}$ *and* $U_0 = 14.4\,\mathrm{V}$. *The deviations at electrodes* 1, 5, 6 *and* 7 *are due to the compensation of micromotion.*

The parameters for Be^+ creation and the cooling laser are the same as in Table 4.1 and the exposure time for the camera is 0.5 s. The detected image is shown at the bottom left of Fig. 4.10, with the projections of the fluorescence signal above and to the right.

volume method ↓ surface method

For the crystals analysed before, an ellipsoid shape was assumed. Since for asymmetric potentials one can expect the crystal to be shallow along the $\hat{y}$ axis, the volume method to obtain the number of ions must be modified. The crystal shape is assumed to be an ellipsoid with a thickness of one Be^+ ion, such that the volume method becomes a surface method. The number of ions is now estimated by dividing the total surface $S = \pi \cdot w_x \cdot l_z$ through a circle defined by the Wigner-Seitz radius. For a symmetric crystal the width w_r of the ellipsoid is not influenced by any projection effects. For an asymmetric crystal, located as can be seen at the top right of Fig. 4.10, the width w_{cam} detected with the cameras needs to be corrected. The expected angle of 45 ° between the crystal extension in $\hat{x}$ direction and the imaging direction leads to a width of $w_x = \sqrt{2} \cdot w_{cam}$. The number of Be^+ ions estimated with this method can be seen in Table 4.6 and compares well to the estimation done by the fluorescence method.

method	number of ions
surface method, circular ion surface	339 ± 16
fluorescence method, 6 ± 1 ions	308 ± 51

Table 4.6: *The number of ions in the crystal shown in Fig. 4.10, obtained by the two different methods.*

fitting the fluorescence

Since the shape of the crystal is described by an ellipse rather than by an ellipsoid, the assumptions in section 4.5 leading to the fit function are not valid anymore. This can also be seen in the fluorescence projections of Fig. 4.10, where the dashed lines show a fit with the functions from eq. (4.2) and (4.3). The overlap is particularly poor at the borders of the signal. However, the projected fluorescence signal is still proportional to the number of ions in each cut along the axes. Along the $\hat{z}$ axis the projected fluorescence for such a two-dimensional crystal is therefore proportional to

$$f_z = \pi \cdot \frac{w_x}{l_z} \cdot \sqrt{(l_z/2)^2 - (z - z_0)^2}, \tag{4.8}$$

with z_0 being the center of the crystal. The same expression holds for the fit along the $\hat{r}$ axis, but with the roles of l_z and w_x exchanged. By not taking the outermost data points into account, the data can be fitted with these functions. The solid lines in the fluorescence-projections in Fig. 4.10 shows these fits, which match particularly at the borders better with the data. This indicates that the shape of the crystal is indeed better described by a two-dimensional ellipse than by an ellipsoid.

lattice structure

Additional support for the two-dimensional character of the crystal can be found by analysing the nature of the lattice structure of the crystal. The inset in the camera data of Fig. 4.10 shows the pseudo-lattice structure of the crystal. Infinite lattices are described by their primitive vectors, which generate the complete lattice structure by discrete translations. For the crystal in question, this is only valid at the center, since the shape of the potential causes deformations at the crystal borders. In radial direction the crystal-like pattern is preserved until the boundaries of the crystal, but in $\hat{z}$ direction the ordering changes. However, close to the center one can find two primitive vectors, which are shown in the inset of Fig. 4.10. The vector $\boldsymbol{d}_1$ along the $\hat{z}$ axis has a length of $38.2 \pm 0.9\,\mu$m, while the vector $\boldsymbol{d}_{2,cam}$ has a length of $23.6 \pm 1.2\,\mu$m. The angle θ_{cam} between the two vectors is $36.1 \pm 0.6\,^\circ$. Assuming a two-dimensional crystal, located with respect to the camera axis as shown at the top right of Fig. 4.10, the value for $\boldsymbol{d}_{2,cam}$ has to be corrected. This leads to $|\boldsymbol{d}_2| = 27.4 \pm 1.8\,\mu$m and $\theta = 45.9 \pm 1.8\,^\circ$. That suggests the assumption that the structure in the center of the crystal is a centered square lattice, since for $|\boldsymbol{d}_{1,sl}| = 38.2\,\mu$m this lattice is described by $|\boldsymbol{d}_{2,sl}| = 27.0\,\mu$m and $\theta_{sl} = 45\,^\circ$, which matches well with the determined values. The observation of this two-dimensional lattice structure further supports a purely two-dimensional crystal. The Wigner-Seitz radius is therefore estimated at $|\boldsymbol{d}_2|/2 = 13.7 \pm 0.9\,\mu$m.

number of ions in slices

The change in the fluorescence of the ions in radial direction and the change of the ordering along the $\hat{z}$ axis makes it difficult to estimate the amount of ions in the slices. While the former leads to an overestimation of the ions in the slice projected onto the $\hat{z}$ axis, the latter distorts additionally the number of ions in the slice along the $\hat{z}$ axis.

4.7.2 A single H_2^+ ion in a two-dimensional Be^+ Crystal

loading of H_2^+

To add H_2^+ ions into a crystal like the one in Fig. 4.10 the e-gun can be used to ionize H_2 from the residual gas. Since the trap parameters do not allow confinement of heavier ions than Be^+ the crystal is not disturbed by the creation of heavier ions, and the H_2^+ ions accumulate in the crystal. Fig. 4.11 shows a two-dimensional Be^+ crystal with

one sympathetically cooled H_2^+ ion on the left. The trap parameters are the same as in Table 4.5 and the e-gun was turned on for 15 s.

number of ions

The number of ions obtained by the different methods is shown in Table 4.8, together with the number by directly counting the ions. The discrepancy can be explained by the fact that due to the small size of the crystal the actual shape is not an ellipse, and the Wigner-Seitz radius is not constant. The accuracy of the fluorescence method is biased by the varying fluorescence per ion.

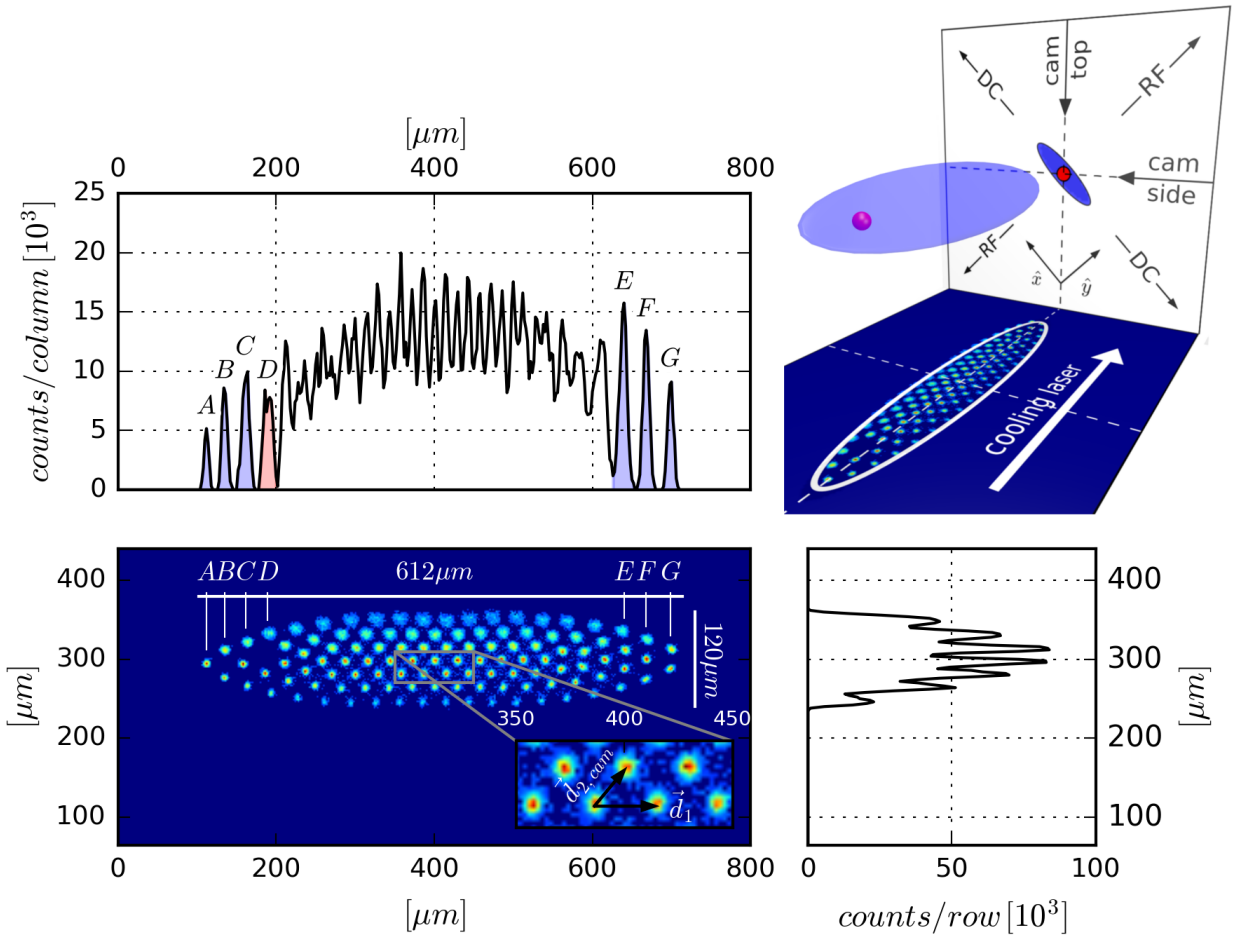

Figure 4.11: *A two-dimensional crystal with* 111 Be^+ *ions and one* H_2^+ *ion, located at the left side of the crystal. The inset of the bottom left image shows a hexagonal lattice structure in the center of the crystal with the two primitive lattice vectors. The outer peaks in the projection of the fluorescence along the* $\hat{z}$ *axis can be identified with the ions along the corresponding columns in the image of the camera data. The numerical integration of the peak D gives nearly the same result as for C and F and allows to identify the position of the* H_2^+ *ion along the* $\hat{z}$ *axis. The seven peaks in the plot at the bottom right can be identified with the seven rows of ions in the camera data.*

method	number of ions
surface method, circular ion surface	126 ± 17
fluorescence method, 18 ± 1 ions	137 ± 8
counting	111

Table 4.7: *The number of ions in the crystal shown in Fig. 4.11, obtained by the two different methods, and by direct counting.*

lattice structure

The inset in the image at the bottom left of Fig. 4.11 shows two primitive lattice vectors for the crystal structure in the center. For these vectors one obtains a length of $|\boldsymbol{d}_1| = 28.2 \pm 1.9\,\mu$m and $|\boldsymbol{d}_{2,cam}| = 22.4 \pm 0.7\,\mu$m, while the angle in between has a value of $\theta_{cam} = 51.1 \pm 4.7\,^\circ$. After correcting these values for the angle in between the camera axis and the $\hat{x}$ axis one obtains $|\boldsymbol{d}_2| = 28.4 \pm 5.3\,\mu$m and $\theta = 60.3 \pm 3.3\,^\circ$. These results match well with the values expected for a hexagonal lattice with $|\boldsymbol{d}_{2,hl}| = |\boldsymbol{d}_{1,hl}| = 28.2\,\mu$m and $\theta_{hl} = 60.0\,^\circ$.

detection of the H_2^+

Sympathetically cooled ions do not contribute to the fluorescence signal, which can be seen at the empty spot in the camera data in Fig. 4.11. At the borders of the crystal in $\hat{z}$ direction the Be^+ ions are well aligned along the $\hat{r}$ axis, and one can identify separated columns. In Table 4.8 the ratios of the numerically obtained integrals for the different columns are shown.

column	A	B	C	D	E	F	G
number of ions	1	2	3	3	4	3	2
integral in units of integral A	1.00	2.04	3.03	3.19	5.04	3.59	2.30
expected	1	2	3	3	4	3	2
integral in units of integral G	0.43	0.88	1.32	1.39	2.19	1.56	1.00
expected	0.5	1	1.5	1.5	2	1.5	1

Table 4.8: *The different columns from Fig. 4.11 with the associated ion numbers. The ratios for the numerical integration work well for adjacent ions.*

This comparison works well for adjacent ions, but poorly for ions which are at different sides of the crystal. The asymmetry between the fluorescence strength of single ions compared between the left and right side of the crystal could already be observed in the crystals presented before. A possible explanation is a not perfectly aligned objective.

4.7.3 Multiple H_2^+ Ions in a flat Be^+ Crystal

By creating a flat Be^+ crystal like in section 4.7.1, and subsequently turning on the e-gun for approximately 60 s, multiple H_2^+ ions are created and accumulate at the nodal line of the crystal. An example for

such a crystal can be seen in Fig. 4.12, where the enclosed H_2^+ ions disturb the ordering in the center of the crystal.

Shape of the crystal

In the fluorescence projection along the $\hat{z}$ axis it can be seen that neither of the fit-functions set up earlier do the shape justice. This indicates that the crystal does neither possess a rotational symmetry around the $\hat{z}$ axis, nor is it a purely two-dimensional crystal. The number of ions is difficult to estimate. The crystal has no sharp boundaries, so that it is problematic to estimate the volume.

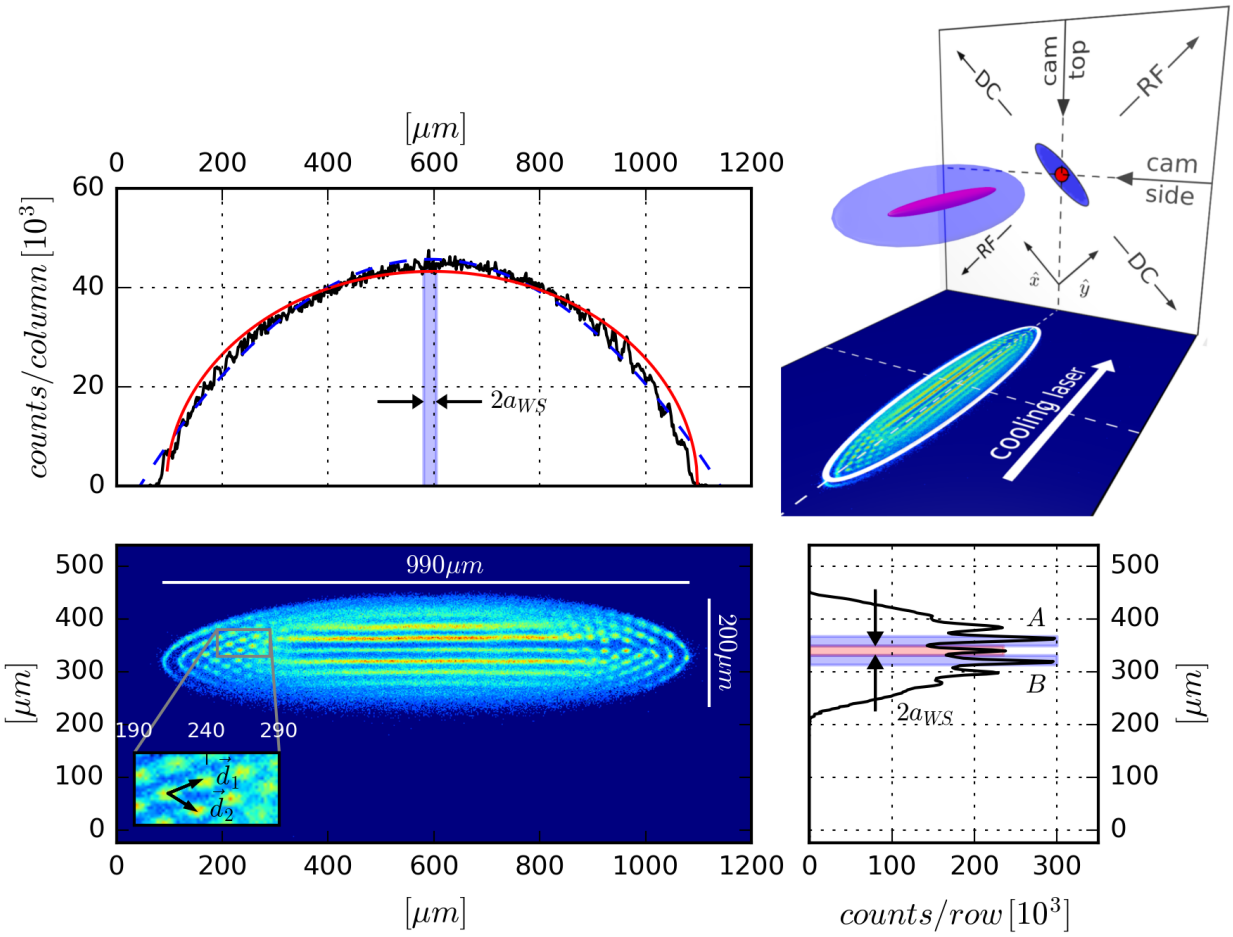

Figure 4.12: *A flat Coulomb crystal with approximately* 250 *to* 400 Be^+ *ions and* 5 - 9 H_2^+ *ions. The inset in the image at the bottom left shows a flat region of the crystal with a hexagonal lattice structure. In the center of the crystal sympathetically cooled* H_2^+ *ions are located. This can also be seen by the drop in the projected fluorescence in the crystal center (bottom right image). Neither of the fit functions for the projection along the* $\hat{z}$ *axis matches very well, indicating that the crystal is not symmetric in the* $\hat{r}$ *direction but also not purely two-dimensional.*

The fluorescence method also does not deliver precise results since there are no clearly separated ions. A comparison with the crystal in section 4.7.1 makes it plausible that the crystal contains roughly 250

– 350 ions.

detection of the H_2^+

Based on this assumption, and doing the approach of a constant fluorescence per ion throughout the crystal, one can estimate the number of ions responsible for the two peaks A and B in the projection of the fluorescence at the bottom right of Fig. 4.12. Depending on the number of ions each of that slices contains between 30 and 49 ions. For the peak in between the ion number ranges from 25 to 40 ions. Comparing these numbers one can estimate the amount of sympathetically cooled H_2^+ ions, ranging between 5 and 9 ions.

4.8 A three-component Crystal

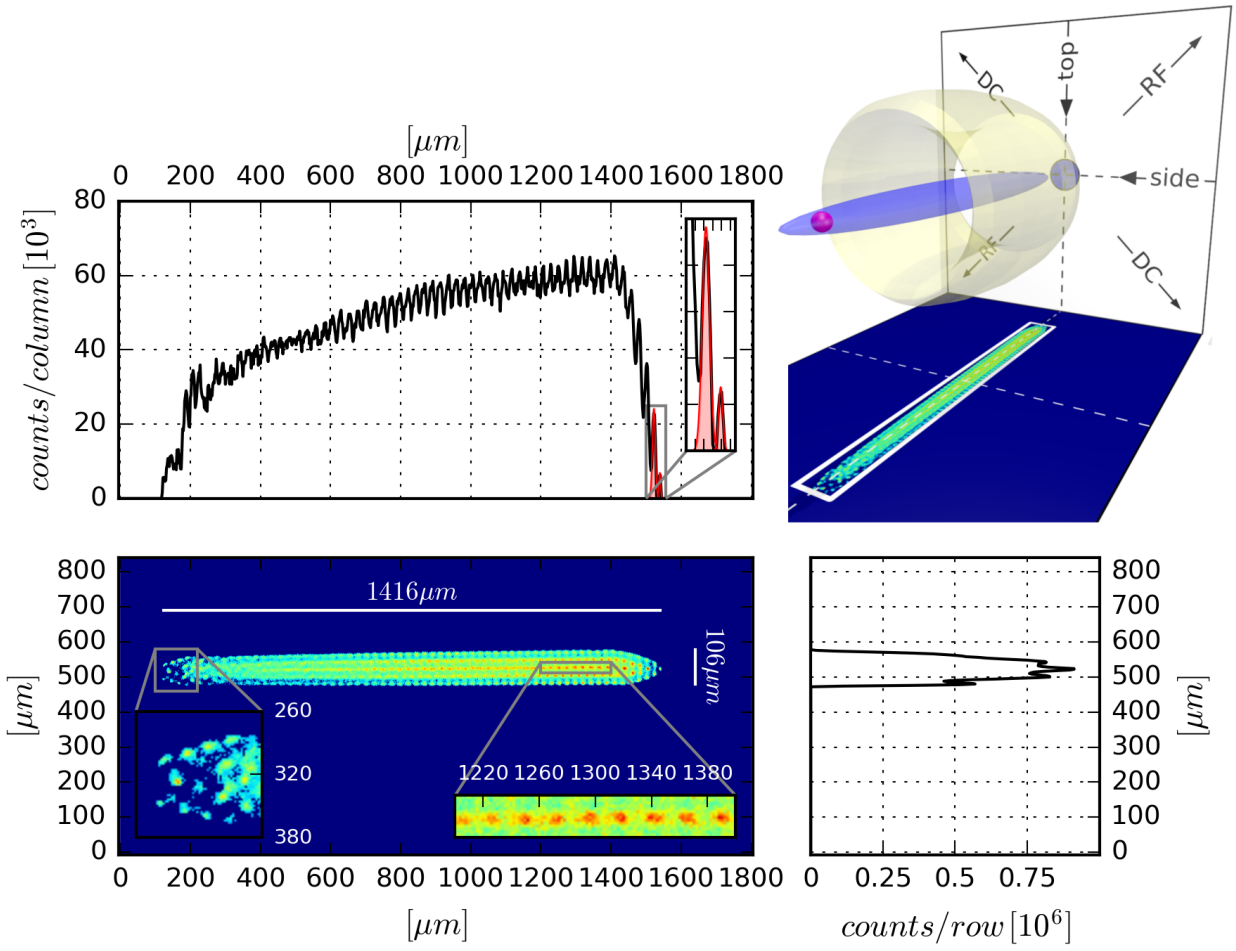

Figure 4.13: *A three component crystal consisting of approximately* 700 Be^+ *ions, enclosed* H_2^+ *ions at the left end of the crystal, and heavier ions around the* Be^+ *crystal. The heavier ions cause the elongated shape of the crystal (compare to Fig. 2.15)*

To obtain a large three component crystal as shown in Fig. 4.13, first a large Be^+ crystal must be created. After that turning on the

beryllium oven and e-gun for ≈ 45 s results in a growing of the Be^+ crystal and a deformation. The additionally created H_2^+ ions accumulate within the Be^+ crystal, while heavier ions, also coming from the residual gas, assemble around the Be^+ crystal and cause the elongated shape in form of a cylinder. The projections of the fluorescence signal are proportional to the ion density along the corresponding axis. Comparing the data in Fig. 4.13 with the results from simulations shown in Fig. 2.15 for the ion density along the two axes, consolidates the assumption that the measured data corresponds to a three component crystal.

4.9 A large Be^+/H_2^+ Coulomb Crystal

For the final goal of the experiment, the high resolution spectroscopy of H_2^+, it is desirable to obtain as many state selected, sympathetically cooled H_2^+ ions as possible. This allows for a better signal-to-noise ratio, since the signal to measure is the fractional ion loss of H_2^+. Fig. 4.14 shows a mixed Be^+/H_2^+ Coulomb crystal with a significant amount of H_2^+ ions.

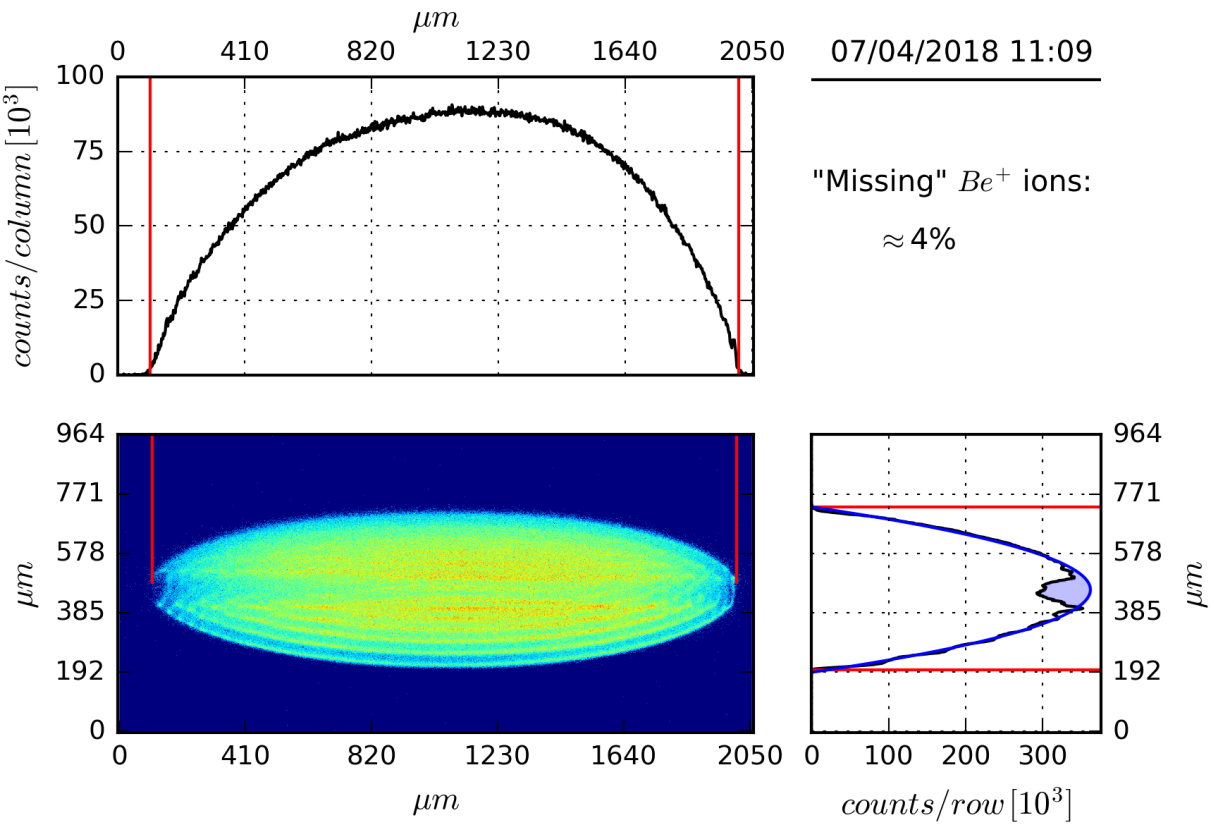

Figure 4.14: *A large* Be^+/H_2^+ *Coulomb crystal. The dip in the center of the fluorescence projection to the right indicates the amount of sympathetically cooled* H_2^+ *ions.*

This crystal was created in the following way: Starting point is the symmetric trap configuration (no additional U_0) with an RF amplitude of 230 V. Loading the trap with Be^+ (oven at 3.1 A, e-gun at 1.44 A) for 100 s creates also H_2^+ ions by electron impact. The next step consists of cleaning the crystal from heavier impurities by temporarily applying an additional U_0. Thereafter the detuning of the cooling laser is changed from -349 MHz to -49 MHz and the intensity is lowered from 7.5 mW to 0.7 mW.
The fluorescence projection to the right in Fig. 4.14 shows a dip at the center, caused by the sympathetically cooled H_2^+ ions. This dip is proportional to the amount of H_2^+ ions, and therefore a possible signal to measure the fractional ion loss after the spectroscopy sequence. The number of missing Be^+ ions in Fig. 4.14 is estimated by fitting the outer regions of the fluorescence projection with a quadratic function. Thereafter the integrals of the fit and the data are compared.

Chapter 5

Summary

The manuscript at hand presents the motivation, design and technical realisation of a new experimental setup to perform sympathetic cooling of H_2^+ ions via Be^+ Coulomb crystals. The final goal is to perform precision spectroscopy of the ro-vibrational, Doppler-free two-photon $\nu = 0, L = 2 \rightarrow \nu = 1, L = 2$ transition in the electronic ground state of the molecular hydrogen ion H_2^+, aiming at testing the validity of QED and obtaining improved values of fundamental constants, in particular the proton to electron mass ratio $\mu_{pe} = {}^{m_p}/_{m_e}$.

conclusion

Chapter two reviews the trapping mechanism of a linear Paul trap and elaborates the choice for the trap design. Furthermore, the Be^+ source, the vacuum system and the planned H_2^+ source are explained. Besides, the imaging system and the experiment control software are presented. Chapter three reviews the fundamentals of Doppler-cooling and presents different options to provide laser light for cooling of Be^+. Additionally the other necessary laser sources for precision spectroscopy of the $\nu = 0, L = 2 \rightarrow \nu = 1, L = 2$ transition of H_2^+ are described. Chapter four presents first results on the laser cooling and crystallization of Be^+ ions, and the characterization of obtained Coulomb crystals. While the state selective H_2^+ source has been shown to work [32], it is not yet implemented in the experimental setup presented here. Nevertheless, observation of sympathetically cooled H_2^+ ions could be performed by operating the trap in a stability region which is only stable for particles with mass ≤ 9 amu, and creating H_2^+ ions out of the residual gas by electron impact ionization. Although the resulting population of the $\nu = 0, L = 2$ state is considerably lower than in the case of state-selective production, this setup might be used for a first observation of the two-photon transition with a modest signal-to-noise ratio.

Furthermore, large, purely two-dimensional Coulomb crystals were observed and analysed. Two different lattice structures in the central region of these crystals were identified. Together with a novel technique to discriminate between two- and three-dimensional Coulomb crystals by means of fitting the fluorescence projections, these lattice

structures allow to verify the purely two-dimensional character of the observed crystals. Besides of being from interest for quantum simulations [36], two-dimensional crystals allow for a precise counting of sympathetically cooled, dark ions.

status During the preparation of the manuscript at hand the work towards preparation of ensembles of cold, state-selected H_2^+ ions was continued. Cooling via σ^+ polarized light was implemented and verified to work. At the moment the secular frequencies are probed in order to get insight of the impurities, detect sympathetically cooled H_2^+ ions with an additional method and verify the SIMION simulations. Furthermore, the design for the new H_2^+ source has been finished and is under preparation at the mechanical workshop. In addition an alternative $2 + 1$ REMPI scheme for state-selective H_2^+ production is investigated.

outlook While the implementation of the state selective H_2^+ source is prepared, three different topics may be investigated:

- Concerning H_2^+ spectroscopy: The state selective production of H_2^+ in the vibrational ground state is crucial for the signal-to-noise ratio of the spectroscopy measurement. Since the dissociation laser at 213 nm is ready to use and mainly acts on the H_2^+ ions in a higher vibrational state [32], it can be of interest to produce H_2^+ ions by electron impact, while the dissociation laser is active. This way one should end up with close to 100% of ions in $\nu = 0$, and therefore $\approx 12\%$ in the $\nu = 0, L = 2$ state. Together with a precise method to monitor the number of sympathetically cooled H_2^+ ions the search for a first spectroscopy signal can be started.

- Concerning two-dimensional lattice structures: Since 03/03/2018 a method is implemented which allows to smoothly change the the trap configuration between different points in the stability diagram. This allows to perform small and adiabatic changes in the trapping potential. Based on this method the phase transition between the centered square lattice and the hexagonal lattice may be investigated.

- Concerning GBAR: The two final steps in the preparation of the antihydrogen ion $\bar{H}^+$ are the sympathetic cooling of the $\bar{H}^+$ ion in a mixed HD^+/Be^+ Coulomb crystal, and thereafter ground state cooling of a $\bar{H}^+/Be^+$ ion pair in a precision trap. Before initiating the transfer of the $\bar{H}^+$ ion to the precision trap, it is important to verify that indeed one $\bar{H}^+$ ion is present in the mixed-species crystal. A possible solution is the following: after the sympathetic cooling in the mixed-species crystal was successful, and the $\bar{H}^+$ is at the nodal line of the RF potential, first the HD^+ must be removed by excitation of their secular frequencies. Thereafter the trap configuration can be smoothly changed

to create a two-dimensional Be^+ Coulomb crystal with one $\bar{H}^+$ ion enclosed. As can be seen in section 4.7.2, the precise location of sympathetically cooled ions in such a crystal is possible. Investigating the removal of sympathetically cooled H_2^+ in Be^+ crystals via excitation of their secular frequencies is performed now at LKB. If this works well the next step may be operating the trap in a stability region suitable for protons, H_2^+ and Be^+ ions. Using the dissociation laser at 213 nm may provide a mixed-species crystal with protons, H_2^+ and Be^+ ions, being close to the situation which is planned for GBAR. This will open up the possibility to investigate the removal of H_2^+ ions without losing the protons, mimicking the GBAR situation with $\bar{H}^+$, HD^+ and Be^+ ions.

A final task is to prepare the Python 3 code in such a way, that it can serve as a basis or example for experimental setups developed in other groups. Collaborations would allow to create a standardized library for the hardware interfacing of many devices used in the trapped ions community, with the ultimate goal of providing a shared software-package which is tailored for trapped ion experiments.

Appendices

Appendix A

.gem-files for SIMION

A.1 .gem-file for the optimal rod size

Below an example for the .gem-file for $r_e = 4\,\text{mm}$. Since r_e changes in each .gem-file also the distance $r' = r_e + R = 7.5\,\text{mm}$ between trap center and the center of the cylindrical electrode has to change, in order to keep $R = 3.5\,\text{mm}$ constant.

```
1  PA_define(261,261,141,planar,non-mirrored,electrostatic)
2
3  ; defines origin of coordinate system, scale of 10
4  ; origin equal trap center
5
6  locate(130,130,70,10,0,0,0){
7
8  ;ELECTRODE 1 RF
9          electrode(1) {
10         locate(0,0,-6,1,0,0,0)  {
11                 fill{within{cylinder(7.5,0,12,4.0,,12)}}
12
13                 fill{within{cylinder(-7.5,0,12,4.0,,12)}}
14                 }
15         }
16
17 ;ELECTRODE 2 CENTRAL ELECTRODES TO GROUND
18         electrode(2) {
19         locate(0,0,-6,1,0,-90,0)          {
20                 fill{within{cylinder(-7.5,0,12,4.0,,12)}}
21
22                 fill{within{cylinder(7.5,0,12,4.0,,12)}}
23                 }
24
25         }
26 }
```

A.2 .gem-file to estimate z_{eff}

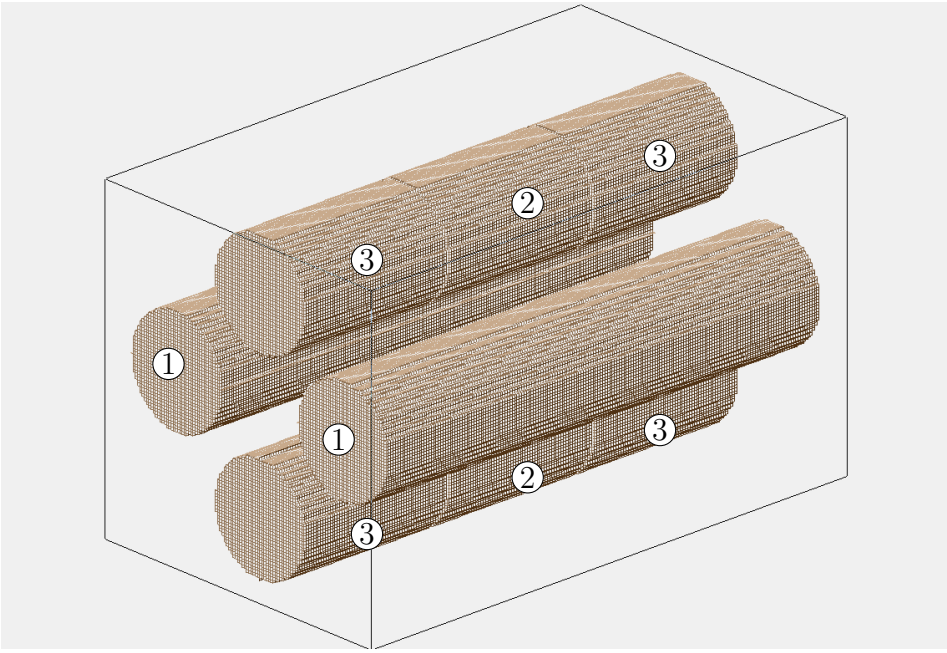

Figure A.1: *The electrodes are grouped in three potential arrays, each array can be scaled to an independent voltage.*

```
1  PA_define(241,241,401,planar,non-mirrored,electrostatic)
2
3  ; defines origin of coordinate system and scale of 10
4  ; origin equal trap center
5
6  locate(120,120,200,10,0,0,0){
7
8  ;ELECTRODE 1 RF
9          electrode(1) {
10         locate(0,0,-18.2,1,0,0,0)        {
11                 fill{within{cylinder(7.5,0,36.4,4,,36.4)}}
12
13                 fill{within{cylinder(-7.5,0,36.4,4,,36.4)}}
14         }
15         }
16
17 ;ELECTRODE 2 CENTER ELECTRODES
18         electrode(2) {
19         locate(0,0,-6,1,0,-90,0)         {
20                 fill{within{cylinder(-7.5,0,12,4,,12)}}
21
22                 fill{within{cylinder(7.5,0,12,4,,12)}}
23                 }
24         }
25
26 ;ELECTRODE 3 ENDCAPS
27         electrode(3) {
28         locate(0,0,6.2,1,0,-90,0)        {
29                 fill{within{cylinder(-7.5,0,12,4,,12)}}
30                 }
31
32         locate(0,0,-18.2,1,0,-90,0)      {
```

```
33                  fill{within{cylinder(-7.5,0,12,4,,12)}}
34                  }
35
36          locate(0,0,-18.2,1,0,-90,0)      {
37                  fill{within{cylinder(7.5,0,12,4,,12)}}
38                  }
39
40          locate(0,0,6.2,1,0,-90,0)        {
41                  fill{within{cylinder(7.5,0,12,4,,12)}}
42                  }
43          }
44  }
```

A.3 .gem-file for $\Phi_{\mathrm{SIM}}(x, y, z)$

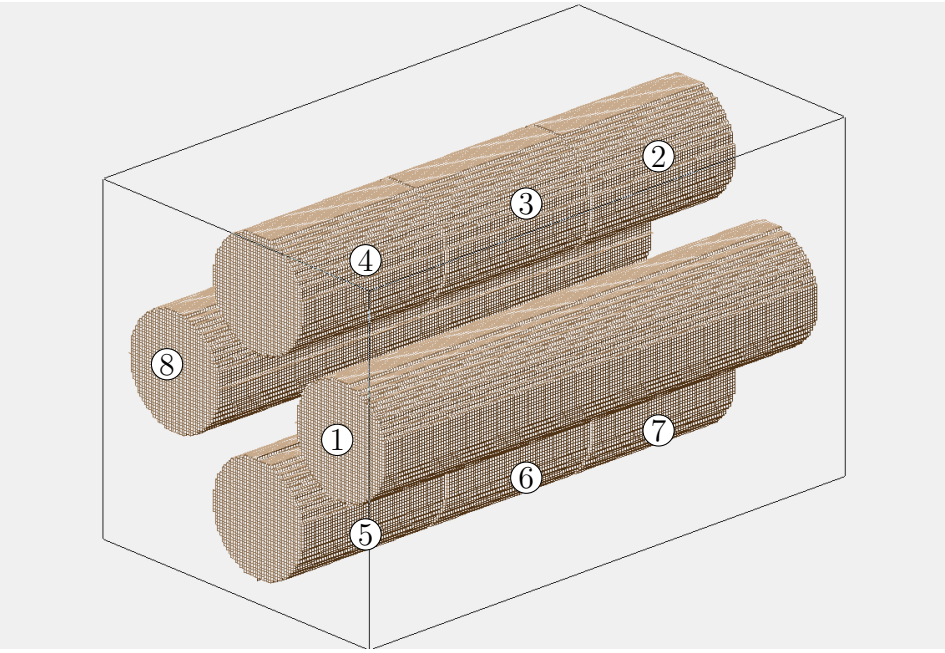

Figure A.2: *The trap in SIMION with its eight independent electrodes.*

```
1   PA_define(241,241,401,planar,non-mirrored,electrostatic)
2
3   ; defines origin of coordinate system and scale of 10
4   ; origin equal trap center
5
6   locate(120,120,200,10,0,0,0){
7
8   ;ELECTRODE 1 RF
9           electrode(1) {
10          locate(0,0,-18.2,1,0,0,0)        {
11                  fill{within{cylinder(-7.5,0,36.4,4,,36.4)}}
12                  }
13          }
14
15  ;ELECTRODE 2 endcap
```

```
16          electrode(2) {
17          locate(0,0,6.2,1,0,-90,0)       {
18                  fill{within{cylinder(-7.5,0,12,4,,12)}}
19                  }
20          }
21
22  ;ELECTRODE 3 center
23          electrode(3) {
24          locate(0,0,-6,1,0,-90,0)        {
25                  fill{within{cylinder(-7.5,0,12,4,,12)}}
26                  }
27          }
28
29  ;ELECTRODE 4 endcap
30          electrode(4) {
31          locate(0,0,-18.2,1,0,-90,0)     {
32                  fill{within{cylinder(-7.5,0,12,4,,12)}}
33                  }
34          }
35
36  ;ELECTRODE 5 endcap
37          electrode(5) {
38          locate(0,0,-18.2,1,0,-90,0)     {
39                  fill{within{cylinder(7.5,0,12,4,,12)}}
40                  }
41          }
42
43  ;ELECTRODE 6 center
44          electrode(6) {
45          locate(0,0,-6,1,0,-90,0)        {
46                  fill{within{cylinder(7.5,0,12,4,,12)}}
47                  }
48          }
49
50  ;ELECTRODE 7 endcap
51          electrode(7) {
52          locate(0,0,6.2,1,0,-90,0)       {
53                  fill{within{cylinder(7.5,0,12,4,,12)}}
54                  }
55          }
56
57  ;ELECTRODE 8 RF
58          electrode(8) {
59          locate(0,0,-18.2,1,0,0,0)       {
60                  fill{within{cylinder(7.5,0,36.4,4,,36.4)}}
61                  }
62          }
63  }
```

Bibliography

[1] A. I. Ångström. Ueber die Spectra der einfachen Gase. *Annalen der Physik*, **220**(10):300–307, 1871.

[2] A. I. Ångström. Ueber die Fraunhofer'schen Linien im Sonnenspectrum. *Annalen der Physik*, **193**(10):290–302, 1862.

[3] J. J. Balmer. Notiz über die Spectrallinien des Wasserstoffs. *Annalen der Physik*, **261**(5):80–87, 1885.

[4] M. Planck. Zur Theorie des Gesetzes der Energieverteilung im Normalspectrum. *Verhandlungen der Deutschen physikalischen Gesellschaft*, **2**(17):245, 1900.

[5] E. Rutherford. LXXIX. The scattering of α and β particles by matter and the structure of the atom. *The London, Edinburgh, and Dublin Philosophical Magazine and Journal of Science*, **21**(125):669–688, 1911.

[6] N. Bohr. I. On the constitution of atoms and molecules. *The London, Edinburgh, and Dublin Philosophical Magazine and Journal of Science*, **26**(151):1–25, 1913.

[7] E. Schrödinger. Quantisierung als Eigenwertproblem. *Annalen der Physik*, **384**(4):361–376, 1926.

[8] P. A. M. Dirac. The quantum theory of the electron. *Proceedings of the Royal Society of London A: Mathematical, Physical and Engineering Sciences*, **117**(778):610–624, 1928.

[9] Willis E. Lamb and Robert C. Retherford. Fine Structure of the Hydrogen Atom by a Microwave Method. *Phys. Rev.*, **72**:241–243, 1947.

[10] H. A. Bethe. The Electromagnetic Shift of Energy Levels. *Phys. Rev.*, **72**:339–341, 1947.

[11] CODATA. `https://physics.nist.gov/cuu/Constants/`. Accessed: 26/02/2018.

[12] Christian G. Parthey, Arthur Matveev, Janis Alnis, Birgitta Bernhardt, Axel Beyer, Ronald Holzwarth, Aliaksei Maistrou, Randolf Pohl, Katharina Predehl, Thomas Udem, Tobias Wilken, Nikolai Kolachevsky, Michel Abgrall, Daniele

Rovera, Christophe Salomon, Philippe Laurent, and Theodor W. Hänsch. Improved Measurement of the Hydrogen $1S$-$2S$ Transition Frequency. *Phys. Rev. Lett.*, **107**:203001, 2011.

[13] Axel Beyer, Lothar Maisenbacher, Arthur Matveev, Randolf Pohl, Ksenia Khabarova, Alexey Grinin, Tobias Lamour, Dylan C. Yost, Theodor W. Hänsch, Nikolai Kolachevsky, and Thomas Udem. The Rydberg constant and proton size from atomic hydrogen. *Science*, **358**(6359):79–85, 2017.

[14] Hélène Fleurbaey, Sandrine Galtier, Simon Thomas, Marie Bonnaud, Lucile Julien, François Biraben, François Nez, Michel Abgrall, and Jocelyne Guéna. New measurement of the $1S$ - $3S$ transition frequency of hydrogen: contribution to the proton charge radius puzzle. arXiv:1801.08816v1, 2018.

[15] Randolf Pohl, Aldo Antognini, François Nez, Fernando D. Amaro, François Biraben, João M. R. Cardoso, Daniel S. Covita, Andreas Dax, Satish Dhawan, Luis M. P. Fernandes, Adolf Giesen, Thomas Graf, Theodor W. Hänsch, Paul Indelicato, Lucile Julien, Cheng-Yang Kao, Paul Knowles, Eric-Olivier Le Bigot, Yi-Wei Liu, José A. M. Lopes, Livia Ludhova, Cristina M. B. Monteiro, Françoise Mulhauser, Tobias Nebel, Paul Rabinowitz, Joaquim M. F. dos Santos, Lukas A. Schaller, Karsten Schuhmann, Catherine Schwob, David Taqqu, João F. C. A. Veloso, and Franz Kottmann. The size of the proton. *Nature*, **466**, 2010.

[16] Øjvind Burrau. Berechnung des Energiewertes des Wasserstoffmolekel-Ions H_2^+ im Normalzustand. *Naturwissenschaften*, **15**(1):16–17, 1927.

[17] Eduard Teller. Über das Wasserstoffmolekülion. *Zeitschrift für Physik*, **61**(7):458–480, 1930.

[18] Egil A. Hylleraas. Über die Elektronenterme des Wasserstoffmoleküls. *Zeitschrift für Physik*, **71**(11):739–763, 1931.

[19] George Jaffé. Zur Theorie des Wasserstoffmolekülions. *Zeitschrift für Physik*, **87**(7):535–544, 1934.

[20] J.-Ph. Karr, L. Hilico, J. C. J. Koelemeij, and V. I. Korobov. Hydrogen molecular ions for improved determination of fundamental constants. *Phys. Rev. A*, **94**:050501, 2016.

[21] William H. Wing, George A. Ruff, Willis E. Lamb, and Joseph J. Spezeski. Observation of the Infrared Spectrum of the Hydrogen Molecular Ion HD^+. *Phys. Rev. Lett.*, **36**:1488–1491, 1976.

[22] J. Biesheuvel, J.-Ph. Karr, L. Hilico, K.S.E. Eikema, W. Ubachs, and J.C.J. Koelemeij. Probing QED and fundamental constants through laser spectroscopy of vibrational transitions in HD^+. *Nature Communications*, **7**, 2016.

[23] Sayan Patra, J-Ph Karr, L Hilico, M Germann, V I Korobov, and J C J Koelemeij. Proton-electron mass ratio from HD^+ revisited. *Journal of Physics B: Atomic, Molecular and Optical Physics*, **51**(2):024003, 2018.

[24] Maximilian Beyer, Nicolas Hölsch, Josef A. Agner, Johannes Deiglmayr, Hansjürg Schmutz, and Frédéric Merkt. Metrology of high-n Rydberg states of molecular hydrogen with $\Delta\nu/\nu = 2 \times 10^{-10}$ accuracy. *Phys. Rev. A*, **97**:012501, 2018.

[25] Vladimir I. Korobov, L. Hilico, and J.-Ph. Karr. Fundamental Transitions and Ionization Energies of the Hydrogen Molecular Ions with Few ppt Uncertainty. *Phys. Rev. Lett.*, **118**:233001, 2017.

[26] Jean-Philippe Karr. Private communication, 2018.

[27] S. Sturm, F. Köhler, J. Zatorski, A. Wagner, Z. Harman, G. Werth, W. Quint, C. H. Keitel, and K. Blaum. High-precision measurement of the atomic mass of the electron. *Nature*, **506**:467–470, 2014.

[28] F. Heiße, F. Köhler-Langes, S. Rau, J. Hou, S. Junck, A. Kracke, A. Mooser, W. Quint, S. Ulmer, G. Werth, K. Blaum, and S. Sturm. High-Precision Measurement of the Proton's Atomic Mass. *Phys. Rev. Lett.*, **119**:033001, 2017.

[29] Vladimir L. Ryjkov, XianZhen Zhao, and Hans A. Schuessler. Simulations of the rf heating rates in a linear quadrupole ion trap. *Phys. Rev. A*, **71**:033414, 2005.

[30] R. D. Knight and M. H. Prior. Laser scanning measurement of the density distribution of confined $^6Li^+$ ions. *Journal of Applied Physics*, **50**(5):3044–3049, 1979.

[31] P. Pérez, D. Banerjee, F. Biraben, D. Brook-Roberge, M. Charlton, P. Cladé, P. Comini, P. Crivelli, O. Dalkarov, P. Debu, A. Douillet, G. Dufour, P. Dupré, S. Eriksson, P. Froelich, P. Grandemange, S. Guellati, R. Guérout, J. M. Heinrich, P.-A. Hervieux, L. Hilico, A. Husson, P. Indelicato, S. Jonsell, J.-P. Karr, K. Khabarova, N. Kolachevsky, N. Kuroda, A. Lambrecht, A. M. M. Leite, L. Liszkay, D. Lunney, N. Madsen, G. Manfredi, B. Mansoulié, Y. Matsuda, A. Mohri, T. Mortensen, Y. Nagashima, V. Nesvizhevsky, F. Nez, C. Regenfus, J.-M. Rey, J.-M. Reymond, S. Reynaud, A. Rubbia, Y. Sacquin, F. Schmidt-Kaler, N. Sillitoe, M. Staszczak, C. I. Szabo-Foster, H. Torii, B. Vallage, M. Valdes, D. P. Van der Werf, A. Voronin, J. Walz, S. Wolf, S. Wronka, and Y. Yamazaki. The GBAR antimatter gravity experiment. *Hyperfine Interactions*, **233**(1):21–27, 2015.

[32] Nicolas Sillitoe. *Production of state-selected H_2^+ ions and numerical simulations of sympathetic cooling in RF traps.* PhD thesis, Université Pierre-et-Marie-Curie, 2017.

[33] R. P. Feynman. Simulating Physics with Computers. *International Journal of Theoretical Physics*, **21**(6):467–488, 1982.

[34] Michael Johanning, Andrés F Varón, and Christof Wunderlich. Quantum simulations with cold trapped ions. *Journal of Physics B: Atomic, Molecular and Optical Physics*, **42**(15):154009, 2009.

[35] B. Szymanski, R. Dubessy, B. Dubost, S. Guibal, J.-P. Likforman, and L. Guidoni. Large two dimensional Coulomb crystals in a radio frequency surface ion trap. *Applied Physics Letters*, **100**(17):171110, 2012.

[36] Philip Richerme. Two-dimensional ion crystals in radio-frequency traps for quantum simulation. *Phys. Rev. A*, **94**:032320, 2016.

[37] W. Paul, H. P. Reinhard, and U. von Zahn. Das elektrische Massenfilter als Massenspektrometer und Isotopentrenner. *Zeitschrift für Physik*, **152**(2):143–182, 1958.

[38] Wolfgang Paul. Electromagnetic traps for charged and neutral particles. *Rev. Mod. Phys.*, **62**(3):531–540, 1990.

[39] Georg Jacob, Karin Groot-Berning, Sebastian Wolf, Stefan Ulm, Luc Couturier, Ulrich G. Poschinger, Ferdinand Schmidt-Kaler, and Kilian Singer. Single particle microscopy with nanometer resolution. arXiv:1405.6480, 2014.

[40] Sebastian Wolf, Julian Wechs, Joachim von Zanthier, and Ferdinand Schmidt-Kaler. Visibility of young's interference fringes: Scattered light from small ion crystals. *Phys. Rev. Lett.*, **116**:183002, 2016.

[41] Sebastian Wolf and Ferdinand Schmidt-Kaler. Private communication, 2017.

[42] Laurent Hilico, Jean-Philippe Karr, Albane Douillet, Paul Indelicato, Sebastian Wolf, and Ferdinand Schmidt Kaler. Preparing single ultra-cold antihydrogen atoms for free-fall in GBAR. *International Journal of Modern Physics: Conference Series*, **30**:1460269, 2014.

[43] F. G. Major, V. N. Gheorghe, and G. Werth. *Charged Particle Traps.* Springer-Verlag Berlin Heidelberg, 2005.

[44] L. D. Landau and E. M. Lifshitz. *Mechanics.* Pergamon Press Ltd., 3rd edition, 1976.

[45] D. R. Denison. Operating Parameters of a Quadrupole in a Grounded Cylindrical Housing. *The Journal of Vacuum Science and Technology*, **8**(1):266–269, 1971.

[46] J. Pedregosa, C. Champenois, M. Houssin, and M. Knoop. Anharmonic contributions in real RF linear quadrupole traps. *International Journal of Mass Spectroscopy*, **290**(2-3):100–105, 2009.

[47] Jurrian Biesheuvel. *Probing QED and fundamental constants through vibrational spectroscopy of HD^+*. PhD thesis, Vrije Universiteit Amsterdam, 2016.

[48] L Hilico, N Billy, B Grémaud, and D Delande. Polarizabilities, light shifts and two-photon transition probabilities between J = 0 states of the H_2^+ and D_2^+ molecular ions. *Journal of Physics B: Atomic, Molecular and Optical Physics*, **34**(3):491, 2001.

[49] Jean-Philippe Karr, Franck Bielsa, Albane Douillet, Jofre Pedregosa Gutierrez, Vladimir I. Korobov, and Laurent Hilico. Vibrational spectroscopy of $H_2{}^+$: Hyperfine structure of two-photon transitions. *Phys. Rev. A*, **77**, 2008.

[50] H. Kogelnik and T. Li. Laser Beams and Resonators. *Applied Optics*, **5**(10):1550–1567, 1966.

[51] J. D. Siverns, L. R. Simkins, S. Weidt, and W. K. Hensinger. On the application of radio frequency voltages to ion traps via helical resonators. *Appl Phys B*, **107**(4):921–934, 2012.

[52] Harald Schnitzler. *Development of an Experiment for Trapping, Cooling, and Spectroscopy of Molecular Hydrogen Ions.* PhD thesis, Universität Konstanz, 2001.

[53] S. Wolf, D. Studer, K. Wendt, and F. Schmidt-Kaler. Efficient and robust photo-ionization loading of beryllium ions. arXiv:1711.01060, November 2017.

[54] Gas Correction Factors for Bayard-Alpert Ionization Gauges. `http://www.thinksrs.com/downloads/PDFs/ApplicationNotes/IG1BAgasapp.pdf`. Accessed: 06/02/2018.

[55] M. Wong. Review of papers regarding vacuum system and materials. `http://home.fnal.gov/~mlwong/outgas_rev.htm`. Accessed: 06/02/2018.

[56] Peter Lebedew. Untersuchungen über die Druckkräfte des Lichtes. *Annalen der Physik*, **311**(11):433–458, 1901.

[57] Kastler, Alfred. Quelques suggestions concernant la production optique et la détection optique d'une inégalité de population des niveaux de quantifigation spatiale des atomes. Application à l'expérience de Stern et Gerlach et à la résonance magnétique. *J. Phys. Radium*, **11**(6):255–265, 1950.

[58] D. J. Wineland, R. E. Drullinger, and F. L. Walls. Radiation-Pressure Cooling of Bound Resonant Absorbers. *Phys. Rev. Lett.*, **40**:1639–1642, 1978.

[59] Wilfried Nörtershäuser, Christopher Geppert, Andreas Krieger, Krzysztof Pachucki, Mariusz Puchalski, Klaus Blaum, Mark L. Bissell, Nadja Frömmgen, Michael Hammen, Magdalena Kowalska, Jörg Krämer, Kim Kreim, Rainer Neugart, Gerda Neyens, Rodolfo Sánchez, and Deyan T. Yordanov. Precision Test of Many-Body QED in the Be^+ $2p$ Fine Structure Doublet Using Short-Lived Isotopes. *Phys. Rev. Lett.*, **115**:033002, 2015.

[60] C. Cohen-Tannoudji. Atomic motion in laser light. In J. Dalibard, J.M. Raimond, and J. Zinn Justin, editors, *Fundamental Systems in Quantum Optics*. Elsevier Science Publisher B.V., 1992. Les Houches, Session LIII, 1990.

[61] R. C. Hilborn. Einstein coefficients, cross sections, f values, dipole moments, and all that. arXiv:physics/0202029v1, 2002.

[62] F. M. J. Cozijn, J. Biesheuvel, A. S. Flores, W. Ubachs, G. Blume, A. Wicht, K. Paschke, G. Erbert, and J. C. J. Koelemeij. Laser cooling of beryllium ions using a frequency-doubled 626 nm diode laser. *Opt. Lett.*, **38**(13):2370–2372, Jul 2013.

[63] C. Monroe, D. M. Meekhof, B. E. King, S. R. Jefferts, W. M. Itano, D. J. Wineland, and P. Gould. Resolved-Sideband Raman Cooling of a Bound Atom to the 3D Zero-Point Energy. *Phys. Rev. Lett.*, **75**:4011–4014, 1995.

[64] A. C. Wilson, C. Ospelkaus, A. P. VanDevender, J. A. Mlynek, K. R. Brown, D. Leibfried, and D. J. Wineland. A 750-mW, continuous-wave, solid-state laser source at 313 nm for cooling and manipulating trapped $^9Be^+$ ions. *Applied Physics B*, **105**:741–748, 2011.

[65] Hsiang-Yu Lo, Joseba Alonso, Daniel Kienzler, Benjamin C. Keitch, Ludwig E. de Clercq, Vlad Negnevitsky, and Jonathan P. Home. All-solid-state continuous-wave laser systems for ionization, cooling and quantum state manipulation of beryllium ions. *Applied Physics B*, **114**(1), 2014.

[66] S. Vasilyev, A. Nevsky, I. Ernsting, M. Hansen, J. Shen, and S. Schiller. Compact all-solid-state continuous-wave single-frequency UV source with frequency stabilization for laser cooling of Be^+ ions. *Applied Physics B*, **103**(1), 2011.

[67] H. Ball, M. W. Lee, S. D. Gensemer, and M. J. Biercuk. A high-power 626 nm diode laser system for Beryllium ion trapping. *Review of Scientific Instruments*, **84**(6):063107, 2013.

[68] X. Baillard, A. Gauguet, S. Bize, P. Lemonde, Ph. Laurent, A. Clairon, and P. Rosenbusch. Interference-filter-

stabilized external-cavity diode lasers. *Optics Communications*, **266**(2):609 – 613, 2006.

[69] G. Blume, O. Nedow, D. Feise, J. Pohl, and K. Paschke. Monolithic 626 nm single-mode AlGaInP DBR diode laser. *Opt. Express*, **21**(18):21677–21684, Sep 2013.

[70] R. Clark Jones. A New Calculus for the Treatment of Optical SystemsI. Description and Discussion of the Calculus. *J. Opt. Soc. Am.*, **31**(7):488–493, 1941.

[71] J. C. J. Koelemeij, W. Hogervorst, and W. Vassen. High-power frequency stabilized laser for laser cooling of metastable helium at 389 nm. *Review of Scientific Instruments*, **76**(3):033104, 2005.

[72] S. Hannig, J. Mielke, J. A. Fenske, M. Misera, N. Beev, C. Ospelkaus, and P. O. Schmidt. A highly stable monolithic enhancement cavity for SHG generation in the UV. arXiv:1709.07188v1, 09 2017.

[73] T. W. Hänsch and B. Couillaud. Laser Frequency Stabilization by Polarization Spectroscopy of a Reflecting Reference Cavity. *Optics Communications*, **35**:441–444, 1980.

[74] G. D. Boyd and D. A. Kleinman. Parametric Interaction of Focused Gaussian Light Beams. *Journal of Applied Physics*, **39**(8):3597–3639, 1968.

[75] A. Ashkin, G. Boyd, and J. Dziedzic. Resonant optical second harmonic generation and mixing. *IEEE Journal of Quantum Electronics*, **2**(6):109–124, 1966.

[76] E. S. Polzik and H. J. Kimble. Frequency doubling with $KNbO_3$ in an external cavity. *Opt. Lett.*, **16**(18):1400–1402, 1991.

[77] J.-P. Karr, A. Douillet, and L. Hilico. Photodissociation of trapped H_2^+ ions for REMPD spectroscopy. *Applied Physics B*, **107**(4):1043–1052, 2012.

[78] S.T. Pratt, P.M. Dehmer, and J.L. Dehmer. Photoionization of excited molecular states. H_2 C^1 Π_u. *Chemical Physics Letters*, **105**(1):28 – 33, 1984.

[79] Vu Quang Tran. *Towards high precision spectroscopy of hydrogen molecular ions H_2^+ and HD^+: Theory and Experiment.* PhD thesis, Université Pierre-et-Marie-Curie, 2013.

[80] M. A. O'Halloran, S. T. Pratt, P. M. Dehmer, and J. L. Dehmer. Photoionization dynamics of H_2 C^1 Π_u: Vibrational and rotational branching ratios. *The Journal of Chemical Physics*, **87**(6):3288–3298, 1987.

[81] Frank Bielsa. *Spectroscopie vibrationelle à deux photons de l'Ion H_2^+: Développement d'une source laser à 9.166 μm*. PhD thesis, Université Pierre-et-Marie-Curie, 2007.

[82] Frank Bielsa, Albane Douillet, Tristan Valenzuela, Jean-Philippe Karr, and Laurent Hilico. Narrow-line phase-locked quantum cascade laser in the 9.2 μm range. *Optics Letters*, **32**(12):1641–1643, 2007.

[83] E. Wigner. On the interaction of electrons in metals. *Phys. Rev.*, **46**:1002–1011, 1934.

[84] F. Diedrich, E. Peik, J. M. Chen, W. Quint, and H. Walther. Observation of a Phase Transition of Stored Laser-Cooled Ions. *Phys. Rev. Lett.*, **59**:2931–2934, 1987.

[85] D. J. Wineland, J. C. Bergquist, Wayne M. Itano, J. J. Bollinger, and C. H. Manney. Atomic-Ion Coulomb Clusters in an Ion Trap. *Phys. Rev. Lett.*, **59**:2935–2938, 1987.

[86] J. P. Schiffer, M. Drewsen, J. S. Hangst, and L. Hornekær. Temperature, ordering, and equilibrium with time-dependent confining forces. *Proceedings of the National Academy of Sciences of the United States of America*, **97**:10697–10700, 2000.

[87] G. Birkl, S. Kassner, and H. Walther. Multiple-shell structures of laser-cooled $^{24}Mg^+$ ions in a quadrupole storage ring. *Nature*, **357**:310–313, 1992.

[88] I. Waki, S. Kassner, G. Birkl, and H. Walther. Observation of ordered structures of laser-cooled ions in a quadrupole storage ring. *Phys. Rev. Lett.*, **68**:2007–2010, 1992.

[89] M Block, A Drakoudis, H Leuthner, P Seibert, G Werth, M Block, A Drakoudis, H Leuthner, and P Seibert. Crystalline ion structures in a Paul trap. *Journal of Physics B: Atomic, Molecular and Optical Physics*, **33**(11):L375, 2000.

[90] M. Drewsen, C. Brodersen, L. Hornekær, and J. S. Hangst. Large Ion Crystals in a Linear Paul Trap. *Phys. Rev. Lett.*, **81**:2878–2881, 1992.

[91] D. J. Berkeland, J. D. Miller, J. C. Bergquist, W. M. Itano, and D. J. Wineland. Minimization of ion micromotion in a Paul trap. *Journal of Applied Physics*, **83**(10):5025–5033, 1998.

[92] Du Li-Jun, Chen Ting, Song Hong-Fang, Chen Shao-Long, Li Hai-Xia, Huang Yao, Tong Xin, Gao Ke-Lin, and Guan Hua. Compensating for excess micromotion of ion crystals. *Chinese Physics B*, **24**(8):083702, 2015.

[93] P. Bowe, L. Hornekær, C. Brodersen, M. Drewsen, J. S. Hangst, and J. P. Schiffer. Sympathetic Crystallization of Trapped Ions. *Phys. Rev. Lett.*, **82**:2071–2074, 1999.

[94] C. B. Zhang, D. Offenberg, B. Roth, M. A. Wilson, and S. Schiller. Molecular-dynamics simulations of cold single-species and multispecies ion ensembles in a linear Paul trap. *Phys. Rev. A*, **76**:012719, 2007.

[95] M. R. Kamsap, J. Pedregosa-Gutierrez, C. Champenois, D. Guyomarc'h, M. Houssin, and M. Knoop. Fast and efficient transport of large ion clouds. *Phys. Rev. A*, **92**:043416, 2015.

[96] R. E. Drullinger, D. J. Wineland, and J. C. Bergquist. High-resolution optical spectra of laser cooled ions. *Applied physics*, **22**(4):365–368, 1980.

[97] D. J. Larson, J. C. Bergquist, J. J. Bollinger, Wayne M. Itano, and D. J. Wineland. Sympathetic cooling of trapped ions: A laser-cooled two-species nonneutral ion plasma. *Phys. Rev. Lett.*, **57**:70–73, 1986.

[98] Takashi Baba and Izumi Waki. Cooling and Mass-Analysis of Molecules Using Laser-Cooled Atoms. *Japanese Journal of Applied Physics*, **35**(9A):L1134, 1996.

[99] Yoshiki Moriwaki, Maki Tachikawa, Yoshiharu Maeno, and Tadao Shimizu. Collision Cooling of Ions Stored in Quadrupole Radio-Frequency Trap. *Japanese Journal of Applied Physics*, **31**(11B):L1640, 1992.

[100] Stephan Schiller and Claus Lämmerzahl. Molecular dynamics simulation of sympathetic crystallization of molecular ions. *Phys. Rev. A*, **68**:053406, 2003.

[101] Residual gas composition. `https://www.pfeiffer-vacuum.com/en/know-how/introduction-to-vacuum-technology/influences-in-real-vacuum-systems/residual-gas-composition/`. Accessed: 09/02/2018.

Un piège à Be^+ pour la spectroscopie d'H_2^+

Résumé: L'objectif du projet est la mesure du rapport de la masse de l'électron à celle du proton par spectroscopie vibrationnelle à deux photons sans effet Doppler de H_2^+. Le refroidissement des ions H_2^+ est nécessaire et ne peut être fait que par refroidissement sympathique par des ions Be^+ refroidis par laser.
La première partie présente la conception et la réalisation d'un piège linéire adapté au confinement des ions H_2^+ et Be^+ et permettant les accès optiques nécessaires pour les lasers et l'imagerie.
La seconde partie décrit les sources laser à 626 (à base de diodes laser ou de lasers à fibres) ainsi que la cavité de doublage de fréquence utilisés pour obtenir le faisceau à 313 nm pour refroidir les ions Be^+.
La dernière partie expose les premiers résultats obtenus qui montrent que le montage est opérationnel. Elle présente l'observation et la caractérisation de cristaux de Coulomb de Be^+ ainsi que des cristaux de Coulomb mixtes Be^+/H_2^+ où les ions H_2^+ sont créés par impact électronique à partir du gaz résiduel. Ces résultats montrent que le montage est prêt pour réaliser la spectroscopie de H_2^+.

A Be^+ Ion Trap for H_2^+ Spectroscopy

Abstract: The objective of the project is to perform high-resolution Doppler-free two-photon vibrational spectroscopy of the H_2^+ molecular ion for accurate electron to proton mass ratio determination. Trapping and laser-cooling of the H_2^+ ions is necessary. Since H_2^+ molecular ions cannot be directly laser cooled, a solution is the implementation of sympathetic cooling via laser cooled Be^+ ions.
In the first part of this thesis the design and implementation of a linear Paul trap is presented. This trap is suitable to confine H_2^+ and Be^+ ions while allowing good optical access for multiple laser sources and the imaging system.
The second part describes a low power, diode based laser system to provide narrow linewidth 626nm light, and a high power, fiber laser based laser system. Subsequently, a bow-tie cavity is presented to frequency double the 626nm light to obtain 313nm light for Be^+ Doppler-cooling.
In the last part the operational readiness of the trap and the fiber laser based 313nm laser source is demonstrated by the observation of Be^+ Coulomb crystals. Electron impact ionization of H_2 present in the residual gas allows to observe sympathetic cooling and shows that the developed setup can provide the experimental conditions for precision spectroscopy of H_2^+.